Università degli Studi di Cagliari

Ph.D. DEGREE
Physics

Cycle XXXIV

TITLE OF THE Ph.D. THESIS
Pixel Chamber: an active target with monolithic pixel sensors for precision measurements of charm and beauty

Scientific Disciplinary Sector(s)

Fis/01 Fis/04

Ph.D. Student:	Alice Mulliri
Supervisor	Gianluca Usai

Final exam. Academic Year 2020/2021
Thesis defence: April 2022 Session

Back off, man. I'm a scientist.

Dr. Peter Venkman

Contents

List of Figures

List of Tables

Abstract

Modern vertex detectors are based on cylindrical or planar layers of silicon sensors. These detectors are used for precision measurements of tracks and vertices of particles produced in the interactions. Since the tracking layers are always few to tens of cm from the interaction point, this poses an ultimate limitation in the achievable resolution of the vertex position.

A silicon-based active target detector capable to image particles produced inside the detector volume in 3D, similarly to a bubble chamber, does not exist. Ideas for a silicon active target providing continuous tracking were put forward already 40 years ago but the required technology just did not exist until recently.

In this work, I will describe the idea for the first silicon active target based on silicon pixel sensors, called Pixel Chamber, capable to perform continuous, high resolution (O(μm)) 3D tracking, including open charm and beauty particles.

The aim is to create a bubble chamber-like high-granularity stack of hundreds of very thin monolithic active pixel sensors (MAPS) glued together. To do this, the ALPIDE sensor chip, designed for the ALICE experiment at the CERN LHC, will be used. R&D for prototypes developments is actually ongoing.

The power consumption of a stack consisting of hundreds of ALPIDE is such as to bring the sensor to very high temperatures. For this reason, simulations were carried out to evaluate different cooling options.

A tracking and vertexing algorithm has been specifically developed to reconstruct tracks and vertices inside Pixel Chamber. It has been tested on Monte Carlo simulations of proton-silicon interactions occurring inside the sensor. According to those simulations, it is possible to obtain a high efficiency for the reconstruction of hadronic tracks, and for the primary and secondary vertices inside the detector. The vertex resolution can be up to one order of magnitude better than state-of-the-art detectors like those of LHC experiments.

The tracking algorithm has been also tested to reconstruct tracks produced in a single ALPIDE sensor exposed to electrons and hadrons beams. Results show that it is possible to obtain very good performances in long track reconstruction on a single ALPIDE.

Chapter 1

Introduction

1.1 Silicon trackers in particle physics experiments

Silicon detectors are key for track and vertex reconstruction in modern high energy physics experiments. Located close to the interaction point, they provide precision measurement of particles produced in the primary vertex, and in particular, for the reconstruction of the decay products of long lived particles, like open charm or beauty states, emerging from secondary vertices, tens to hundreds of microns from the primary vertex depending on the specific particle lifetime and momentum.

Typically the innermost detector layer is a few to tens of centimeters from the interaction point. For this reason, the track of an open charm or beauty particle cannot be directly imaged and furthermore its decay charged tracks have to be back-extrapolated to the decay vertex. Track reconstruction usually starts from the hits in the outermost layers or planes and proceeds backwards to the interaction point. The primary vertex is reconstructed by its position from some average of the intersections of all reconstructed tracks. The primary vertex resolution is, for this reason, mainly determined by the number of these tracks and the precision in the spatial position of the individual reconstructed tracks. The latter quantity is determined mostly by the measurements of the track position in the innermost layers, preferably having the first layer as close as possible to the interaction point. This is a fundamental quantity since a secondary vertex is inferred by extrapolated tracks not pointing to the primary interaction vertex. Thus, an intrinsic limitation of the system is just due to the finite distance of the tracking layers from the interaction point.

To reconstruct charm or beauty particles, topological variables determined from track reconstruction are used. For example, Figure 1.1 shows the decay of a D^0 into a kaon and a pion. This figure illustrates two quantities fundamental for the decay reconstruction: the track impact parameter, which is the distance between the daughter particle trajectory (d_0) and the mother particle production point (the primary vertex in the case of a primary D^0 produced in the main collision), and the

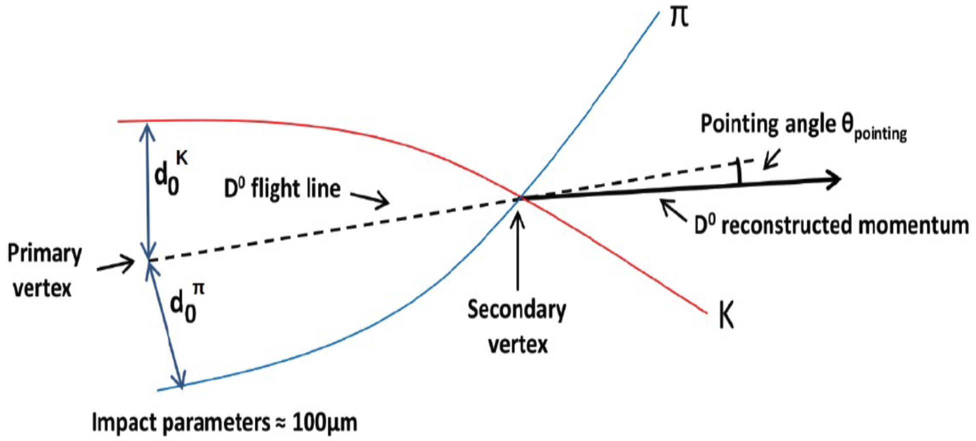

Figure 1.1: *D^0 decay in a pion and a kaon.*

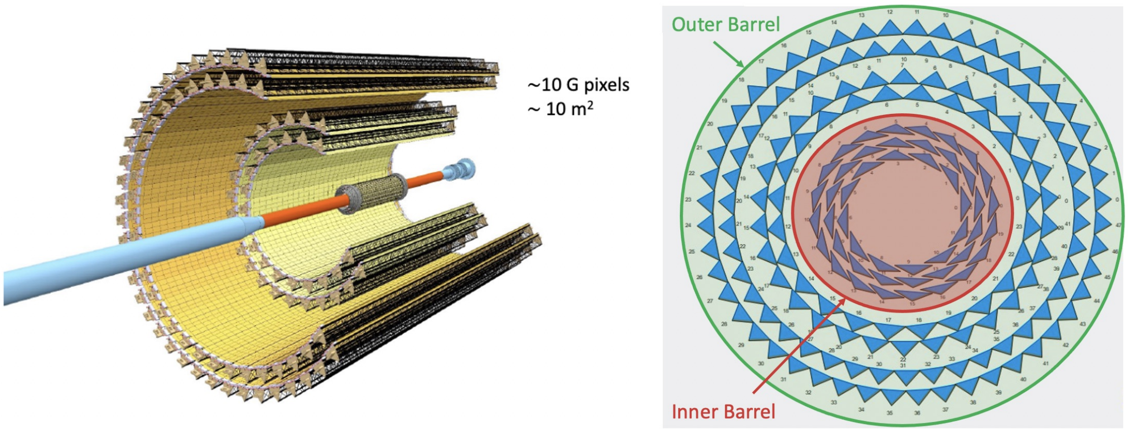

Figure 1.2: *Left: ALICE Inner Tracking System (ITS2) scheme. Right: ITS2 staves segmentation*

pointing angle.

An example of modern tracker is the newly installed ALICE Inner Tracking System (ITS2) that consists of seven cylindrical layers of Monolithic Active Pixel Sensors (MAPS) (Figure 1.2, left) [1]. The MAPS that constitute the ITS2 cylindrical layers are called ALice PIxel DEtector (ALPIDE, described in section 2.2.1) [2, 3] and have been developed specifically for ITS2 with a 180 nm CMOS technology provided by TowerJazz [4]. The pixel dimension is 29.24x26.88 µm^2 and an ALPIDE sensor contains a matrix of 512x1024 pixels for a total area of 30x15 mm^2. The sensor thickness is 50 µm and the spatial resolution is 5 µm. Given their small area the sensors need to be arranged in units called staves to cover the full surface of the ITS2.

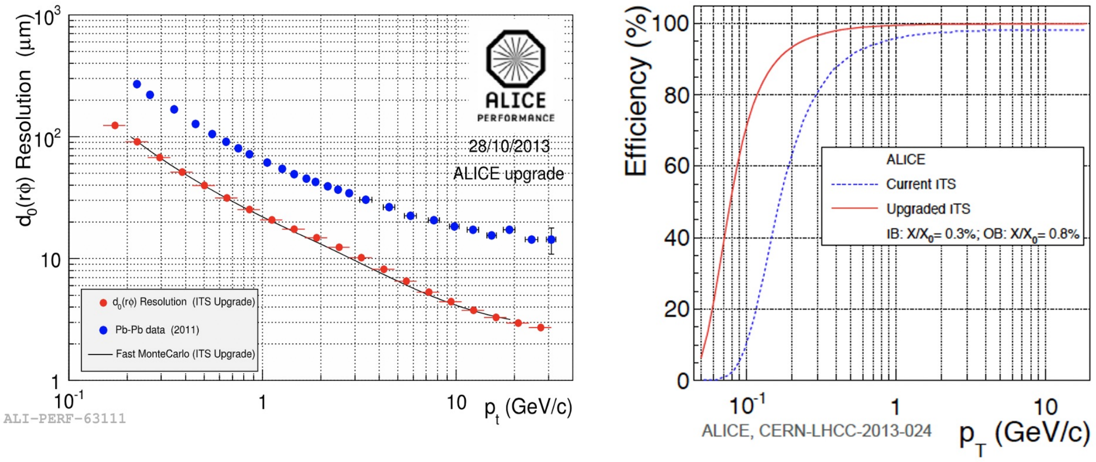

Figure 1.3: *Left: impact parameter resolution comparison between old ITS (blue) and the ITS2 (red) [5]. Right: track reconstruction efficiency comparison between old ITS (blue, called "current ITS") and the ITS2 (red, called "Upgraded ITS") [1].*

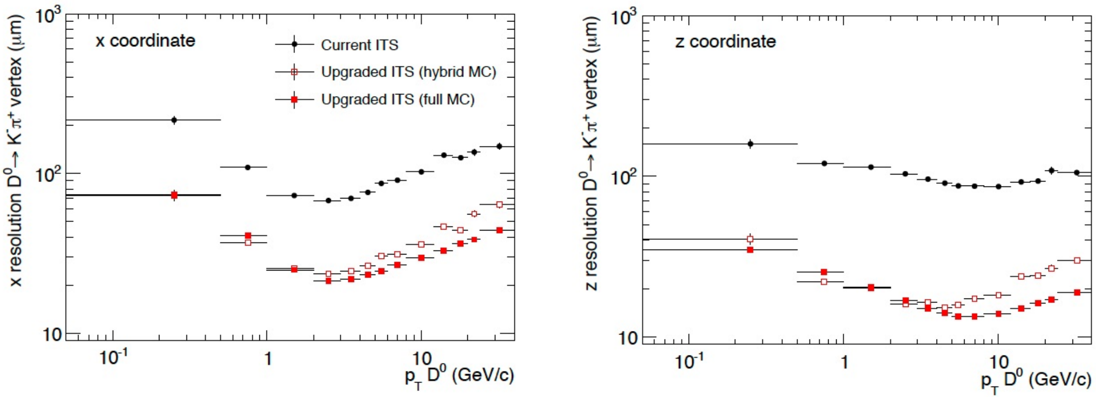

Figure 1.4: *Left: D^0 vertex resolution along x traversal axis. Right: D^0 vertex resolution along beam axis z. [1]. [1]. Old ITS (black) is called "Current ITS", ITS2 (red) is called "Upgraded ITS".*

The ITS2 layers are organized in 2 groups (Figure 1.2, right): the Inner Barrel (IB) consists of the three innermost layers, while the Outer Barrel (OB) contains the four outermost layers.

ITS2 layers are azimuthally segmented in staves which are fixed to a support structure, half-wheel shaped, to form the Half-Layers. The stave of the Outer Barrel is further segmented in azimuth in two halves, named Half-Staves. In total there are 48 Staves in the IB and 144 Staves in the OB [1].

This detector has a total active area of ~ 10 m^2 segmented in 12.5 billion pixels. It represents the largest scale application of MAPS in a high-energy physics experiment.

The ITS2 replaced a previous tracker [6] consisting of six cylindrical layers of silicon detectors placed co-axially around the beam pipe located at radii between 39 mm and 430 mm. The two innermost layers were made of hybrid silicon pixel sensors, the two middle layers were made of Silicon Drift Detectors and the two outermost layers were equipped with double-sided Silicon micro-Strip Detectors.

The radius of the innermost layer of the ITS2 was reduced to 22 mm and the material budget in terms of radiation length (X_0) of the ITS2 was greatly improved (for the inner layers from $1.14\%X_0$ to $0.3\%X_0$ per layer). The spatial resolution of the MAPS sensors is ~ 3 times better than the previous hybrid sensors.

This allowed the impact parameter resolution to be improved by a factor of three in the transverse plane (e.g. from 150 μm to 50 μm for $p_T \sim 0.5$ GeV/c [5], as shown in Figure 1.3, left) for $p_T < 1$ GeV/c. In this way measurements of heavy-flavour mesons and baryons can be performed with high precision down to zero p_T. As an example, Figure 1.4 shows the improvement in the reconstruction of the D^0 vertex.

The tracking efficiency of ITS2 is also significantly better for $p_T < 1$ GeV/c as shown in Figure 1.3, right.

1.2 Pixel Chamber: a MAPS active target for tracking and vertexing

Present silicon trackers do not provide a continuous tracking. Bubble chambers provide a continuous tracking with good spatial resolution of the order of tens of microns. These are chambers filled with an overheated liquid at very high pressure. A charged particle that passes through this liquid with sufficient energy ionises many of its atoms. Along the path of the particle the liquid boils and forms bubbles. It is then possible to obtain stereoscopic images of the tracks by taking photographs from different angles to the ionized liquid.

Many discoveries fundamental to particle physics have been made using bubble chambers like the weak neutral currents at Gargamelle [7] or the first observation of a strange particle [8] (Figure 1.5). However, bubble chambers do not have good temporal resolution (O(ms)) which is not suitable for experiments requiring a much larger event rate to study rare processes like charm and beauty processes.

A silicon-based active-target capable to provide a continuous tracking for imaging of open charm and open beauty particles in three dimensions, similar to a bubble chamber, does not exist yet. While the first ideas have been put forward already almost 40 years ago [9], the required technology became available only very recently.

It is from the basic concept of bubble chamber that the idea of Pixel Chamber [10, 11, 12] was born. Pixel Chamber is conceived to be the first bubble chamber-like high-granularity active-target based on silicon pixel sensors, capable to perform continuous, high-resolution (O(μm)) three dimensional tracking.

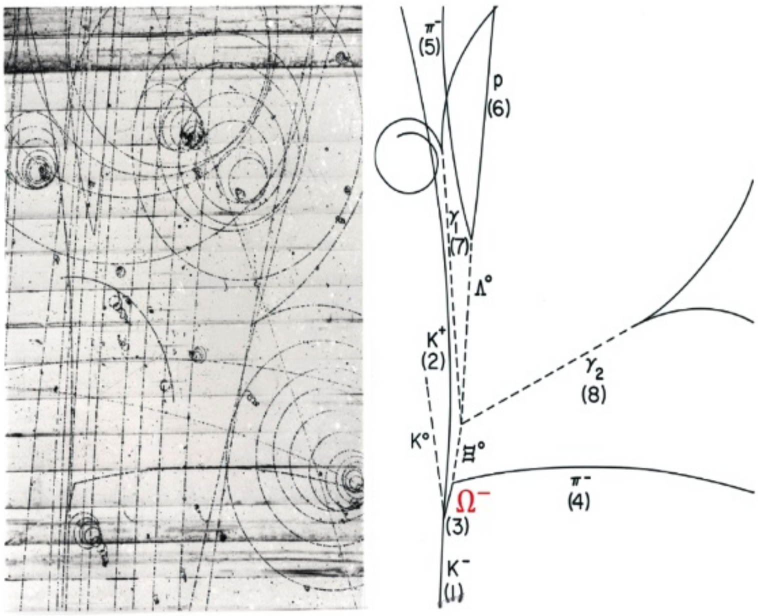

Figure 1.5: *Image of the* Ω^- *discover with a bubble chamber [8].*

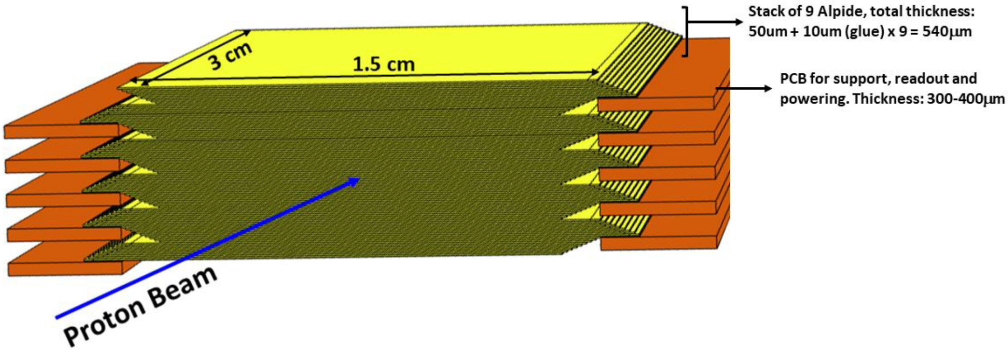

Figure 1.6: *Pixel Chamber stack.*

A three dimensional pixel volume might be created by a stack of silicon pixel sensors glued together. Figure 1.6 illustrates the concept with a stack of several hundreds of ALPIDE sensors glued together, providing a very high granularity capable of performing a three dimensional tracking. The beam interacts in the detector itself which also serves as a target.

Figure 1.7 shows a Geant4 simulation of p-Si interaction with the production of a D^+ meson inside Pixel Chamber. In this case, Pixel Chamber acts as an active target and hosts the primary interaction point for the production of D^+ meson. The continuous tracking capability of Pixel Chamber enables the imaging of the secondary vertices showing the decay of D^+ to a kaon and a pion. Thus,

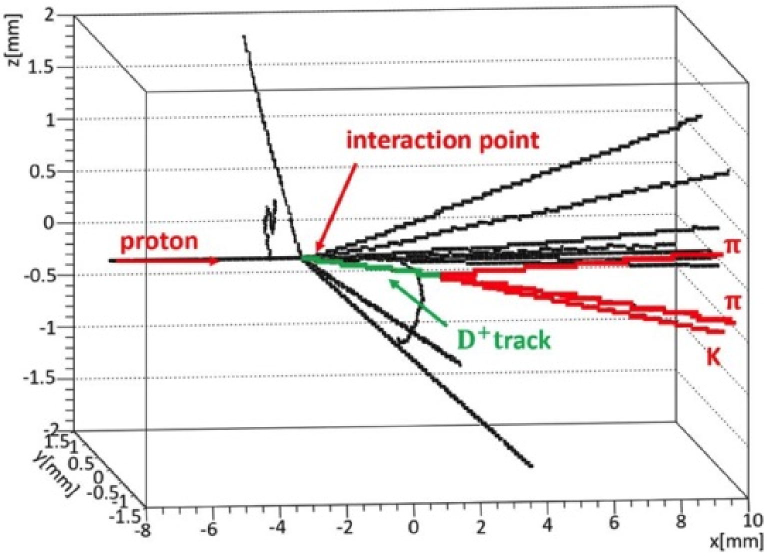

Figure 1.7: *Geant4 simulation of p-Si interaction with the production of a D^+ meson inside Pixel Chamber.*

a device like Pixel Chamber could eliminate the intrinsic limitations of traditional vertex detectors and provide improvements to precision studies for charm and beauty particles.

1.3 Thesis outline

This thesis is organised as follows. Chapter 2 gives a short overview of silicon pixel sensors. Differences between hybrid sensors and monolithic sensors is underlined and the ALPIDE sensor is described in detail. Chapter 3 illustrates the Pixel Chamber architecture starting from its basic unit called A9 stack. In chapter 4 cooling studies are described. In chapter 5, algorithms for tracking and vertexing are discussed. The performances have been studied with Geant4 simulations considering a proton beam at 400 GeV (SPS energies) interacting inside Pixel Chamber. Chapter 6 describes the capability of the tracking algorithm to reconstruct tracks in a single ALPIDE sensor using data from test beams. Finally, chapter 6.3.2 gives a summary of the work done and an outlook on the next steps of the Pixel Chamber project.

Chapter 2

Silicon pixel sensors

Pixel sensors are semiconductor detectors characterized by a two-dimensional segmentation of the sensitive area. Pixel sensors are composed of an active area which consists of a matrix of nearly identical rectangular or squared pixels and of a chip periphery which controls the active area. The sensor chip contains pads for power, readout and control. The active area contains the sensitive elements in which the signal is formed and the front-end circuits used for the amplification of the signal to be read. Depending on the pixel type, other features can be implemented in the pixel itself such as shaping, buffer and registers.

To simplify the readout architecture, the pixels are often organized in groups (usually columns) readout by the same circuitry. In that case, the chip periphery has to readout data from a number of channels much lower than the number of pixels.

Data readout by the chip periphery is compressed, buffered and transmitted to the external data acquisition system. The front-end circuit and the architecture of the chip periphery are strongly dependent on the type of application to which pixel chips are destined.

2.1 Hybrid Pixel Sensors

Hybrid pixel sensors (HPS) dominated the past 20 years and are still widely used in high-energy physics experiments. In HPS, the silicon sensor is bump-bonded on the readout chip. The two chips are produced in two different silicon wafers (Figure 2.1). The advantage of this configuration is that the sensor and front-end electronics can be developed separately and there are several technological options provided by the semiconductor industry.

Full depletion can be reached in these devices by applying a high reverse voltage on the back plane of the sensor (10-100 V). This has a strong impact on the performance of the sensor because almost all the sensor volume becomes sensitive. This enables the possibility to collect charge by drift which translates into fast charge

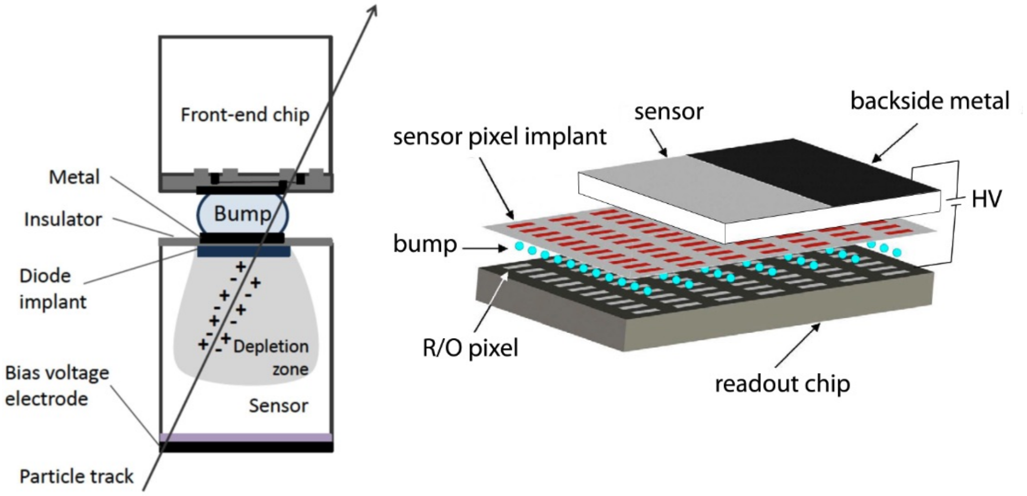

Figure 2.1: *Left: Scheme of a hybrid pixel. Right: pixel matrix. The front-end electronics is implemented in a separate chip bump-bonded to the sensor.*

collection and temporal response (the Giga Tracker of NA62 provides single-hit timing with 200 ps RMS resolution [13]) and hence less sensitivity to radiation damage (10^{16} equivalent neutrons (n_{eq}) per cm^2 for the new sensors designed for HL-LHC [14]).

The in-pixel circuitry is typically fast and rather complex, consisting in a full analog-digital chain that often employs fast ADCs and multi-event buffers.

A limitation of HPS is that the total thickness of the sensor and readout chip is several hundreds of microns. Moreover the bump-bonding of the two wafers requires that there must be exact matching between the size of the front-end circuits and the size of the sensing element because each sensing element has to be connected to its respective front-end circuit. This poses several constraints in the design of the detector. The required silicon and the bump-bonding technique make them very expensive, a severe limitation for large area detectors. In addition, the pixel size is limited by the bump-bonding technology. In state-of-the-art sensors, the pixel pitch is limited to $\sim$ 50µm. Power consumption is considerably high ($\sim$ 30 mW/mm^2) which calls for the adoption of high material budget cooling systems.

2.2 Monolithic Active Pixel Sensors

In a Monolithic Active Pixel Sensor (MAPS), as the name suggests, the active area (epitaxial layer) and the front-end circuitry in the pixel cell are etched on the same silicon substrate (Figure 2.2). This eliminates the bump-bonding, thus reducing the production cost with respect to the hybrid sensors (30-50% lower than hybrids). MAPS have excellent spatial resolution and a thickness reduced to tens of microns

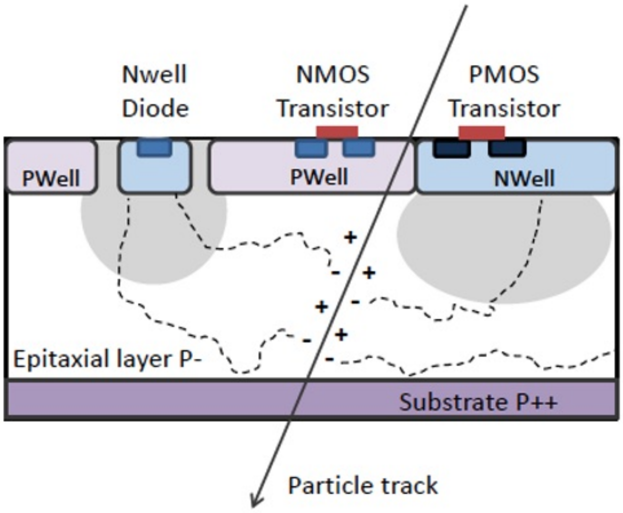

Figure 2.2: *Scheme of a Monolithic Active Pixel Sensor.*

making them suitable for applications requiring low material budget.

The main components of a MAPS in a standard CMOS process are shown in Figure 2.2.

- The substrate is the deepest layer of the sensor. It is highly doped (p-type) and provides mechanical stability to the other structures.
- The epitaxial layer is lightly doped (p-type) and forms the active volume of the sensor. In this layer charge carriers are generated from the passage of a charged particle. It is grown on the top of the substrate and hosts the active devices.
- Well implantations are used as bulk for the Field Effect Transistors. They host PMOS and NMOS transistors.
- The collection diode collects the charge generated in the epitaxial layer. The depleted region is formed at the junction between the n-well diode and and the p-epitaxial layer.

The depletion region is shown schematically in Figure 2.2 as the grey zone under the n-well diode. In that region, signal charge moves and is collected primarily by drift, while outside this region charge moves primarily by diffusion. Moreover, the n-well of the PMOS transistor can collect electrons that are diffused in the epitaxial layer causing a loss of information.

One solution is offered by the 180 nm technology provided by TowerJazz [4]. This technology allows to deposit a deep highly doped p-well (Figure 2.3) layer under the n-well of the PMOS transistor in order to avoid the loss of charge. The

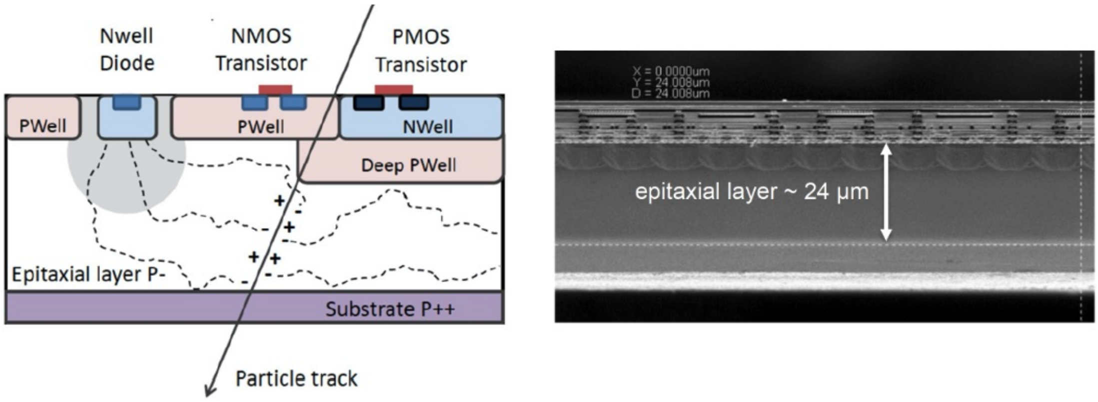

Figure 2.3: *Left: MAPS cell with the addition of deep p-well that prevents the n-well of the PMOS to collect charge. Right: SEM (Scanning Electron Microscope) picture of an ALPIDE sensor [15]*

.

size of the deep p-well can be chosen in order to optimize the signal to noise ratio, the charge collection efficiency and this allows moderately complex in-pixel circuitry - amplification, shaping, discrimination and buffering. Taking all these features into account, the Towerjazz 180 nm technology has been selected for the development of the ALPIDE sensor for the new ITS2 of the ALICE experiment at CERN. ALPIDE sensors will also be used for the realization of Pixel Chamber.

The resulting depletion region, with the p-well architecture is shown in Figure 2.3 as the grey zone. Even though the charge collection efficiency improves with this configuration, the diffusive component of the charge collection still remains dominant, degrading both the time response and radiation tolerance of the sensor.

2.2.1 The ALPIDE sensor

ALPIDE (ALICE PIxel DEtector) is a monolithic pixel sensor developed using the TowerJazz 180 nm CMOS imaging process[2, 3]. It covers an area of 15x30 mm^2 and contains a matrix of 512x1024 pixels with a pitch of 29.24x26.88 μm^2. The small thickness (50 μm) and low power density provides a very low material budget (0.3%X_0) for the innermost layers of ITS2. It is designed to readout 100 kHz of Pb-Pb interactions and provides a radiation hardness of around 10^{13} n_{eq}/cm^2. The ALPIDE time resolution is 2-4 μs [16, 17].

Each pixel cell consists of a sensing diode, a front-end amplifying and shaping stage and a discriminator. It also includes three hit storage registers (Multi Event Buffer), a pixel masking register and pulsing logic (Figure 2.4).

The principle of operation of the analog front-end producing an in-pixel binary information (hit/not hit) is shown in Figure 2.4. When the signal charge generated by a particle hit is collected on the sensing node, the signal is amplified and presented

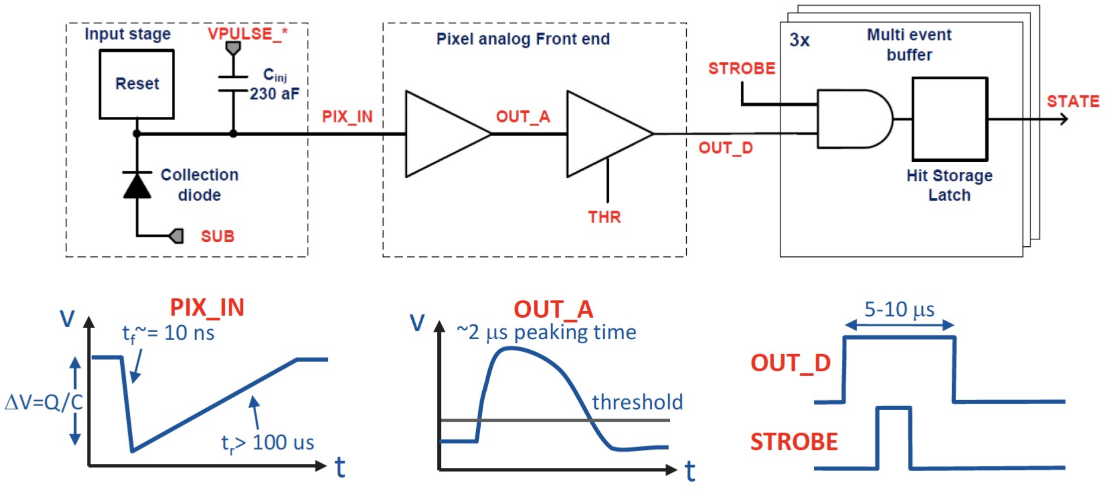

Figure 2.4: *Block diagram of the ALPIDE pixel cell [3].*

to a discriminator which compares the signal to a threshold and outputs a logic 1 only when the signal exceeds this threshold.

The front-end and the discriminator are continuously active. The discriminator features a non-linear response and its transistors are biased in weak inversion. Their total power consumption is just 40 nW. The small signal gain of the front-end is 4 mV/e, the Equivalent Noise Charge is 3.9 e^- and the minimum threshold is below 100 e^-. The typical value of the capacitance of the sensing diode is 2.5 fF. The input capacitance of the front-end is below 2 fF.

The circuit can be operated in continuous or triggered mode. In the second case, only upon the arrival of a trigger signal, the output of the front-end is latched. The front-end is therefore used as a memory or delay line as it maintains the hit information during the shaping or integration time. Afterwards, the latched hit information has to be extracted from the pixel matrix.

The output of the front-end has a peaking time of the order of $\sim$ µs, while the discriminated pulse has a typical duration of 10 µs. The comparator can be configured with such a rather slow response with a settling time of about few $\sim$ µs to minimise its power consumption, as indicated by the stringent requirements for the apparatus.

The readout of pixel hit data from the matrix is based on a circuit named Priority Encoder (PE). There are five hundred and twelve such circuits, one every two pixel columns. The PE provides to the periphery the address of the first pixel with a hit in its double column. During one hit transfer cycle a pixel with a hit is selected, its address is generated and transmitted to the periphery and finally the in-pixel memory element is reset. This cycle is repeated until the addresses of all pixels initially present in a valid hit at the inputs of a Priority Encoder have been

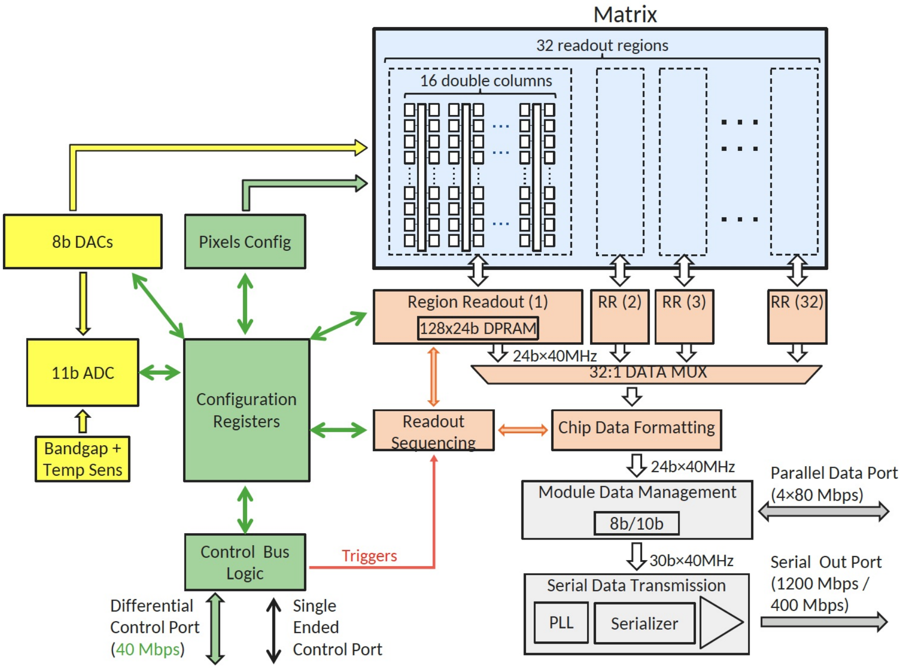

Figure 2.5: *ALPIDE sensor block diagram [3].*

transferred to the periphery. The transfer of the frame data from the matrix to the periphery is therefore zero-suppressed.

Each PE is implemented in a very narrow region between the pixels, extending vertically over the full height of the columns. There is no free running clock distributed in the matrix and there is no signalling activity if there are no hits to read out. The PE also implements the buffering and distribution of readout and configuration signals to the pixels.

The readout of the matrix is organized in thirty-two regions (512x32 pixels), each of them with sixteen double columns being read out by sixteen PE circuits (Figure 2.5). There are thirty-two corresponding readout modules (Region Readout Units) in the chip periphery, each one executing the readout of a submatrix. The sixteen double columns inside each region are read out sequentially, while the thirty-two submatrices are read out in parallel.

The region read out modules include de-randomizing memories and perform additional data reduction and formatting. Two major readout modes are supported, one in which the strobing and readout are triggered externally and a second one in which frames are continuously integrated and read out, with programmable duration of the strobe assertion interval.

Hit data can be transmitted on two different data interfaces according to one of three alternative operating modes envisaged for the application in the Upgraded ALICE ITS: Inner Barrel chip, Outer Barrel Master and Outer Barrel Slave.

The ALPIDE sensor has custom control interfaces. There is a differential control port supporting bi-directional (half duplex) serial signaling at 40 Mb/s on differential links. A second single ended control line is also available. These interfaces and the related control logic enable the interconnection of multiple chips on a multi-point control bus. The Control Management Unit block implements the control layer and provides full access to the control and status registers of the chip as well as to the multi-event memories in the Region Readout Units. The control bus is also used to distribute commands to the chips, most notably the trigger messages. All the analog signals required by the front-ends are generated by a set of on-chip 8 bit DACs. Analog monitoring pads are available to monitor the outputs of the internal DACs.

The analog section of the periphery also contains an ADC with 10-bit dynamic range, a bandgap voltage reference and a temperature sensing circuit. The ADC can be used to monitor several quasi-static internal analog signals: the outputs of the DACs, the analog and digital supply voltages, the bandgap voltage and the temperature sensor.

Chapter 3

Pixel Chamber design

Pixel Chamber would constitute a stack of a few hundreds of ultra-thin pixel sensors on top of each other to provide a continuous three dimensional tracking. The high granularity, low thickness and high spatial resolution makes ALPIDE an excellent candidate for Pixel Chamber. The data, control and clock signals on the ALPIDE can be accessed through peripheral bonding pads on one side. To provide that access, the sensors should be stacked with an offset, providing space for the wire bonding which would be interfaced on a printed circuit board. The detailed architecture of the assembly is described in the next section.

3.1 Pixel Chamber architecture

3.1.1 A9 stack

The basic unit of Pixel Chamber is a stack of nine ALPIDE sensors called the A9 stack. Twenty-four A9 stacks (total 216 ALPIDE sensors) form the entire Pixel Chamber. In the A9 stack, the nine sensors are arranged in a staggered fashion to provide the space for wire bonding of the sensor pads (Figure 3.1). The pads, which provide access to the signal and power circuits of the sensor, reside on one side of the surface of the sensor along its length (Figure 3.2). The offset between sensor layers is 150 µm. Between two sensors there will be a layer of electrically insulating glue with a thickness of about 10 µm. The total thickness of the A9 stack is 540 µm.

The control signals, clock, and data lines to and from the sensor will be interfaced on a Printed Circuit Board (PCB), through wire bonds. The PCB will consist of both rigid and flexible parts, the rigid part being at the bottom of the sensor covering the area of the pads to provide support for the wire bonding. The flexible part will then be used to interface with the data acquisition system, situated at a distance from the Pixel Chamber.

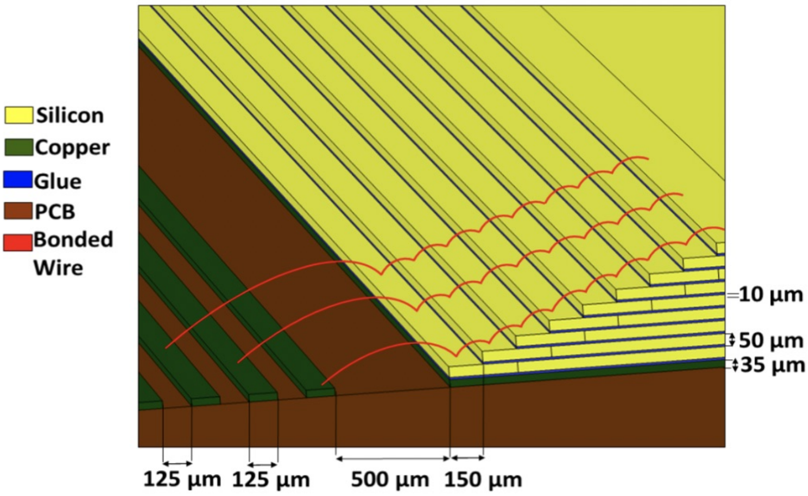

Figure 3.1: *The A9 stack scheme showing the wire bonding of the staggered sensors on a PCB.*

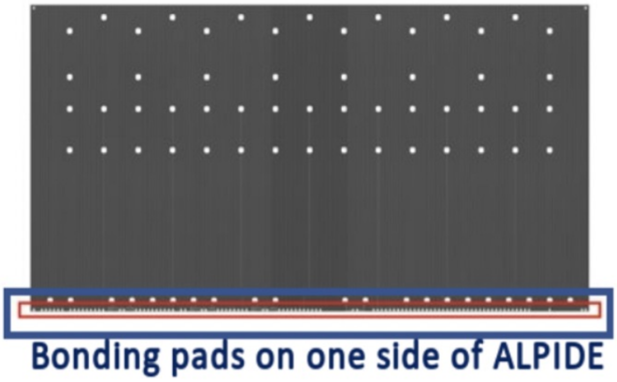

Figure 3.2: *Bonding pads on ALPIDE.*

3.1.2 Data Acquisition

The nine ALPIDE sensors in the A9 stack have individual 1.2 Gbps serial data lines, a shared bi-directional differential control and monitoring line and a shared differential clock line (Figure 3.3, right-bottom). The data, control, monitoring, and clock signals are interfaced on a PCB through wire bonds. The topology is the same as in the ALICE ITS2 Inner Barrel stave, which also hosts nine ALPIDE sensors. The Inner Barrel (IB) stave of ITS2 is readout by the Readout Unit (RU) [2, 18].

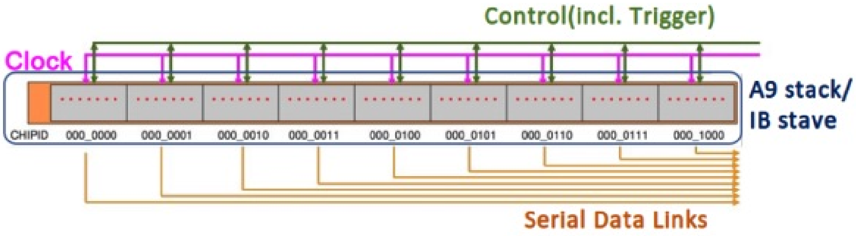

Figure 3.3: *Clock, control and data signals from the A9 stack (the same as the ALICE ITS Inner Barrel stave [2, 18]).*

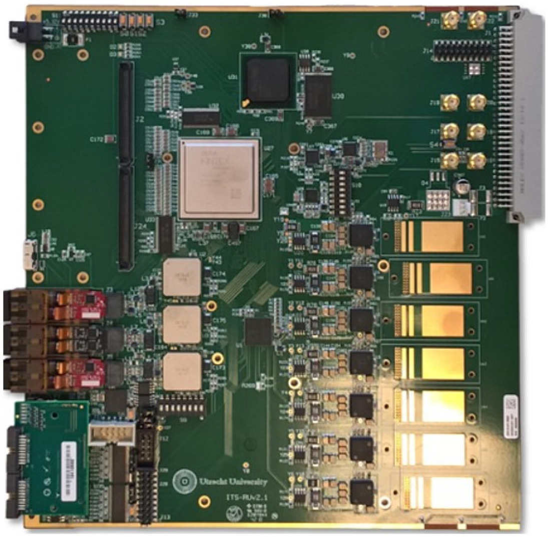

Figure 3.4: *The Readout Unit (RU) of ITS2 [2, 18]. The A9 stack is topologically similar to the ITS2 Inner Barrel stave. Hence the RU can be used to readout the A9 stack.*

The RU is an FPGA based board (Figure 3.4) which interfaces to the IB stave and carries unidirectional clock and serial data (1.2 Gbps) links and bidirectional control links. One RU can readout nine ALPIDE sensors of the ITS2 IB stave and interfaces with the ALICE Detector Control System and the Online-Offline framework. Given the same topology as the ITS2 IB, the A9 stack would also be readout by one RU. Each A9 stack would be connected to a RU by a single flex-PCB through a patch panel.

3.1.3 Pixel Chamber

Pixel Chamber is an assembly of twenty-four A9 stacks. A total of 216 sensors form the full stack of the Pixel Chamber along the scheme shown in Figure 3.5. With

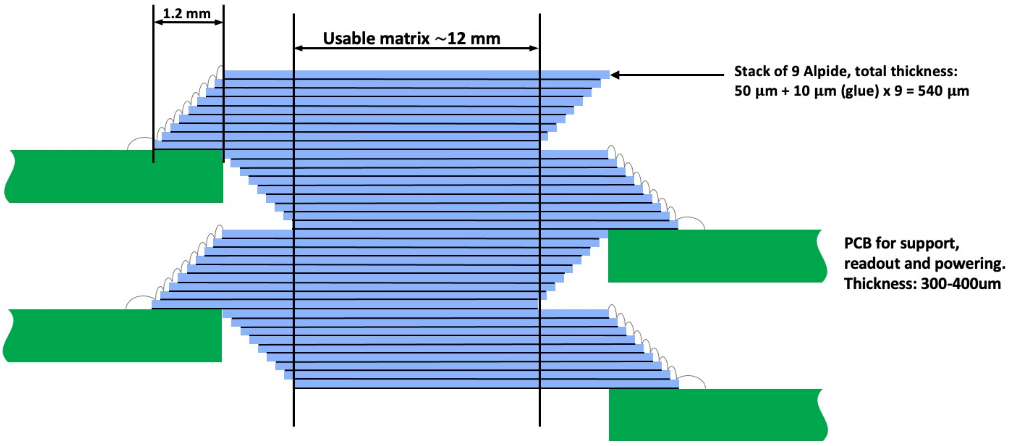

Figure 3.5: *Cross-sectional view of Pixel Chamber composed by an assembly of 24 A9 stacks.*

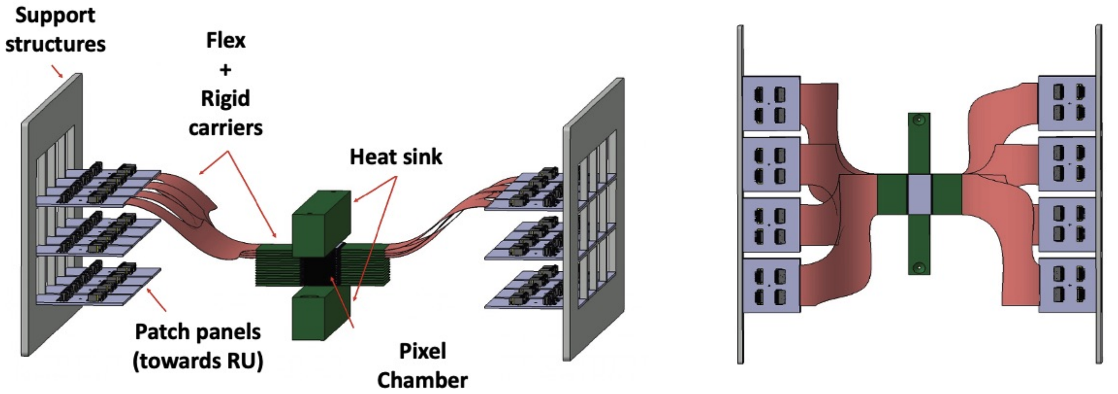

Figure 3.6: *Left: Pixel Chamber integrated with flexible and rigid carriers connected to patch-panels for interfacing with the Readout Unit of ALICE ITS. There are two heat-sinks on the top and bottom of Pixel Chamber. Right: top view of the scheme (the heat-sink is not shown in this view).*

such configuration the thickness of the Pixel Chamber is about 13 mm. The width of the usable active area is 10 mm making the chamber volume to be 30x10x13 mm^3. Signal and power lines will be distributed by a combination of rigid and flex PCBs. The rigid part will host the bonding wires and will extend 1.2 mm inwards from the periphery of the first sensor of the A9 stack (the green layers in Figure 3.5). The flex PCBs will be a continuation of the rigid PCBs and will be connected to a patch panel (Figure 3.6) interfaced to the readout and data acquisition system. There will be twelve PCBs on each side of Pixel Chamber connected to the readout patch panels.

Figure 3.7: *ACCµRATM100 flip-chip bonding machine [20] installed at the University of Geneva [21] which is being used for the preliminary tests for the gluing of the sensors.*

3.2 Towards the first A9 stack prototype

The assembly of the A9 stack and the eventual Pixel Chamber is a complex interplay between mechanics and electronics. The sensors should be precisely aligned, glued and bonded to create the A9 stack.

A 10 µm thick electrically insulating glue between the sensors is considered in the simulations of the Pixel Chamber. In practice, two options are being evaluated. The first option is laminating a 5 µm thick Nitto 5600 [19] acrylic adhesive film on the sensors and stacking them. This glue doesn't provide a permanent mechanical bonding and the individual sensors could be dismounted in case a malfunctioning sensor needs to be replaced. The cooling performance with this solution needs to be investigated. The second option is using an epoxy-based non-conductive film (NCF) of 10-15 µm thickness. This requires a thermal curing for a duration dependent on the temperature. This glue provides a permanent mechanical bonding, and the individual sensors could not be dismounted after the procedure. In both cases, the consecutive sensors need to be aligned precisely in a stack over the glue layer.

Both these options of gluing, along with the alignment and thermal curing could be implemented by a flip-chip bonding machine like the ACCµRATM100 [20]. There is an ongoing collaboration on the gluing studies with CERN and the Particle Physics

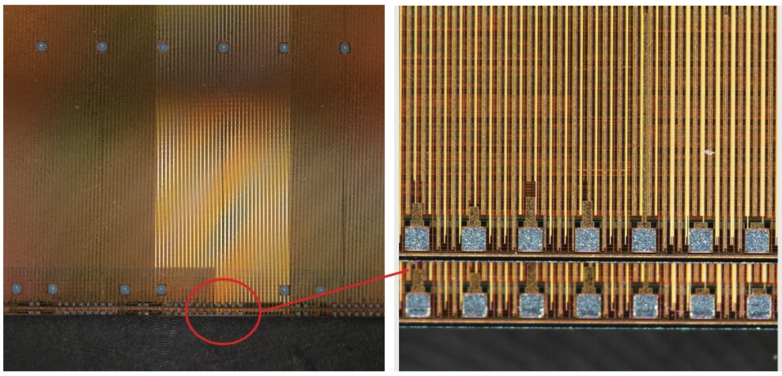

Figure 3.8: *Left: Two ALPIDE sensors glued by Nitto 5600 [19]. Right: Magnified image of the glued sensors showing the peripheral pads.*

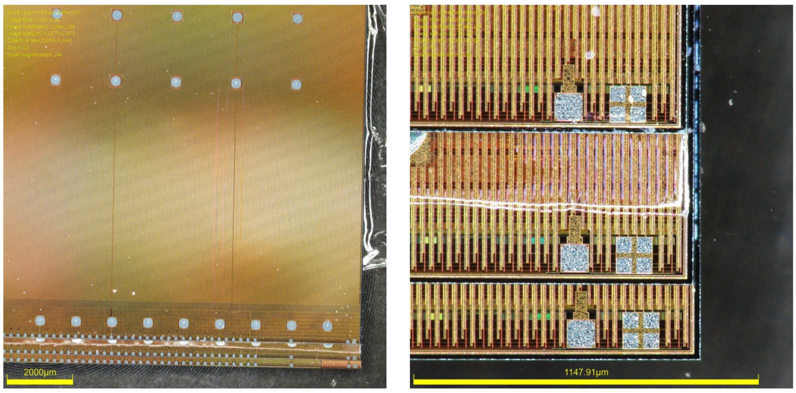

Figure 3.9: *Left: Three ALPIDE sensors glued by Nitto 5600 [19]. Right: Magnified image of the glued sensors showing the peripheral pads.*

Department, University of Geneva [21] where such a machine is installed. The machine, shown in Figure 3.7, can be configured for different bonding profiles based on temperature, force, position and time. The glue is attached to the bonding head which then moves and presses against the sensor placed on the substrate chuck. The position, force and temperature as a function of time are based on the pre-defined bonding profile.

Preliminary trials have started at the University of Geneva [21] using the different options. Some preliminary results from those trials are shown. Figure 3.8 shows two ALPIDE sensors glued by the Nitto 5600 acrylic adhesive film. Figure 3.9 shows three ALPIDE sensors glued together. The bonding profile selected for gluing the three sensors is plotted in Figure 3.10 which shows the force imparted by the bonding head on the sensor and its corresponding position with respect to the idle position as a function of time.

A prototype carrier board for the A9 stack have been developed and is shown in

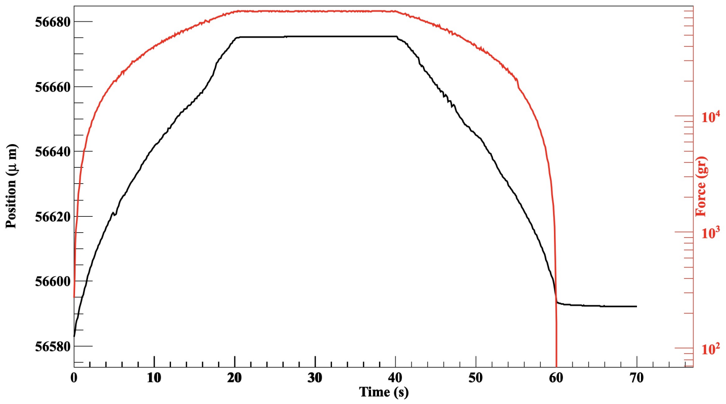

Figure 3.10: *The bonding profile used for the gluing of the three sensors.*

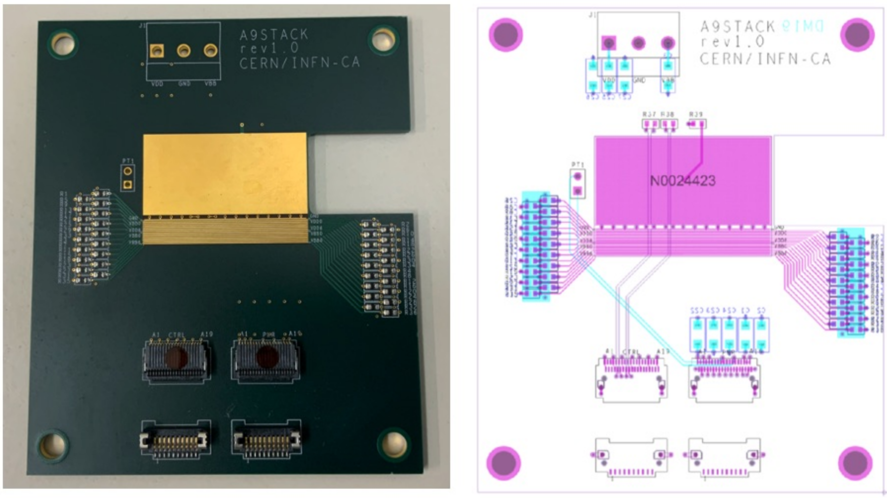

Figure 3.11: *Left: the first prototype of the A9 stack carrier board. Right: carrier board layout*

Figure 3.11. There are separate power lines for each sensor. All the sensors share common clock and control signals. The connector used is Samtec (Micro TCA Up To 20 Gbps FireFly Edge Card Socket Assembly) which interfaces to the RU connector. The first tests using the carrier board are foreseen with one sensor. The validation can be done using the MOSAIC system [22], which has the same interfaces as the RU. After the validation of the board with one sensor, the separately assembled A9 stack would be glued on the carrier board followed by the wire bonding. Detailed functional tests are then foreseen in the laboratory using the MOSAIC system. Once the assembly is qualified, the A9 stack would be studied with beams.

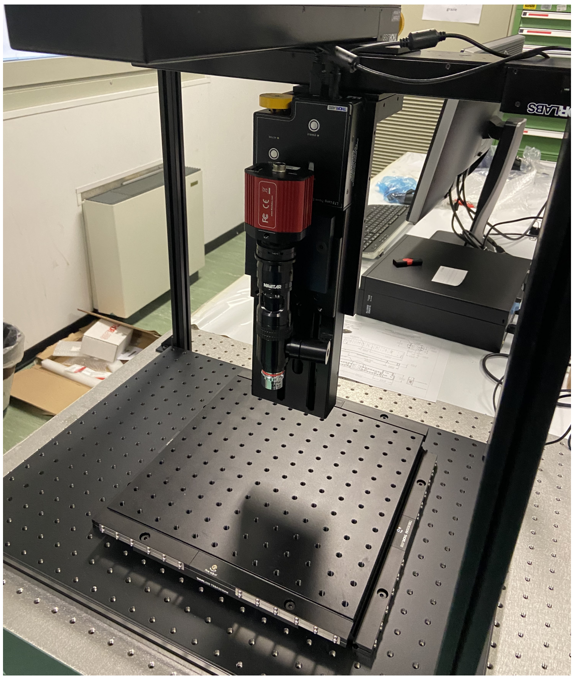

Figure 3.12: *The setup for carrying out the Pixel Chamber assembly with multiple A9 stacks. The setup is installed at INFN, Cagliari.*

3.2.1 Pixel Chamber assembly

After detailed characterization of the A9 stack, the assembly of the Pixel Chamber consisting of multiple A9 stacks would be carried out. The assembly will be carried out on an optical bench, equipped with a 25mm-travel micrometer linear stage, and a 4mm/6° 6-axis stage with differential adjuster. The linear movement will provide coarse position adjustment, while the 6-axis stage will provide precise positioning of the stacks with sub-micron resolution. The optical bench and the stages are produced by Thorlabs.The main components of the positioning system, assembled as shown in Figure 3.12 are:

- MAX601D/M (The Thorlabs 6-Axis NanoMax stages with Differential Adjusters, 6DOF) [23];
- XR25C/M (linear travel 25mm coarse, metric micrometer with 500 µm displacement per revolution) [24];
- Thorlabs Kiralux CS505MU 5MP CMOS camera, 2448x2048 pixels, equipped with a Thorlabs MVL6X12Z 6.5X zoom lens and required adapter tubes [25] will be used to check the positioning ;
- Thorlabs OSL2 halogen fiber optic illuminator [26] will be used to illuminate the working area.

Chapter 4

Pixel Chamber cooling studies

The ALPIDE sensor consumes only 40 mW/cm^2 and without cooling the operation temperature of a single isolated chip is around 30 degrees centigrade at room temperature. With hundreds of ALPIDE sensors stacked in the Pixel Chamber, the increase of temperature can be critical and merits detailed studies to estimate probable effects and practical solution. A preliminary study on cooling has been carried out to keep the temperature of the entire stack to less than 40°C [27]. It will be described in detail in this chapter.

In order to study the temperature as a function of the position within the stack of the ALPIDE sensors and deriving the temperature gradient, a numerical simulation has been developed with COMSOL Multiphysics [28, 29], a commercial finite element [30] software package designed to address a wide range of physical phenomena. COMSOL Multiphysics allows conventional physics-based user interfaces and coupled systems of partial differential equations. It provides an integrated development environment and unified work flow for electrical, mechanical, fluidodynamical, acoustics and chemical applications.

The implementation of a simulation starts identifying a physical process. It is then necessary to develop a mathematical description of this process, discretise the model into an algebraic system, solve this system and finally process the data. The geometry is modelled into small pieces over which it is possible to write a set of equations describing the solution to the governing equation. A governing equation describes the major physical mechanisms and processes without further revealing the change and non-linearity of the material properties.

The Pixel Chamber cooling simulations involve a heat transfer problem. In this case, the governing equation describes a process in which the thermal energy at an infinitesimal point or a representative element volume is changed due to energy transferred from surrounding points via conduction, convection, radiation, and internal heat sources or any combinations of these four heat transfer mechanisms. The response of the whole system is then inferred by modelling it as an assemblage of several small volumes assembling the collection of all elements.

The simulation reference system is defined as follow: x axis is along the long side of the chip; y axis is along the short side of the chip; z axis is along the sensor thickness.

4.1 Single ALPIDE simulation

The ALPIDE power consumption values have been assumed according to the Inner Barrel chip characteristics [31]:

$$\text{Analog power} = 27 \text{ mW} \tag{4.1}$$
$$\text{Digital power} = 173.25 \text{ mW} \tag{4.2}$$

The simulation is developed starting from a single ALPIDE sensor. The geometry includes the silicon chip, the carrier board and copper strip (Figure 4.1).

The dimensions are:

- chip: 30x15x0.05 mm^3;
- carrier board: 70x70x1.8 mm^3;
- copper strip: 37x17x0.035 mm^3.

Analog and digital power have been assigned uniformly to silicon chip as the heat source (eq. (4.1), (4.2)).

The chip is placed in an air volume of 1 m^3 at room temperature of 23°C with an airflow along x-y axes with a velocity of 0.1 m/s (still air). The temperature of the chip increases from the start temperature for $\sim$ 10 minutes, then it reaches the stability at a value of 29.8°C which is in agreement with the experimental value of $\sim$ 30°C (Figure 4.2).

4.2 A9 stack simulation

The next step is the A9 stack simulation. The carrier board for the A9 stack (Figure 3.11) has also been considered for the A9 simulation. The dimensions of every single chip, copper strip and the PCB carrier board are the same as that of the single chip simulation. The nine sensors are arranged in a staggered fashion (Figure 4.3, right). Analogue and digital power are the same of eqq. (4.1), (4.2). The A9 stack COMSOL implementation is shown in Figure 4.3.

With the simulation conditions (room dimensions, air flow) as the single chip configuration, the temperature increases at a maximum value of 97.8°C.

To reduce temperature of the A9 stack, an airflow cooling is considered. The flow velocity is varied from 1 to 2 m/s. Different conditions are considered. If the air flow is set to 1 m/s along the y axis and from the bonding side direction the stable

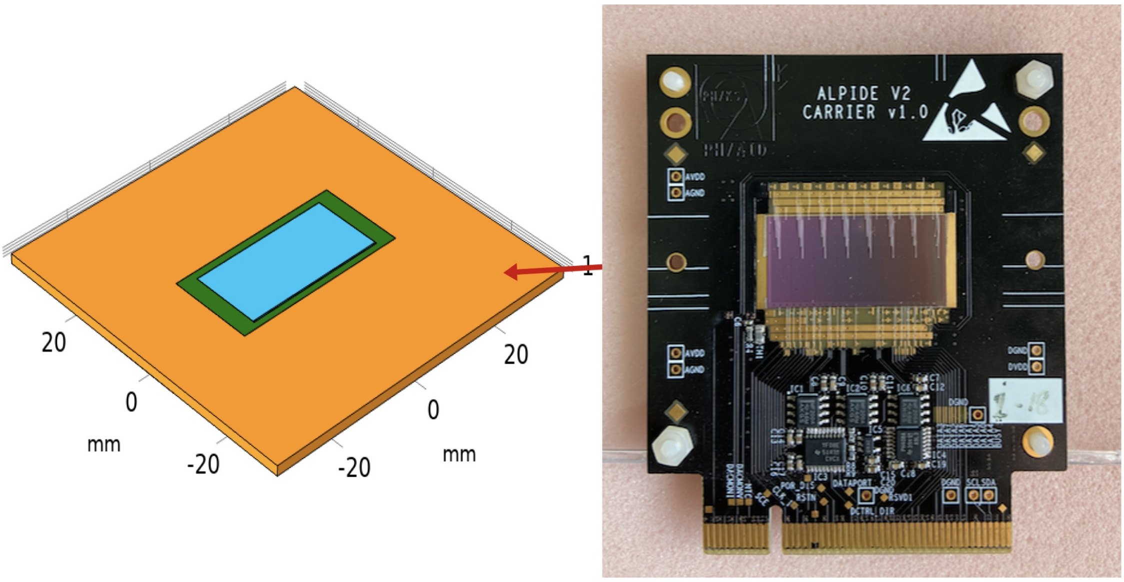

Figure 4.1: *Left: Simulation model of single ALPIDE sensor. The blue part is the silicon sensor, green part is copper, orange part is the carrier board. Right: The actual carrier board of single ALPIDE sensor.*

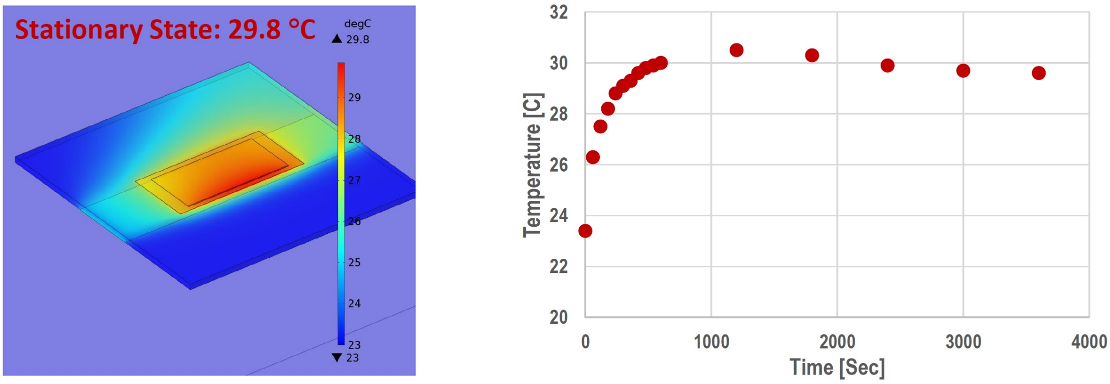

Figure 4.2: *Left: Stabilized temperature profile of single ALPIDE sensor with the carrier board. Right: Variation of temperature as a function of time for a single ALPIDE sensor.*

temperature is reached in 5 minutes and is 47.3°C. If the air flow is set to 2 m/s, along the y direction and from the bonding side direction the stable temperature is reached in 3 minutes and is 37.9°C. Other configurations have been evaluated with air flow at 2 m/s. Some examples are shown in Figure 4.4. The best configuration from the cooling point of view seems to be the one where the air flow arrives on the bonding side (Figure 4.4, top-right). The configuration where it arrives on the

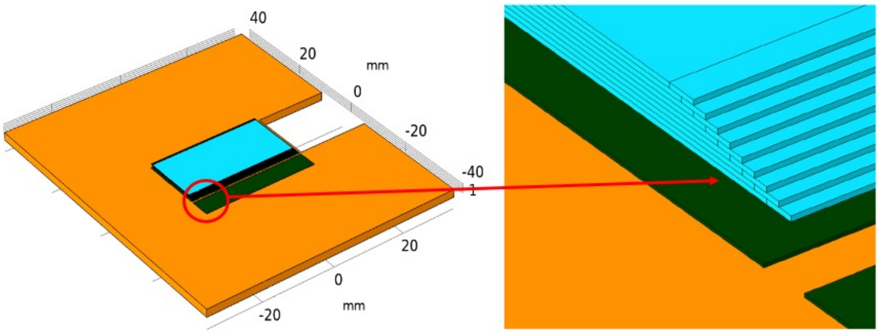

Figure 4.3: *Left: Simulation model of A9 stack with the carrier board. The silicon sensor is shown in blue, the copper strip in green and the carrier board in orange. Right: Magnified view of the nine ALPIDE sensors in the A9 stack placed in a staggered manner.*

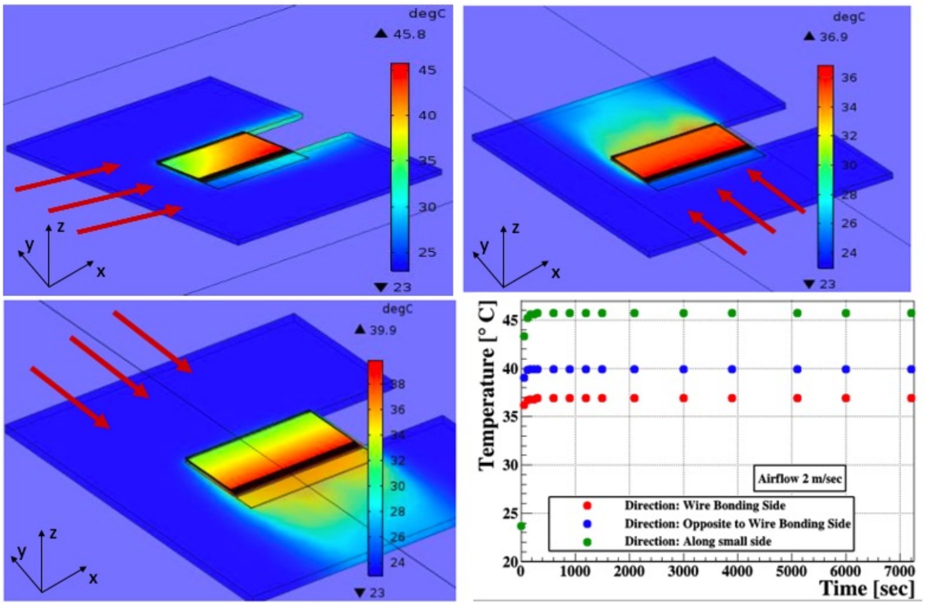

Figure 4.4: *Top, bottom-left: Stabilized temperature profile of A9 stack with an airflow from different directions and velocity of 2 m/s. Bottom-right: Variation of temperature as a function of time for different air flow directions and velocity of 2 m/s.*

opposite side is also acceptable (Figure 4.4, bottom-left). The stabilized temperature in this case is 39.9°C.

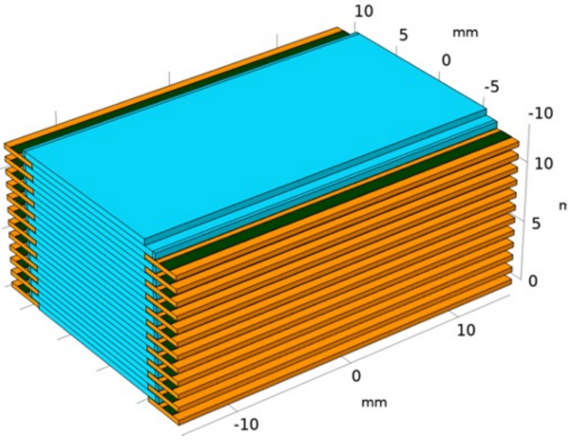

Figure 4.5: *Simulation model of the full Pixel Chamber stack.*

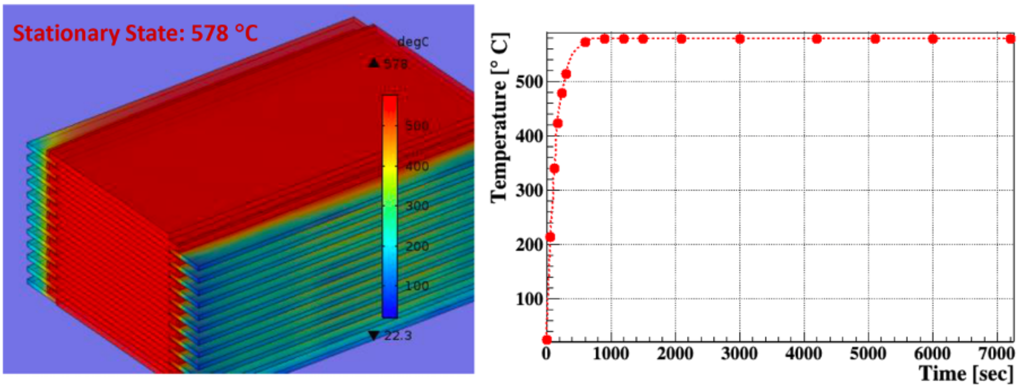

Figure 4.6: *Left: The stabilized temperature profile of the full Pixel Chamber stack without any cooling. Right: Variation of temperature as a function of time for full stack.*

4.3 Full Pixel Chamber stack simulation

A numerical approximation has been made to simulate the entire stack. The A9 stack is approximated to a single chip that has the thickness and the power energy consumption equal to A9. It has been verified that in this approximation, the reached temperatures are the same that are reached without the approximation within 1%. The numerical approximation is computationally easier to handle: it is not needed to simulate 216 ALPIDE sensors, but twenty-four A9 stacks of the same thickness (540 µm) as shown in Figure 4.5. The full Pixel Chamber stack is placed in an air volume of 0.1 m^3. The air flow blows along the x-y axes with a velocity of 1 m/s at a room temperature of 23°C. In this condition, after 15 minutes, the stabilized temperature is 578°C (Figure 4.6). To reduce the temperature of the

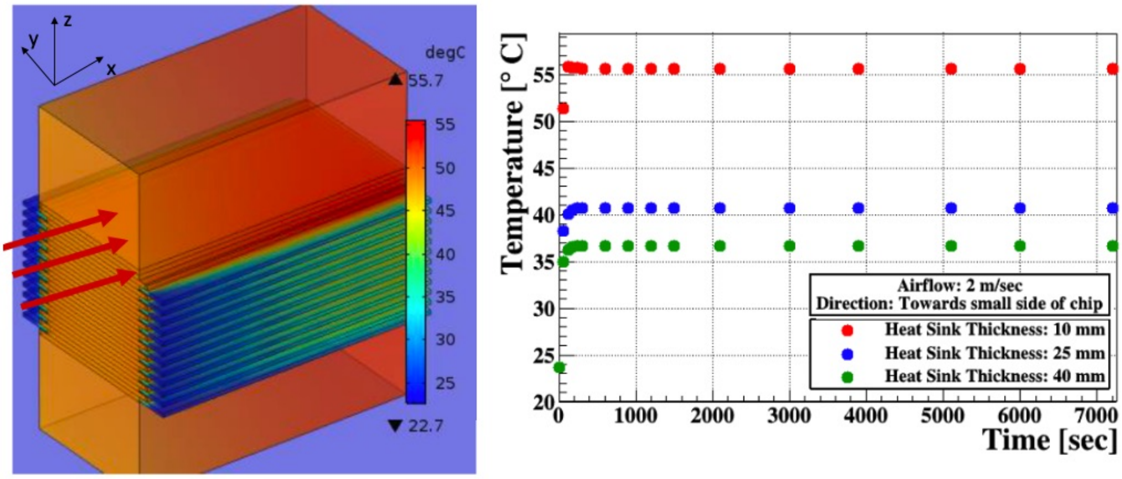

Figure 4.7: *Left: The stabilized temperature profile of full stack with copper heat sinks on top and bottom. Right: Variation of temperature with time for different copper sink thickness.*

Air flow velocity (m/s)	Stabilized temperature (T°C)
No airflow	578
1	168
2	106
3	84.9

Table 4.1: *Summary of air flow cooling stabilized temperatures for the full Pixel Chamber stack.*

stack, an air flow at room temperature (23°C) has been initially considered. The rigid carriers and the patch panel are placed along the longer side of the chip (Figure 3.6). Therefore the air fan has to blow along the long side of the chip (x axis).

Results of air cooling for different air velocities are summarized in tab. 4.1 and show that air cooling is not enough for the efficient operation of the full stack.

To reduce the temperature of the full stack to a reasonable value, copper heat sinks are needed on top and bottom of the stack (Figure 4.7, left). To prevent any damage to the active chips due to the contact with copper sinks, dummy chips both on top and bottom of the stack have been placed. For the dummy chips too, a stack of A9 chips have been considered. Placing the dummy chips have reduced the temperature by 3°C under 3 m/sec airflow compared to the tab. 4.1 value.

In the next step, two copper heat sinks have been placed on top and bottom, respectively. Different thickness values of the copper heat sinks have been considered. An airflow of 2 m/s is chosen. Figure 4.7, left shows an example of the copper heat sink profile temperature. Temperature profiles shown in Figure 4.7, right show that

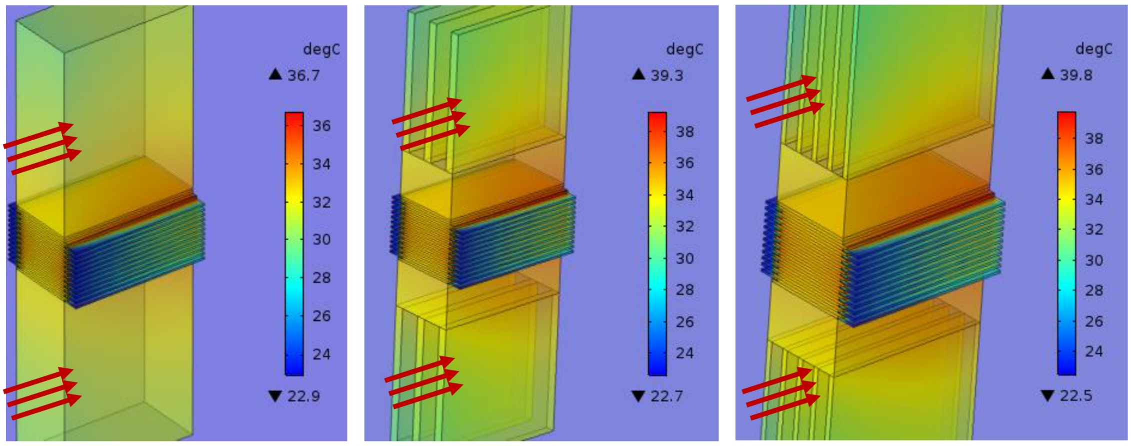

Figure 4.8: *Stabilized temperature profile with an airflow of 2 m/sec for different copper configurations.*

Air flow velocity (m/s)	Stabilized temperature (T°C)	Copper sink
No airflow	578	No
2	106	No
2	36.7	Yes

Table 4.2: *Summary of Pixel Chamber stabilized temperatures.*

the suitable sink thickness to reduce the stack temperature below 40°C, at 36.7°C is 40 mm.

The last step has been to carry out a study to observe the effect of copper fins on the cooling (Figure 4.8). For this, two different models have been considered. In the first case, a 10 mm thick copper plate is used as a base with three 30 mm thick copper fins on top it (total thickness is 40 mm). Each fin has a width of 2 mm with 4.5 mm space in between them. In this case, under 2 m/sec airflow, the stabilized temperature is 39.3°C in comparison to 36.7°C for a single copper plate of the same total thickness. In the second case, the five 30 mm thick copper fins on top of 10 mm thick copper plate have been considered. In this case, each fin has a width of 1 mm with 2.5 mm space in between them and under 2 m/sec airflow, the stabilized temperature is 39.8°C (Figure 4.8). The best solution seems to be the copper sink with 40 mm thickness.

Another check has been performed where air is blown from the bottom. With an airflow of 2 m/s the stabilized temperature is around 51°C so the best configuration is copper sink with 40 mm thickness, airflow 2 m/s at room temperature (23°C) along the x axis. Results are shown in table 4.2.

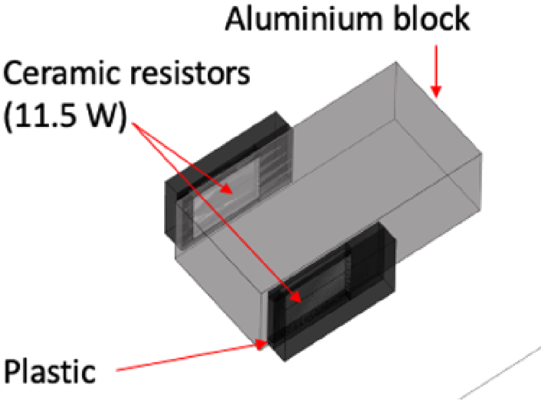

Figure 4.9: *Pixel Chamber simulation model with an aluminium block as the mock sensor. Two ceramic 11.5 W resistors in thermal contact with the two sides of the mock sensor.*

4.4 Experimental validation of the cooling studies

The results of the simulations were validated by laboratory measurements using an aluminum mock-up of Pixel Chamber. Aluminum was chosen because it has thermal properties similar to silicon and can be easily machined. To reproduce the same heating conditions of the Pixel Chamber stack, two ceramic 25 Ω resistors [32], dissipating a power of 11.5 W, are attached to the aluminum block with a double-sided thermal adhesive tape. This is shown in Figure 4.9.

According to a simulation done with COMSOL, the stable heating condition of the aluminium block is reached at 580°C as shown in Figure 4.10, left. This is very similar to the maximum temperature reached by Pixel Chamber which is 578°C. The stabilized temperature of the mock sensor model with an air flow at room temperature (23°C) at 2 m/s is 94.1°C whereas with the real sensor model the temperature is 106°C. The temperature difference between the simulation with the sensor and the mock sensor is $\sim$ 12°C.

Another simulation has been performed to study the cooling of the mock sensor with both the air flow and the copper heat sink. The cooling scheme is shown in Figure 4.11, left. The two copper heat sinks are placed inside two pipes connected to air fans which generate an airflow of 2 m/s each. The sinks are in contact with the mock sensor. With this condition, the stabilized temperature is 33.7 °C (compared to the 36.7°C reached in the same conditions from the real sensor simulation).

As the temperature differences are small the mock-up can be used to validate the cooling simulations in the laboratory.

In the experimental setup, the block temperature is measured using a DS18B20 temperature sensor [33] in thermal contact with the aluminium. The temperature

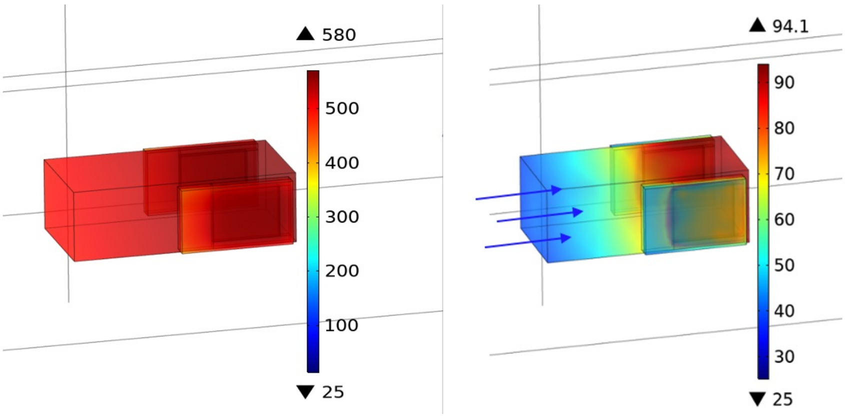

Figure 4.10: *Left: Stabilized temperature of the mock Pixel Chamber without cooling. Right: stabilized temperature of the mock Pixel Chamber with 2 m/s air flow cooling.*

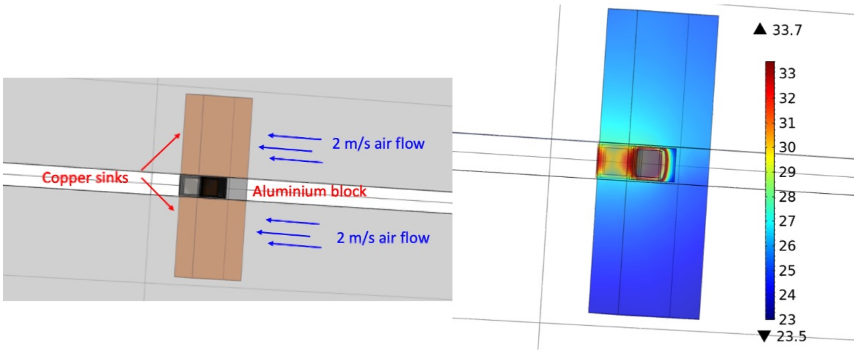

Figure 4.11: *Left: Setup for cooling emulation. Right: Stabilized temperature of the mock Pixel Chamber with 2 m/s air flow cooling and cooper heat sink.*

sensor has a precision of 0.5 °C and range from ∼ -55°C ∼ 125°C. It is connected for bias and data acquisition to a Raspberry Pi [34].

The air flow is provided with SanAce 80W fan [35] and measured with an RS-3893 thermo-anemometer [36] with a resolution of 0.01 m/s.

At the moment measurements were performed for the aluminum mock-up without the copper heat sinks. The setup without the copper heat sinks is shown in Figure 4.12. The air flow is conveyed from the fan to the aluminum block inside a pipe. A 3D printed structure has been realized to host the fan and the anemometer and to connect them to the air pipe.

The equilibrium temperature reached by the aluminum block with an airflow of 2 m/s is 102°C. Figure 4.13 shows the comparison between the temperature variation obtained from the simulation and from the laboratory measurement. The values of the stabilized temperature have a 8% discrepancy showing a reasonable agreement between the experimental measurement and the simulations.

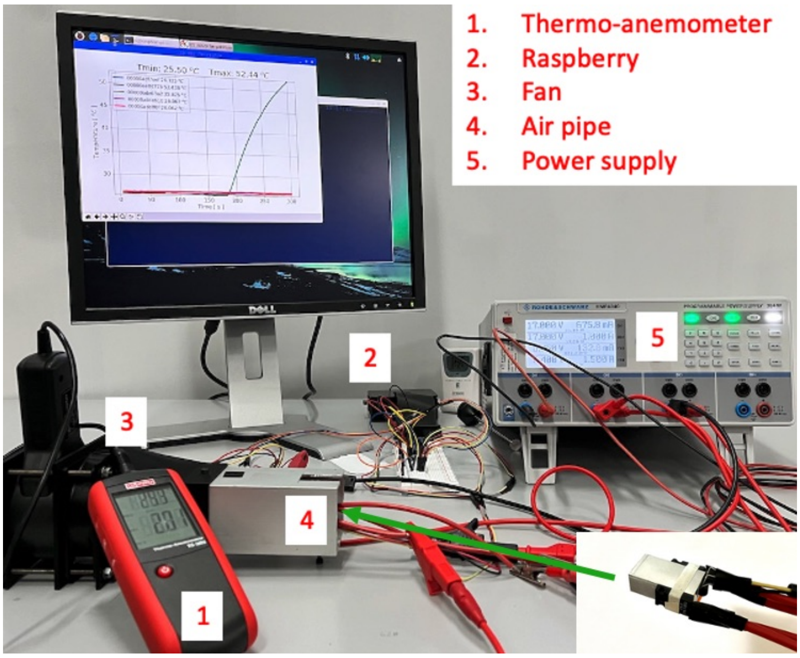

Figure 4.12: *Cooling validation setup. The mock sensor is an aluminium block in thermal contact with two resistors (right bottom) placed inside an air pipe. The air flow is sent towards the block inside the pipe connected to the fan. The temperature sensors are interfaced with a Raspberry Pi. In this setup the copper sinks are not mounted.*

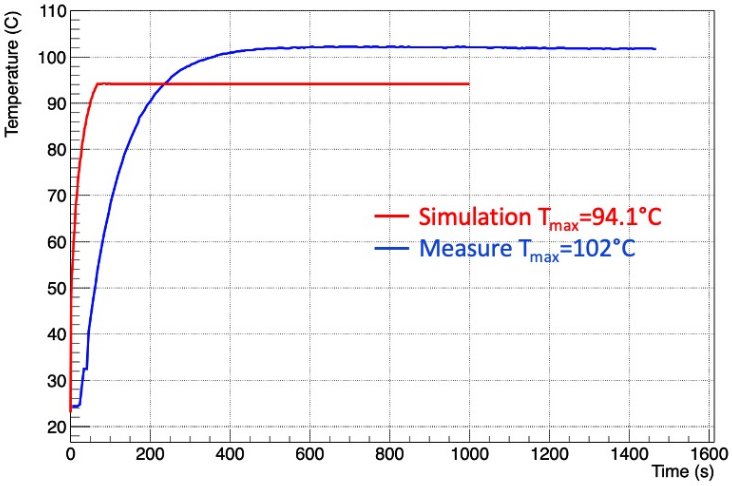

Figure 4.13: *Variation of temperature with time obtained from the mock sensor simulation (red) and from the laboratory measure.*

Chapter 5

Track and vertex reconstruction

This chapter presents a study of algorithms for tracking and vertexing with Pixel Chamber. The performances have been studied in detail with Geant4 simulations of Pixel Chamber.

5.1 Pixel Chamber simulation with Geant4

Geant4 (G4, GEometry ANd Tracking, geometry and tracking) is a platform for simulation of the passage of particles through matter which can be employed in a variety of settings [37, 38].

The Geant4 Simulation Toolkit provides comprehensive detection and modelling capabilities integrated in a flexible structure which provides the possibility to manage in a relativity simple way different aspects of the simulation such as the geometry of the system, the materials involved, the fundamental particles of interest, the generation of primary particles of events, the transport of particles through materials, the physics processes governing particle interactions, the response of sensitive detector components, the generation of event data and so on.

The geometry of Pixel Chamber has been implemented in G4 to simulate a stack of 216 ALPIDE sensors. The reference system is shown in Figure 5.1. The x-axis defines the beam direction, while the y-axis is directed vertically along the stack. The pixel pitch is 29.24 μm along the x axis, 26.88 μm along the z axis and 50 μm along the y-axis (the sensor thickness). The 3D volume has the dimensions of $\sim$ 30x15x11 mm^3 and contains almost 10^8 pixels.

A beam of 400 GeV protons is sent towards the detector front-side to generate p-Si inelastic interactions. The proton beam spot is simulated to be centred in (0,0) on y-z plane with a Gaussian profile with $\sigma = 0.4$ mm. An angular Gaussian spread of 0.02 mm has been simulated as well (Figure 5.2 left and right).

Charm production in p-Si has been also simulated considering D^0 or D$^\pm$ mesons. Since G4 does not foresee the generation of charmed particles in proton interactions, it is necessary to perform a separate simulation in which D particles are generated

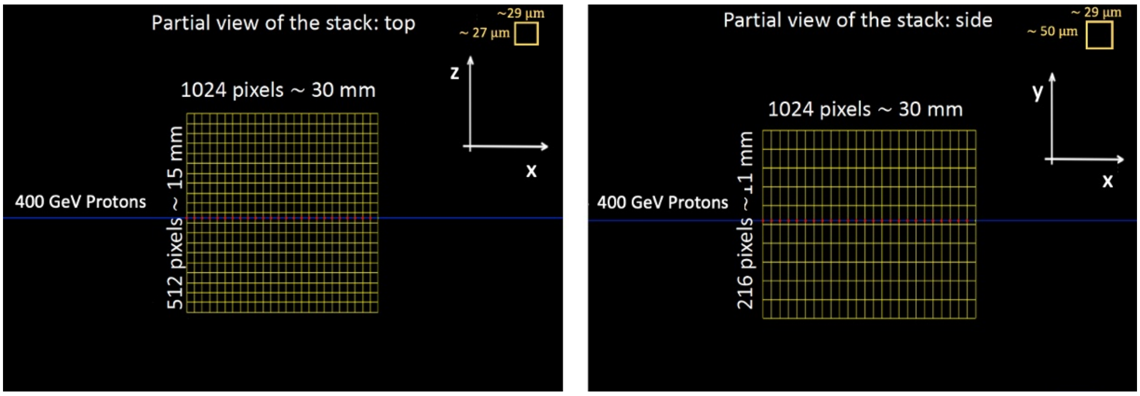

Figure 5.1: *Partial view of the simulated stack on Geant4: left from above, right from side.*

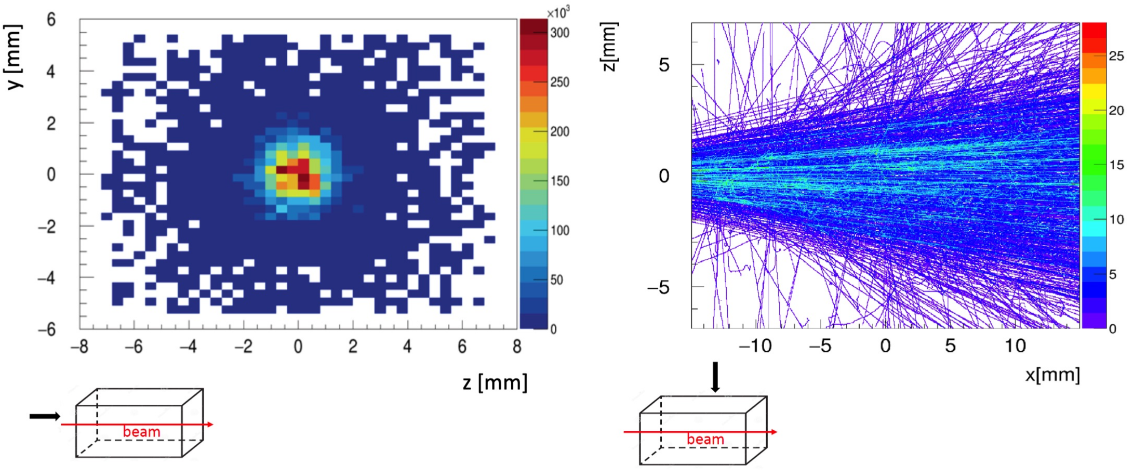

Figure 5.2: *Left: input coordinates of the protons in the y-z plane of the sensor. Right: top view of the proton beam spread.*

in the p-Si interaction point according to the kinematics parameters (rapidity and transverse momentum) evaluated with POWHEG-box event generator [39] for the hard scattering and PYTHIA 6 [40] for the parton shower and hadronization. The POWHEG simulations have been performed with the CTEQ6 PDF and a charm quark mass of 1.5 GeV/c^2. G4 takes care of the tracking and decaying of the charmed particles and decay products. An example of an event with a D^+ decaying to $K^-\pi^+\pi^-$ is shown in Figure 5.3.

In this preliminary study, the charge spread across different pixels is not considered so that the pixel cluster size is one.

From the G4 simulation, a dataset is obtained for particles produced in p-Si interactions, including D decay products. The dataset contains various information

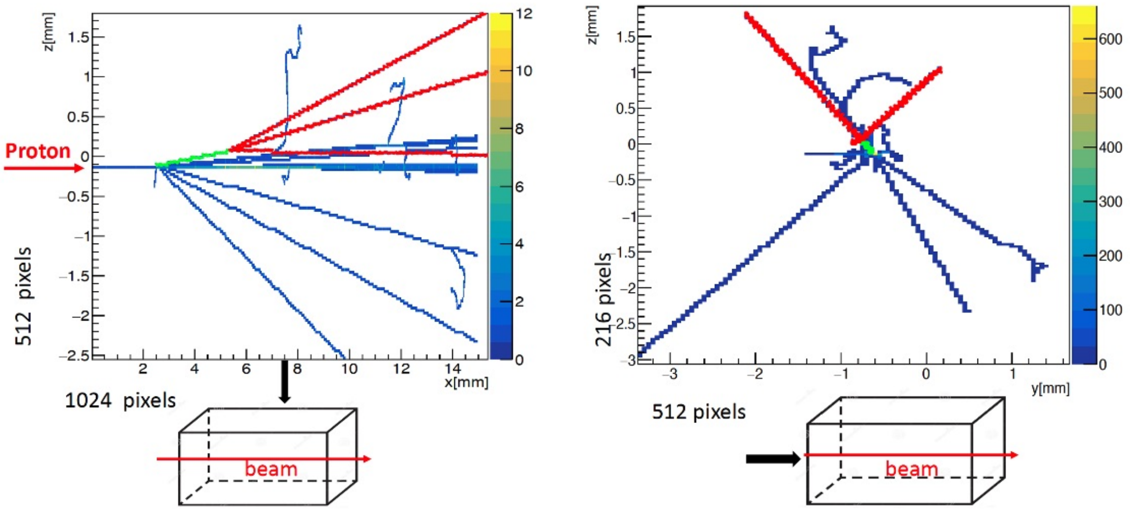

Figure 5.3: *Views from above (left) and from one side (right) of the primary vertex produced by the proton-silicon interaction and the secondary vertex produced by the decay of a* D^+ *in the* $D^+ \rightarrow K^-\pi^+\pi^-$ *channel.*

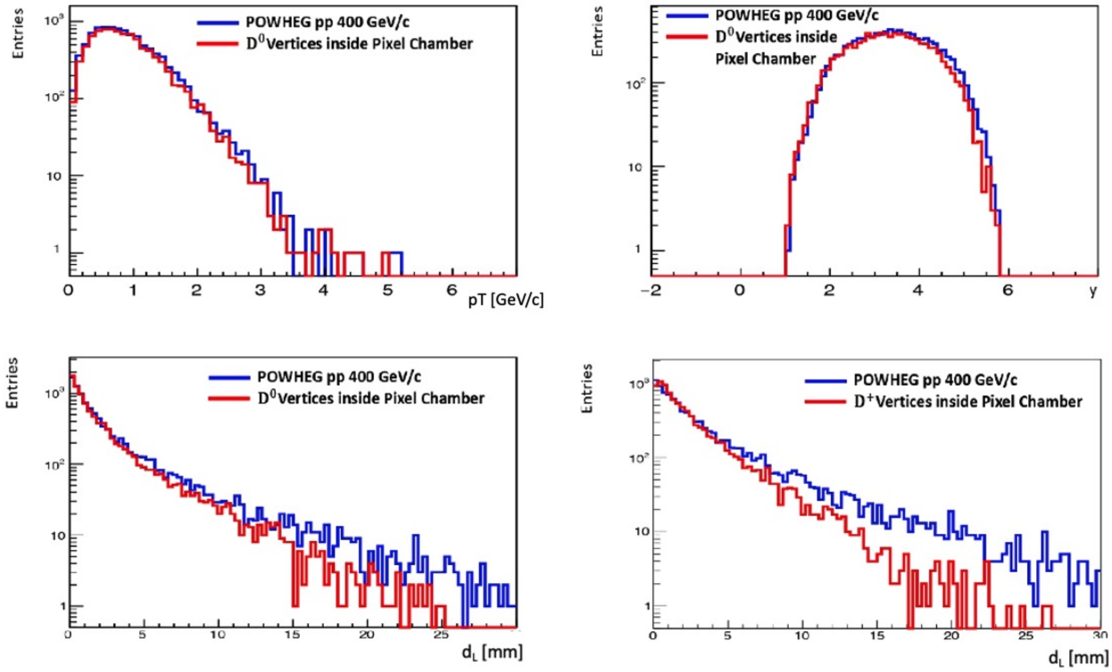

Figure 5.4: *Comparison between the kinematic distributions of the charm particles decayed inside the detector (red) and those obtained by POWHEG (blue).*

including the coordinates of the center of the pixels crossed by a particle (hits) and useful information for the Monte Carlo (MC) truth, such as momentum, energy,

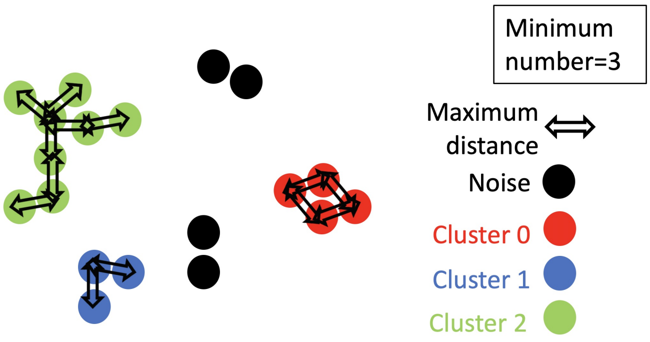

Figure 5.5: *DBSCAN clustering principle*

PDG code and production vertex of the particles that generate a hit in the detector.

Considering the number of pixels contained in Pixel Chamber, an event with p-Si interaction can contain more than $4 \cdot 10^4$ hits.

A study of the y, p_{T} coverage of PixelChamber for charged and neutral D mesons has been performed. Figure 5.4 shows in blue the D meson rapidity y, p_{T} and decay length for the generated events. The y, p_{T} and decay length for particles decayed inside Pixel Chamber are shown in red. About 90% of D^0 produced in interactions inside Pixel Camber decay in the sensitive volume.

5.2 Algorithm for track reconstruction

For the reconstruction of the hadronic tracks produced by a p-Si interaction inside Pixel Chamber, a class library has been developed in C++. The reconstruction of one event containing an inelastic interaction inside Pixel Chamber starts with the tracks reconstruction.

The basic idea is derived from the popular DBSCAN [41] clustering algorithm. This algorithm is based on the concept of hit density: if a pixel has minimum number of neighbours (hit pixels for which the maximum distance does not exceed a fixed value) these are grouped into a cluster as shown in Figure 5.5.

In our algorithm the pixels coordinates are defined in terms of integer indices i, j, k. The minimum distance between neighbours is computed as a discrete distance and is set equal to 1 (Figure 5.6). The algorithm performs the following steps:

1. **Sorting:** The first step of the track reconstruction algorithm is the search of hit pixels neighbours. Since a Pixel Chamber event can contain more than $4 \cdot 10^4$ hits, the search of pixel neighbours for n hits requires a long computational time of the order of n^2.

   To reduce this time, hits are sorted before proceeding with the neighbours search. This operation is performed through a recursive sorting algorithm

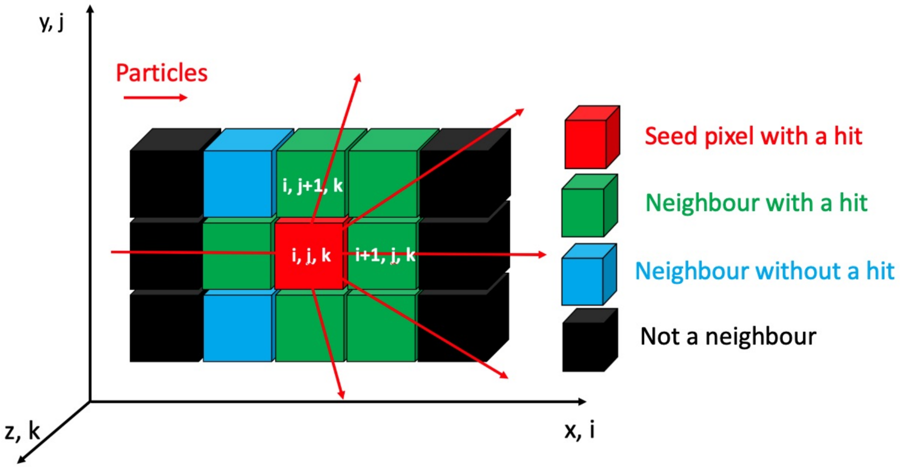

Figure 5.6: *Pixels neighbours.*

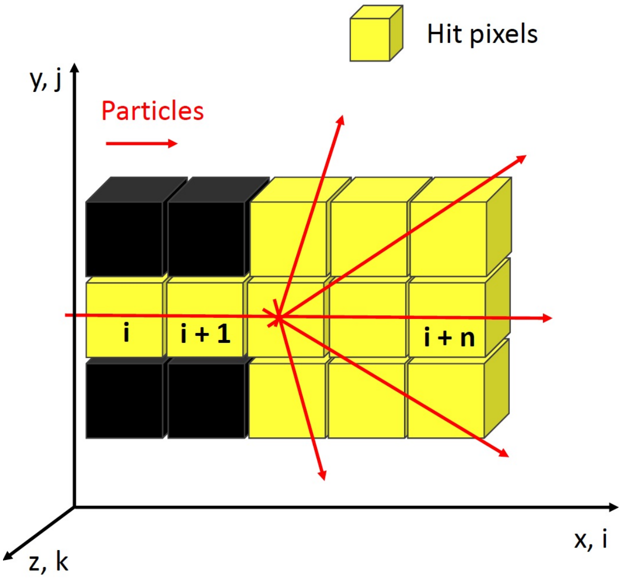

Figure 5.7: *Sorting of hits by index i with a quicksorting algorithm.*

called quicksorting [42] which reorders the hits by increasing x (index i) coordinates (Figure 5.7). This procedure essentially consists in dividing the data vector into smaller vectors and, starting from a first element called pivot, the minor elements (in our case pixels with smaller index i) are put to the left of the pivot and the major ones to the right. The operation is repeated for the two newly created sub vectors and so on until the data is completely sorted. Sorting data using quicksorting takes about n · log(n) cycles to sort n items while the computational time required for the search of neighbours decreases

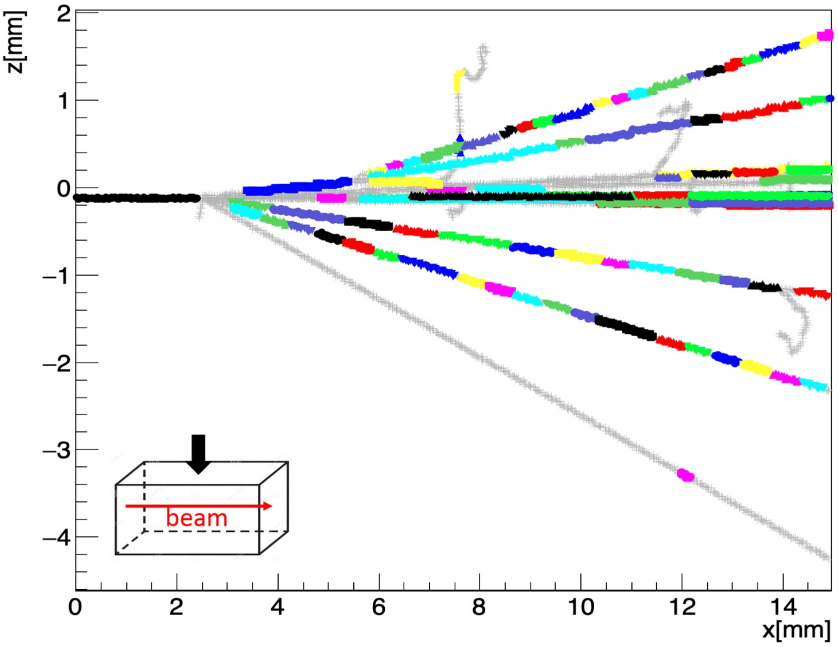

Figure 5.8: *The result of the first clustering attempt considering only the number of neighbors. The reconstructed clusters are shown in different colors, the noise points are shown in gray.*

up to $O(n \cdot \log(n) + n)$.

2. **Neighbours search:** After the sorting of the hit pixels, the search of neighbours is performed. If a pixel has a minimum number of neighbours (n_{neigh}) it is added to a cluster. The main difference with the DBSCAN algorithm consists in the application of an upper limit on hit pixels n_{neigh}. This condition is needed to split tracks in regions with high density of hits (e.g. vertices). For this reason, the condition to add a hit pixel into a clusters is to have $1 < n_{neigh} < 3$, otherwise it is considered as a *noise* point.
   With this condition, tracks belonging to the same vertex are split. On the other hand, a cut in the upper limit on $\mathrm{n_{neigh}}$ splits the tracks into small clusters. The result of the first clustering attempt is shown in Figure 5.8. The coloured points represent the reconstructed clusters while grey points are noise.

3. **Track fitting and merge:** At this point a linear fit of the reconstructed clusters is performed as described in the section 5.2.1.
   The parameters vector obtained from the fit is used to check the compatibility between two clusters which have both χ^2/ndf smaller than 2.5. If clusters have compatible direction cosine, close boundary points (distance smaller than 70 μm) and the track resulting from the merge has a χ^2/ndf smaller than 2.5,

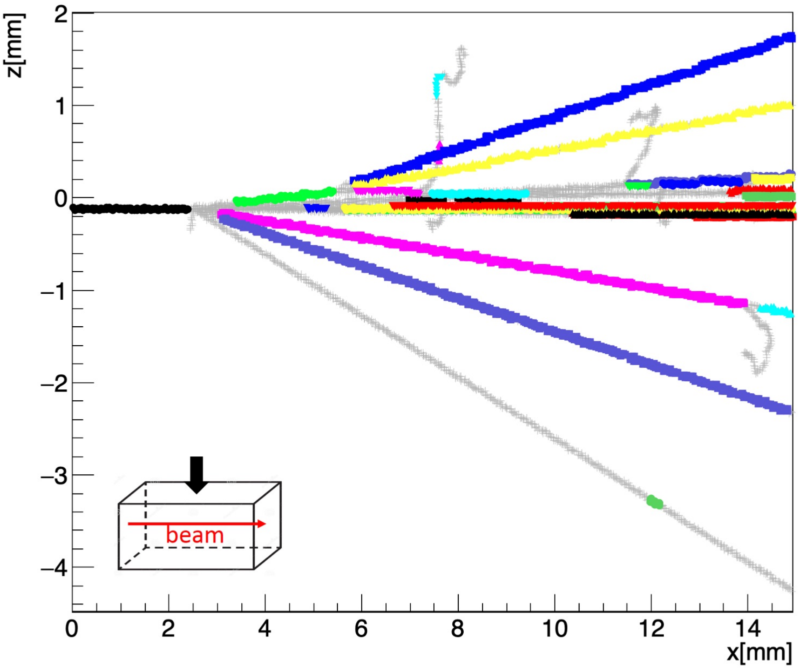

Figure 5.9: *Result of the first track merge attempt. The reconstructed clusters are shown in different colors, the noise points are shown in gray.*

they are merged together. The result of this merge is shown in Figure 5.9. A significant number of the small clusters has been merged into longer tracks.

4. **Further clusterization pass:** Figure 5.8 shows that after the first clusterization attempt, many noise points are still present in the event (grey points). For this reason, further clusterizations on residual noise points with less stringent conditions on the upper limit of n_{neigh} are performed. The clusterization on residual noise points is performed twice with $n_{neigh} < 4$ and $n_{neigh} < 6$. Is shown in Figure 5.10, after the clusterization attempts for noise points, a large number of noise points have been added to clusters. Residual noise points are then added to the reconstructed tracks if the distance between the point and the fit line is smaller than 40 μm.
Finally, a new fit and merge attempts are performed until the number of reconstructed tracks remains constant. Figure 5.11 shows that most of the hadronic, very straight tracks are well reconstructed. Non-rectilinear tracks are still broken but they are produced mostly by low energy δ electrons and therefore are not interesting for our purposes. At very forward rapidity some tracks remain split. The reason is that in this regions the hit density is very high and therefore tracks are very hard to resolve.

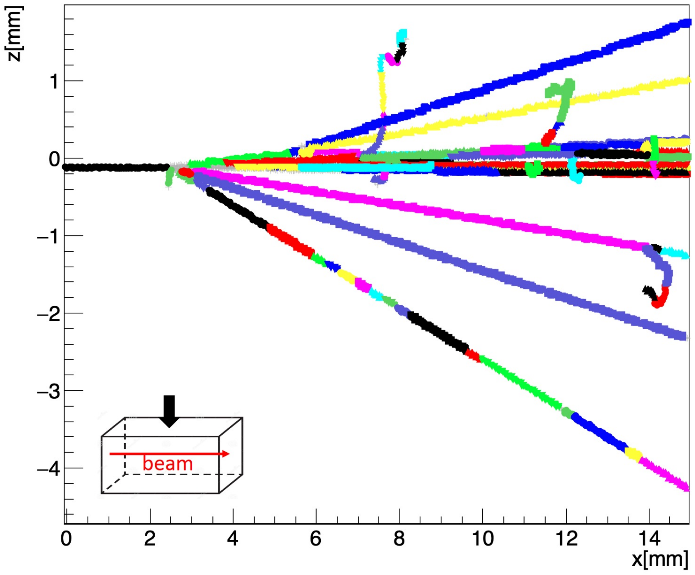

Figure 5.10: *Result of two clusterizations on noise points. The reconstructed clusters are shown in different, the noise points are shown in gray.*

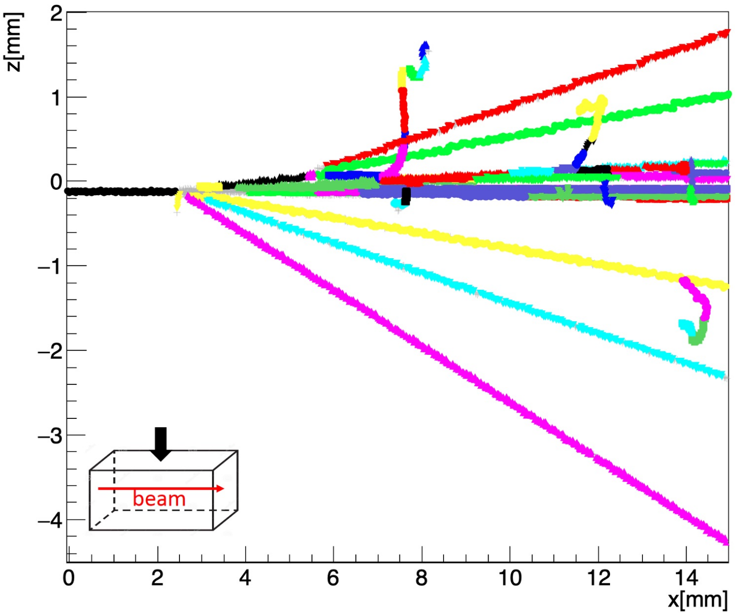

Figure 5.11: *Result of the final track merge. The reconstructed clusters are shown in different colors, the noise points are shown in gray.*

5.2.1 Track fit

Tracks are fit using a linear model of a parametric line:

$$\begin{cases} x = x_0 + v_x t \\ y = y_0 + v_y t \\ z = z_0 + v_z t \end{cases} \tag{5.1}$$

where

$$\begin{pmatrix} v_x \\ v_y \\ v_z \end{pmatrix} \tag{5.2}$$

it is the vector of direction cosines.

The fit is performed considering the projections of the straight line in equation 5.1 on the x-y and x-z planes and expressing y and z as functions of x:

$$\begin{cases} y(x) = y_0 + \frac{v_y}{v_x}(x - x_0) \\ z(x) = z_0 + \frac{v_z}{v_x}(x - x_0) \end{cases} \rightarrow \begin{cases} y(x) = y_0 + \alpha(x - x_0) \\ z(x) = z_0 + \beta(x - x_0) \end{cases} \tag{5.3}$$

Where x_0 is arbitrarily set as the first x coordinate of the fitted cluster.

In the fit, coordinate errors are taken the expected standard deviation for a position measurement with a digital pixel of given pitch:

$$\begin{array}{rclcl} \sigma_x & = & 29.24/\sqrt{12}\ \mu m & \sim & 8.4\ \mu m \\ \sigma_y & = & 50/\sqrt{12}\ \mu m & \sim & 14.4\ \mu m \\ \sigma_z & = & 26.88/\sqrt{12}\ \mu m & \sim & 7.8\ \mu m \end{array} \tag{5.4}$$

The points have errors along the three axes and the fit is performed on x-y and x-z planes. For this reason the function χ^2 to be minimized has to take into account the errors on all the coordinates:

$$\chi^2 = \sum_{i=1}^{n_{points}} \frac{(y_i - y(x_i))^2}{\sigma_y^2 + \alpha^2\sigma_x^2} + \frac{(z_i - z(x_i))^2}{\sigma_z^2 + \beta^2\sigma_x^2} \tag{5.5}$$

If the track is perpendicular to the x axis ($\mathrm{v_x} = 0$), the fit is performed on a single plane minimizing the function in equation 5.6.

$$\chi^2 = \sum_{i=1}^{n_{points}} \frac{(z_i - z(y_i))^2}{\sigma_z^2 + \beta^2\sigma_y^2} \tag{5.6}$$

Minimization is performed with MINUIT[43], a numerical minimization software library largely used for statistical analysis. It is conceived to find the minimum value of multi-parameter functions using the χ^2 or maximum likelihood method in order to

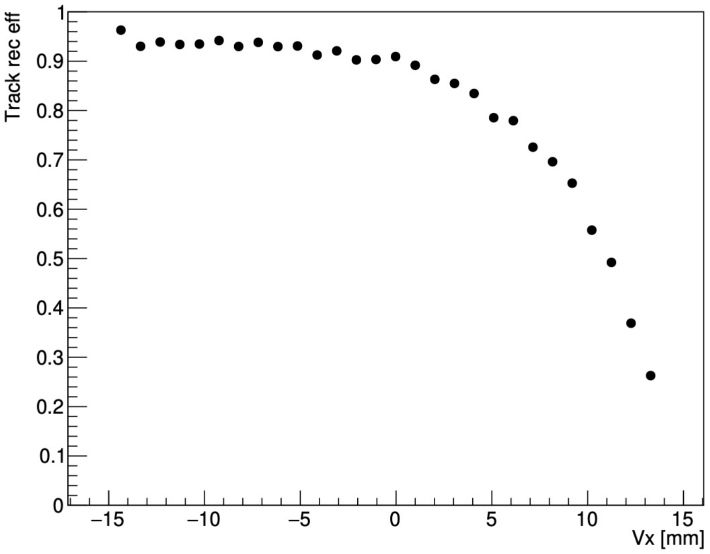

Figure 5.12: *Efficiency of tracks reconstruction.*

optimise the parameters of a data fit, their uncertainties and possibly the correlation between the parameters themselves.

The vector of parameters obtained from the fit is:

$$q_i = \begin{pmatrix} \alpha \\ y_0 \\ \beta \\ z_0 \end{pmatrix} \tag{5.7}$$

where, $\alpha = \mathrm{v_y}/\mathrm{v_x}$, $\beta = \mathrm{v_z}/\mathrm{v_x}$ and $\mathrm{y_0}$, $\mathrm{z_0}$ are the coordinates of a reference point along the line.

The fit of a track with N points has 2N-4 degrees of freedom.

5.3 Efficiency of track reconstruction

The efficiency of the track reconstruction is obtained as the ratio between the number of MC and reconstructed tracks considering only MC hadronic tracks with more than 50 points and a χ^2/ndf smaller than 1.5.

A reconstructed track is considered compatible with a MC one if they have compatible direction cosines and if the boundary points are closer than 70 µm.

Figure 5.12 shows the efficiency of the track reconstruction as a function of the position of the MC primary vertex. The efficiency decreases as the primary vertex approaches the end of the detector. The reason is that if the interaction occurs close to the end of the detector, the hadronic tracks produced in the interaction are very short and harder to be resolved and reconstructed. Excluding events in which the interaction occurs in the last 10 mm of the detector, the efficiency of the track reconstruction reaches $\sim 90\%$.

5.4 Primary vertex reconstruction

The reconstruction of primary vertex has been performed using two different methods which will be described in the following.

5.4.1 Fit of the primary vertex: least square method

The first method used to reconstruct the p-Si interaction point is based on the idea that the primary vertex is the intersection point of the tracks produced in the vertex. For the vertex fit, only tracks with more than 50 points, a χ^2 *textndf* < 2.5 and starting point close to the last proton track point (distance < 1 mm) are considered. The last condition can be applied because the last point of the proton track is always placed before the interaction point thanks to the neighbours upper limit condition of the reconstruction that splits tracks belonging to the same vertex.

From the linear track fit, the following measured parameters for the i-th track are taken:

- coordinates at a reference point $(\mathrm{x_{0i}}, \mathrm{y_{0i}}, \mathrm{z_{0i}})$;
- direction cosines $(\mathrm{v_{xi}}, \mathrm{v_{yi}}, \mathrm{v_{zi}})$.

The aim of the algorithm is to verify if the tracks have a common point (vertex, Figure 5.13). In order to do this, a fit based on the least squares method (LSM) is performed in which the inputs are the measured track parameters with their errors for each track. The output parameters of the fit are the vertex coordinates and new direction cosines:

- vertex coordinates $(\mathrm{x_v}, \mathrm{y_v}, \mathrm{z_v})$;
- updated direction cosines from the fit $(\widetilde{\mathrm{v}}_{\mathrm{xi}}, \widetilde{\mathrm{v}}_{\mathrm{yi}}, \widetilde{\mathrm{v}}_{\mathrm{zi}})$

In the LSM fit, the measured track parameter vector $\mathrm{q_i}$ (equation 5.7) of the i-th track are compared to a track parameter vector $\mathrm{h_i}$ based on the vertex-fit track model in equation 5.8:

$$\begin{cases} \widetilde{x}_i = x_v + \widetilde{v}_{xi} t \\ \widetilde{y}_i = y_v + \widetilde{v}_{yi} t \\ \widetilde{z}_i = z_v + \widetilde{v}_{zi} t \end{cases} \tag{5.8}$$

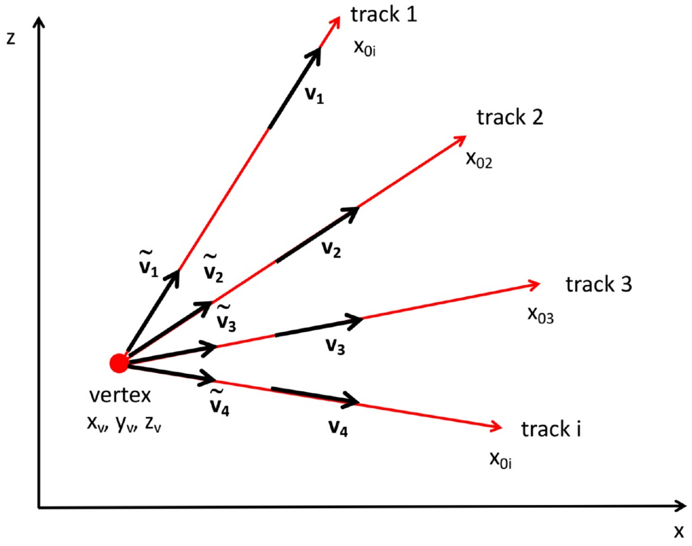

Figure 5.13: *Scheme of the fit of the tracks performed to find the point where they intersect, that is the primary vertex.*

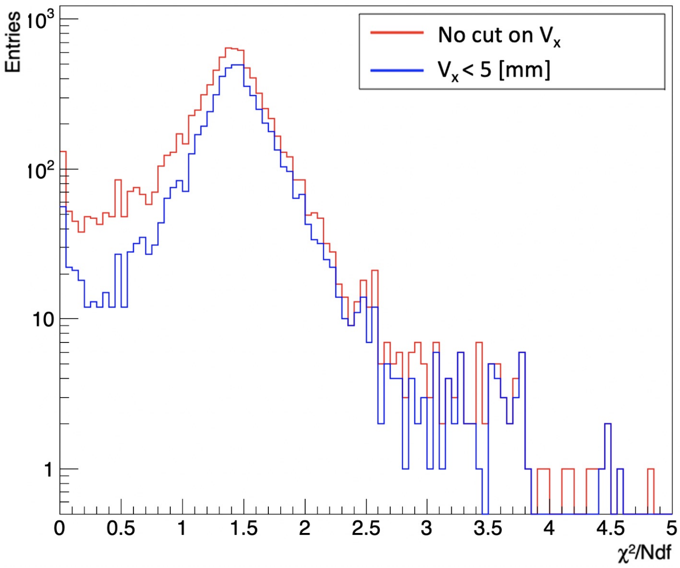

Figure 5.14: χ^2_{PV}/ndf *distributions without cut on the primary vertex position (red) and with a cut to exclude vertices that occur in the last 10 mm of the detector (blue).*

In this track model all the tracks have manifestly a common point (Figure 5.13), the vertex, for t = 0. Based on that, we consider the track parameter vector with $\widetilde{\mathrm{y}}$ and $\widetilde{\mathrm{z}}$ calculated as a function of $\widetilde{\mathrm{x}}$ (equation 5.9):

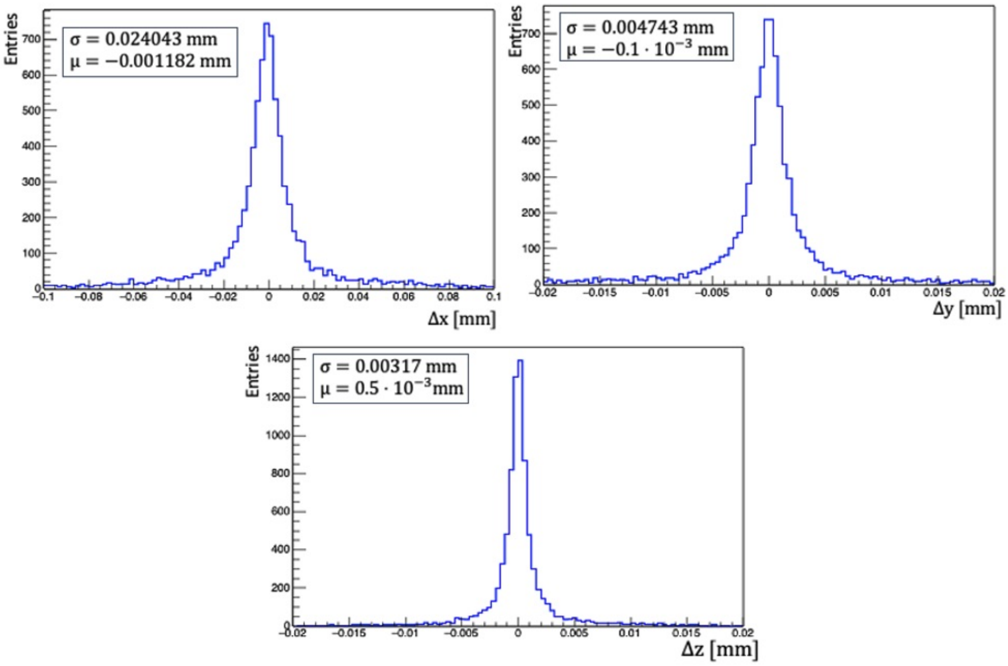

Figure 5.15: *Residuals obtained from the difference between the x, y and z coordinates of the reconstructed vertices and the Monte Carlo vertices.*

$$h_i = \begin{pmatrix} \widetilde{\alpha}_i \\ \widetilde{y}_i(x) = y_v - \widetilde{\alpha}_i(x_v - x_{0i}) \\ \widetilde{\beta}_i \\ \widetilde{z}_i(x) = z_v - \widetilde{\beta}_i(x_v - x_{0i}) \end{pmatrix} \tag{5.9}$$

The χ^2 to be minimized is

$$\chi^2_{PV} = \sum_{i=2}^{n_{tracks}} (q_i - h_i)^T V_i^{-1} (q_i - h_i) \tag{5.10}$$

Where V_i is the matrix containing the diagonal elements of the track fit covariance matrix.

For the primary vertex, the proton track is mandatory and it is identified as the one starting at the very beginning of the detector. A second linear track is added to the fit and the vertex fit is performed. If the vertex fit has a reduced $\chi^2_{PV} < 2.5$, the track is kept; otherwise it is rejected. A new track is then added and the fit is performed again. The procedure continues until all tracks have been tested.

A vertex fit with N tracks has 2N-3 degrees of freedom.

After the track reconstruction, some tracks are still split in small clusters as seen in 5.2. If the proton track is split, a vertex can be found between the clusters of the

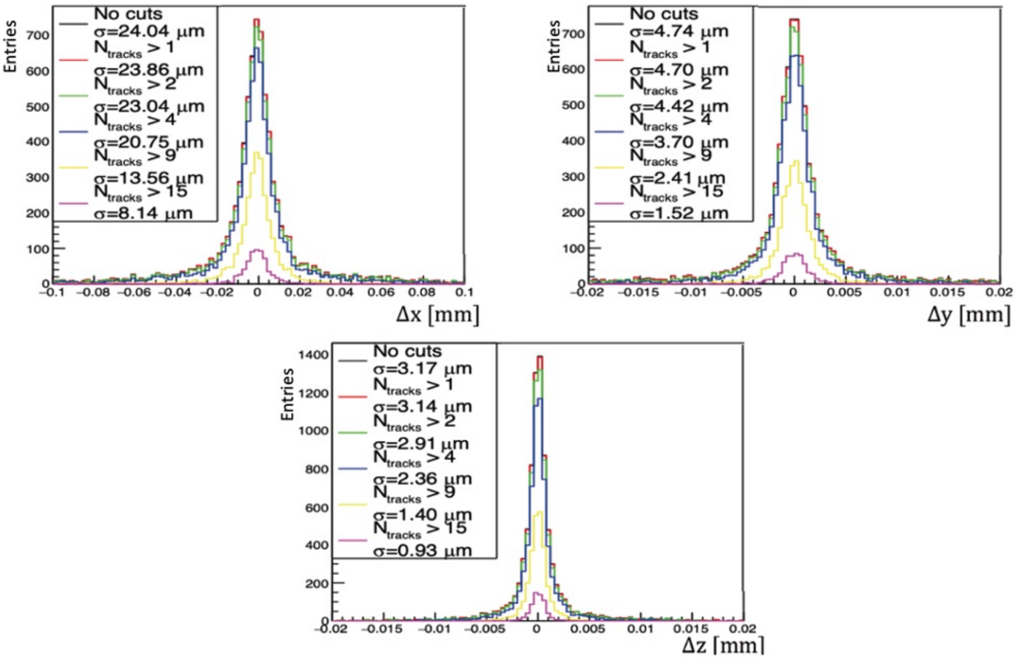

Figure 5.16: *Distributions of the residuals of the reconstructed vertices with different cuts on the number of tracks associated with the vertex.*

proton track. To avoid this issue, if the track multiplicity (N_{tr}) of the reconstructed vertex is 2, a merge attempt is performed between the two tracks. If the resulting track has a reduced $\chi^2 < 1.5$ the proton track identification is updated and the vertex reconstruction starts from the beginning.

The distributions of the χ^2_{PV}/ndf obtained from the fit are shown in Figure 5.14. The red distribution in Figure 5.14 shows the χ^2_{PV}/ndf obtained considering the all the reconstructed vertices. The distribution shows a peak for $\chi^2_{PV}/\mathrm{ndf} = 0$.

This is due to the fact that there are vertices to which only the the proton track is associated or when the vertex track multiplicity is 2. Both conditions occur when the proton interacts at the end of the detector and therefore produced hadronic tracks are very short and hard to resolve and do not fit the conditions to be included in the fit, as discussed in section 5.3.

Applying a fiducial cut to exclude the last 10 mm of the detector and excluding events with $N_{tr} < 2$, the χ^2_{PV}/ndf distribution (shown in blue in Figure 5.14) shows that the peak at 0 is reduced and the mean value is 1.35.

The vertex reconstruction efficiency is calculated taking in account reconstructed vertices with $\chi^2_{PV} < 2.5$ and $N_{tr} > 2$ and the fiducial cut on the MC primary vertex position along the beam axis to exclude interactions occurred in the last 10 mm of the detector. The efficiency is $\sim 78\%$.

Figure 5.15 shows the residual distributions obtained as the difference between

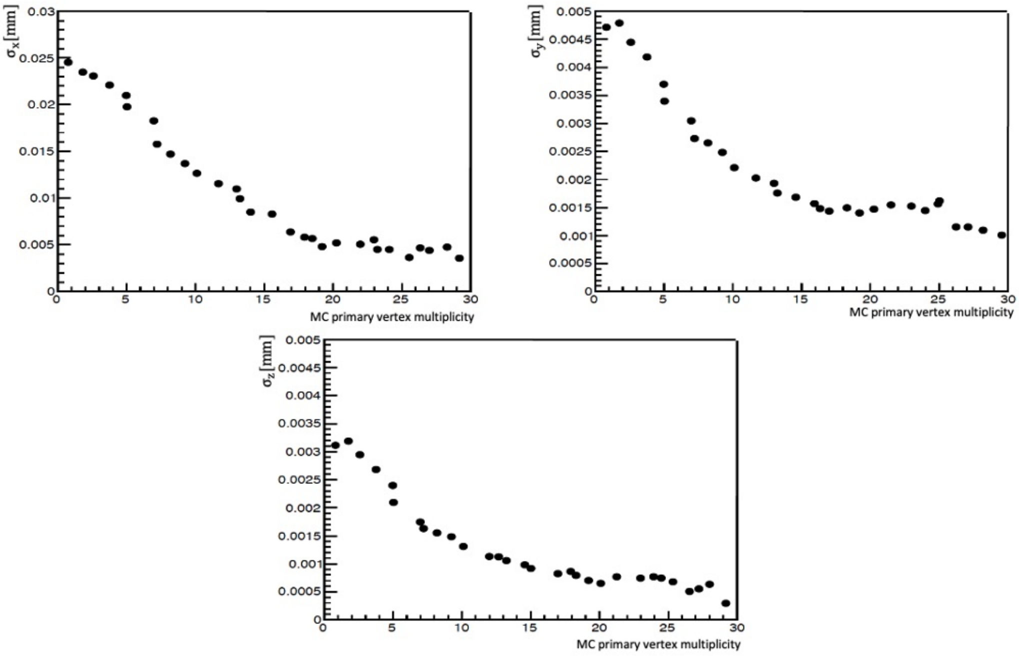

Figure 5.17: *Resolutions on the x, y and z coordinates of the vertices reconstructed as a function of the number of tracks associated with the vertices.*

the x, y and z coordinates of the reconstructed primary vertices and the MC ones. The resolutions on the primary vertex position are obtained as the standard deviations of the residual distributions. They are ∼ 24 µm along the beam axis, ∼ 4.7 µm and ∼ 3.2 µm along the transverse axes.

The residuals for different cuts on track multiplicity are shown in Figure 5.16. Figure 5.17 shows the trends of the resolutions obtained from the residuals as a function of the primary vertex multiplicity. The resolutions improve as the multiplicity increase, as expected, arriving at ∼ 5 µm along the beam axis and ∼ 0.5 µm along the z axis for $N_{tr} > 30$.

5.4.2 Fit of the primary vertex: weighted least square method

The vertexing method described in 5.4.1 section has some limitations. First, the off-diagonal elements of the covariance matrix used in the function χ^2 (equation 5.10) are neglected. Secondly, the coordinates of the reconstructed vertex can be shifted due to the association of secondary vertex tracks.

For this reason, another more rigorous algorithm for vertex reconstruction has been implemented. This is based on a method used in other experiments such as LHCb [44], ALICE and earlier, CERES and NA45 [45] and is a weighted least square method (WLSM).

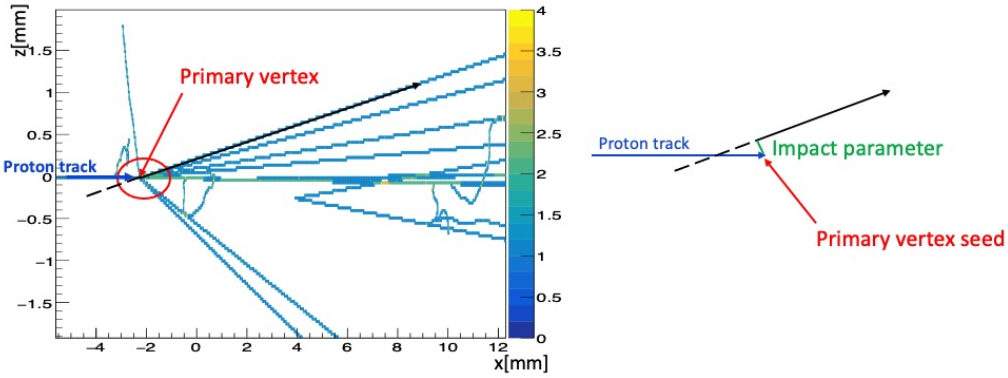

Figure 5.18: *Primary vertex impact parameter scheme.*

In this case, the aim is to determine x_v, y_v and z_v while tracks are not refitted. The vector of the y_v and z_v coordinates is:

$$h_i = \begin{pmatrix} y_v \\ z_v \end{pmatrix} \tag{5.11}$$

Initial values of x_v, y_v and z_v (seed) are set as the last point of the proton track which is identified as the one starting at the entrance of the detector. These coordinates are reasonably close to the interaction point.

For each reconstructed track with more than 50 points and $\chi^2/\mathrm{ndf} < 2.5$ the vector of y and z coordinates corresponding to x_v is calculated based on the fit parameters

$$h_i = \begin{pmatrix} y_{0i} - (x_v - x_{0i})\alpha \\ z_{0i} - (x_v - x_{0i})\beta \end{pmatrix} \tag{5.12}$$

Using the fit vector q_i (equation 5.7) and h_i for each track, the distance from the primary vertex at its point of closest approach called impact parameter (Figure 5.18) χ^2_{IP} is evaluated:

$$\chi^2_{IPi} = (q_i - h_i)^T V_i^{-1} (q_i - h_i) \tag{5.13}$$

Where V_i is the covariance matrix obtained from the track fit:

$$V = \begin{pmatrix} (\Delta x)^2\sigma_\alpha + 2\Delta x\sigma_{\alpha y} & (\Delta x)^2\sigma_{\alpha\beta} + \Delta x\sigma_{\alpha z} + \Delta x\sigma_{\beta y} + \sigma_{yz} \\ (\Delta x)^2\sigma_{\alpha\beta} + \Delta x\sigma_{\alpha z} + \Delta x\sigma_{\beta y} + \sigma_{yz} & (\Delta x)^2\sigma_\beta + 2\Delta x\sigma_{\beta z} + \sigma_z \end{pmatrix} \tag{5.14}$$

A weight W_T is assigned to each track on the basis of the χ^2_{IP}. It depends on the ratio between the χ^2_{IP} and the Tukey [46] constants C_T:

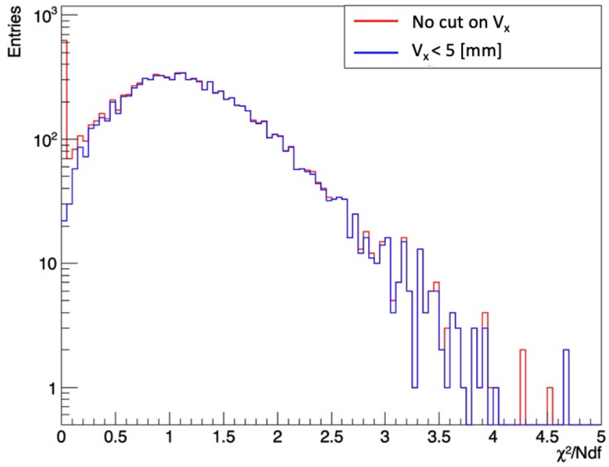

Figure 5.19: χ^2_{PV}/ndf *distributions without cut on the primary vertex position (red) and with a cut to exclude vertices that occur in the last 10 mm of the detector (blue).*

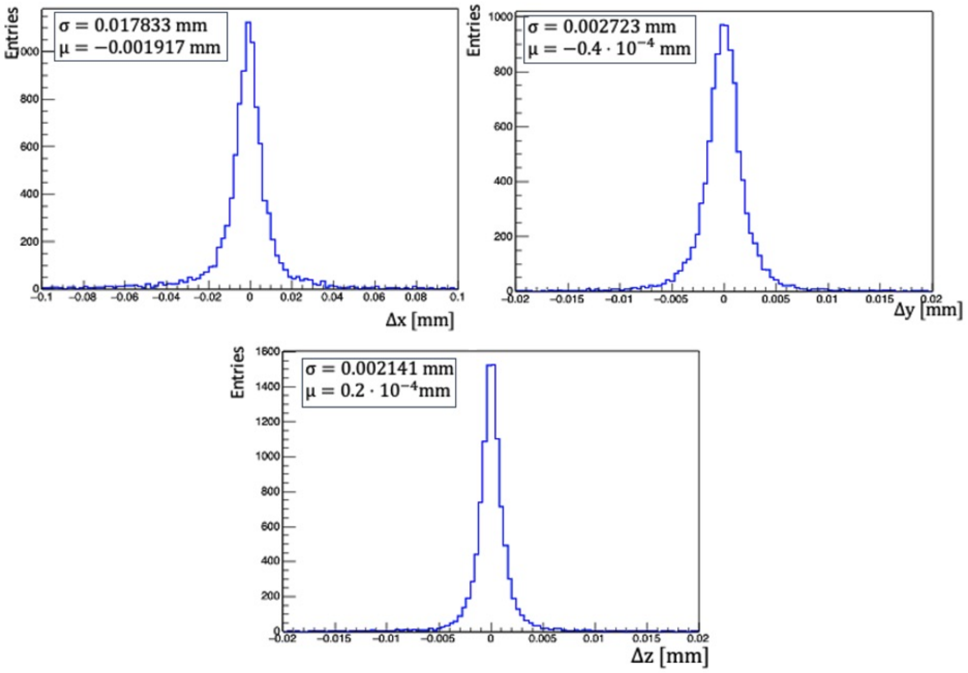

Figure 5.20: *Distributions of residuals calculated as the difference between the x, y and z MC and reconstructed vertex coordinates.*

$$W_{Ti} = \left(1 - \frac{\chi^2_{IPi}}{C_T^2}\right) \quad \text{if } \chi^2_{IPi} < C_T \tag{5.15}$$

$$W_{Ti} = 0 \quad \text{if } \chi^2_{IPi} > C_T \tag{5.16}$$

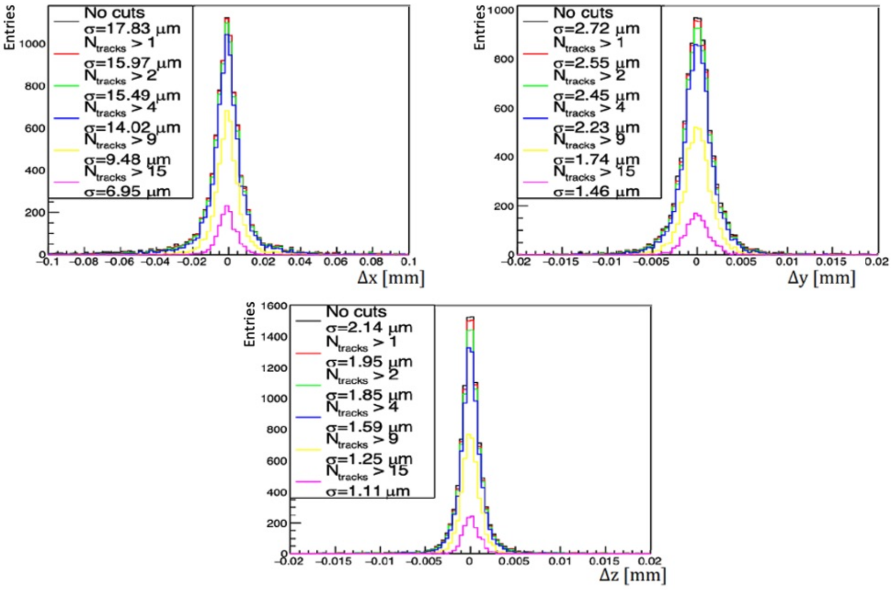

Figure 5.21: *Distribution of the residuals of the reconstructed vertices with different cuts on N_{tr}.*

This allows to avoid associating to the primary vertex tracks which could worsen the vertex estimation.

The primary vertex χ^2_{PV} is obtained summing each track χ^2_{IP} weighted by $\mathrm{W_T}$ and is then minimized using MINUIT [43] to obtain the primary vertex coordinates.

$$\chi^2_{PV} = \sum_{i=1}^{n_{tracks}} \chi^2_{IPi} W_{Ti} \tag{5.17}$$

The procedure is iterative and the χ^2_{PV} is calculated at each iteration for decreasing values of $\mathrm{C_T}$. The initial value of $\mathrm{C_T}$ is set to 10^6 to avoid convergence in local minimum and decreases to the empirically determined value of 20.

At each iteration, the vector $\mathrm{h_i}$ is updated and the values of χ^2_{IP} and $\mathrm{W_T}$ are recalculated. In this way, the tracks that in a specific iteration had a weight equal to zero are retested and if their weight is different from zero they contribute to the fit. The iteration is stopped when χ^2_{PV} has converged to a stable value.

Figure 5.19 shows the distribution of the χ^2_{PV}. There is a peak at zero due to primary vertices occurring in the last 10 mm of the detector. In these events, only the proton track is associated to the primary vertex and $\mathrm{N_{tr}} < 2$ as discussed in section 5.3. The vertex reconstruction efficiency is calculated by taking into account the reconstructed vertices with $\chi^2_{\mathrm{PV}} < 2.5$ and $\mathrm{N_{tr}} > 2$ and the fiducial cut on the MC primary vertex position along the beam axis to exclude interactions occurred in the last 10 mm of the detector. The efficiency is $\sim 97\%$.

Figure 5.20 shows the distributions of the residuals obtained as the differences

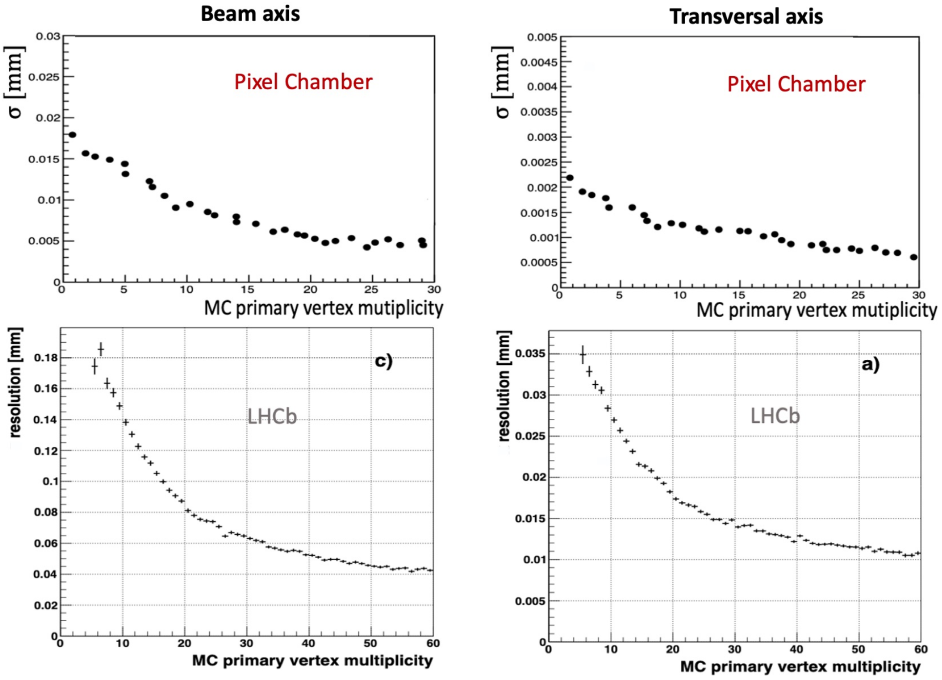

Figure 5.22: *Comparison between Pixel Chamber (top) and LHCb (bottom) resolution distributions on the x, y and z coordinates of the reconstructed vertices as a function of MC vertex multiplicity.*

between the x, y and z MC and reconstructed vertex coordinates. The resolutions, obtained as the standard deviations of the distributions, range from ∼ 18 µm along the beam axis (x, top left) to ∼ 2 µm (z, bottom right).

Figure 5.21 shows that resolutions improve by increasing the primary vertex track multiplicity. This behaviour is also shown in Figure 5.22. With $N_{tr} > 25$ the primary vertex resolution reaches 5 µm along the beam axis and 0.5 µm along the transversal axes.

Figure 5.22 shows the comparison between Pixel Chamber and LHCb primary vertex resolutions as a function of N_{tr}. Although the two experiments are conducted under different conditions (multiplicity, energy, etc.), it is nevertheless interesting to observe that with Pixel Chamber it is possible to obtain resolutions that are about one order of magnitude better than those obtained with LHCb [44].

5.4.3 Fit of the primary vertex: comparison between the two methods

Figure 5.23 shows the comparison between the distributions of residuals obtained using the LSM (section 5.4.1) and the WLSM (section 5.4.2) vertex reconstruction methods.

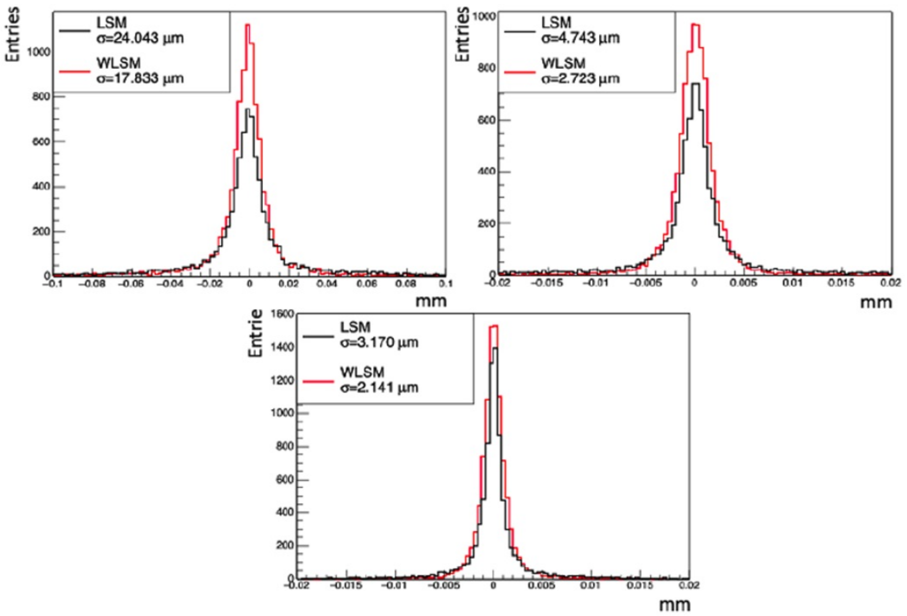

Figure 5.23: *Comparison of distributions of residuals obtained using the LSM and WLSM vertex fit methods.*

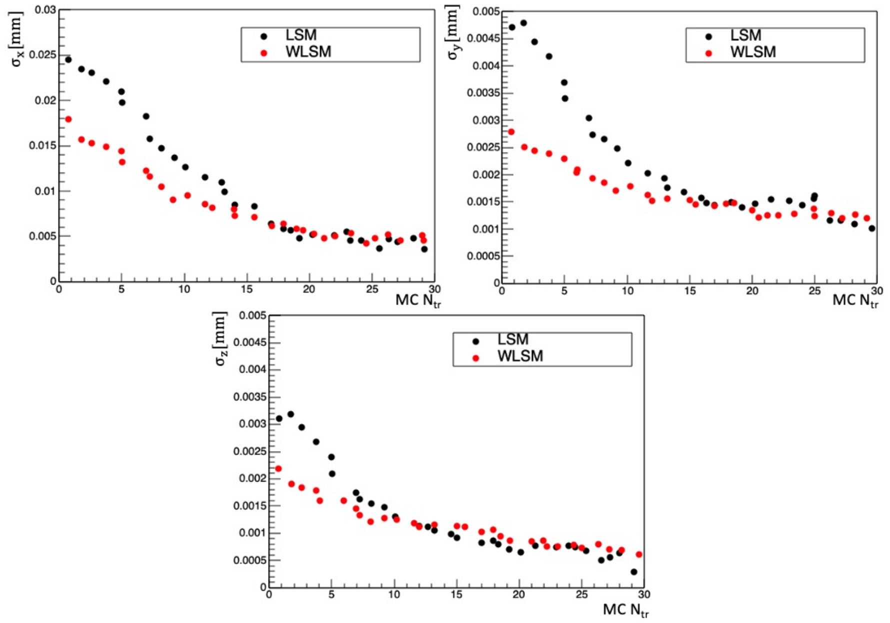

Figure 5.24: *Comparison of residual trends as a function of the number of tracks associated with the primary vertex obtained using the LSM and WLSM vertex fit methods.*

With the second method the reconstruction efficiency is higher and resolutions are better. This is also seen in Figure 5.24 that shows the resolutions as a function of the primary vertex multiplicity. Figure 5.24 shows that only for rather high multiplicity ($\sim N_{tr} > 15$) resolutions are comparable.

Table 5.1 a summarize the results obtained with the two vertex finding methods.

	LSM method	WLSM method
Vertex reconstruction efficiency ($\mathrm{V_x} < 5$[mm])	78%	97%
mean χ^2_{PV}/ndf $\mathrm{N_{tr}} > 2,\ \mathrm{V_x} < 5$[mm]	1.35	1.10
σ_{x} (μm) $\mathrm{N_{tr}} > 2,\ \mathrm{V_x} < 5$[mm]	23.50	15.20
σ_{y} (μm) $\mathrm{N_{tr}} > 2,\ \mathrm{V_x} < 5$[mm]	4.40	2.10
σ_{z} (μm) $\mathrm{N_{tr}} > 2,\ \mathrm{V_x} < 5$[mm]	3.17	1.80
σ_{x} (μm) $\mathrm{N_{tr}} > 25,\ \mathrm{V_x} < 5$[mm]	5.50	4.90
σ_{y} (μm) $\mathrm{N_{tr}} > 25,\ \mathrm{V_x} < 5$[mm]	1.20	0.50
σ_{z} (μm) $\mathrm{N_{tr}} > 25,\ \mathrm{V_x} < 5$[mm]	0.70	0.50

Table 5.1: *Summary of the results obtained by the two vertex fit methods.*

5.5 D^{0}econdary vertex reconstruction

The D^0 is a meson containing a charm and anti up quark with rest mass 1864.84 MeV [47]. In each event a charm meson decay is present:

- $D^0 \rightarrow K^-\pi^+$ with a probability of 50%;
- $\bar{D}^0 \rightarrow K^+\pi^-$ with a probability of 50%.

The algorithm for the secondary vertex reconstruction is the weighted least square method described for the primary vertex but with some differences to adapt it to the reconstruction of the D^0 vertex. First the vertex fit is performed on pairs of tracks (with $\mathrm{n_{pts}} > 50$ and χ^2/ndf < 2.5) testing all combinations not associated to the primary vertex. Second, the initial vertex value (seed) is the closest point to the primary vertex of one of the two tracks under test.

The secondary vertex reconstruction is performed on all the events with a primary vertex χ^2_{PV}/ndf < 2.5, $\mathrm{N_{tr}} > 2$ and $\mathrm{V_x} < 5$ mm.

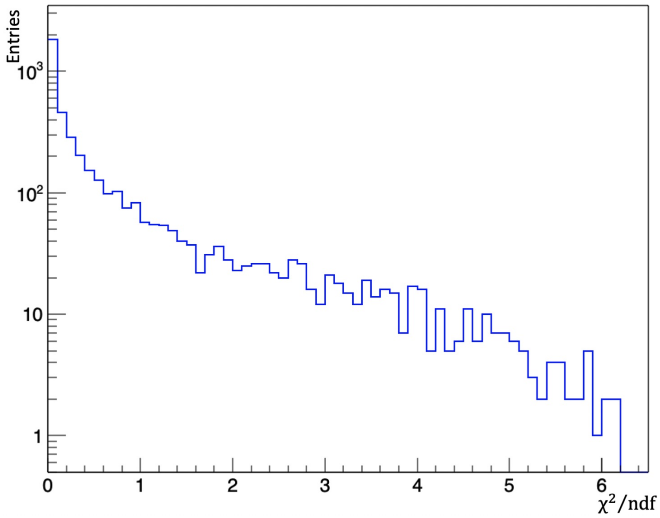

Figure 5.25: *χ^2/ndf distribution for the reconstructed secondary vertices.*

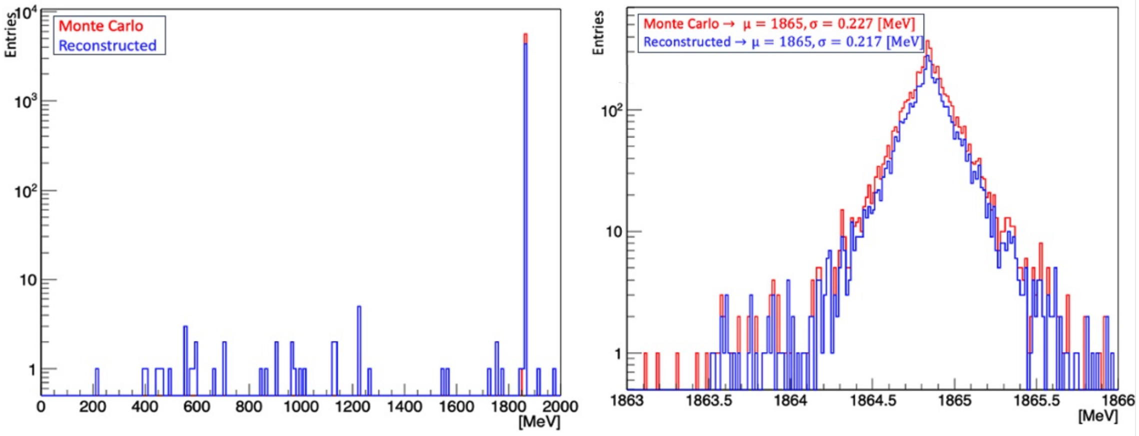

Figure 5.26: *Blue: invariant mass distribution of closest secondary vertices to the primary vertices; red: MC distributions of the D^0 invariant mass. Left: distribution including misidentified vertices; right: zoom of the distribution in the D^0 mass region.*

Many secondary vertices can be found in each event and the D^0 vertex candidate is selected as the closest to the reconstructed primary vertex. Figure 5.25 shows the χ^2/ndf distribution for the reconstructed secondary vertices.

Using the MC information of energy and momentum of the decay products it is possible to calculate the invariant mass of the particles belonging to a vertex and verify if the D^0 vertex has been correctly identified. Figure 5.26, left shows the MC (red) and reconstructed (blue) invariant mass distributions. The blue spike at 1864 MeV corresponds to the correctly reconstructed D^0 vertices. A small fraction $\sim 2\%$ are incorrectly reconstructed. Figure 5.26, right shows a zoom around the D^0 mass.

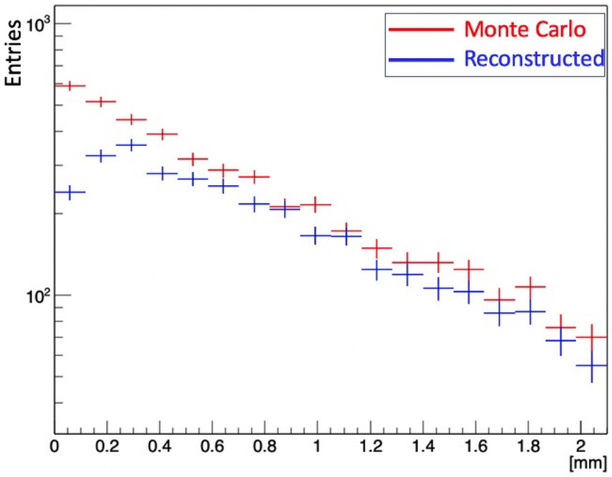

Figure 5.27: *Blue: decay length obtained as the difference between reconstructed primary and secondary vertices; red: decay length obtained as the difference between MC primary and secondary vertices.*

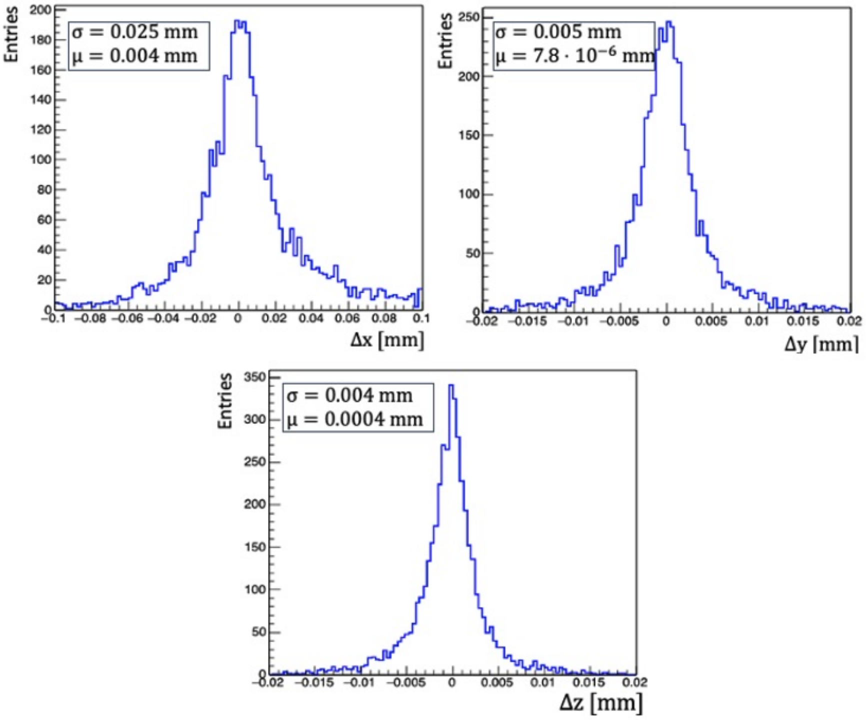

Figure 5.28: *Distributions of residuals for secondary vertices obtained as the difference between the MC and reconstructed vertex coordinates.*

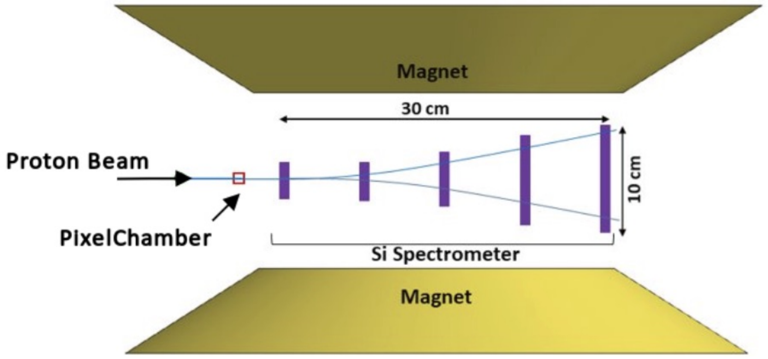

Figure 5.29: *Integration of Pixel Chamber with a silicon spectrometer.*

The secondary vertex reconstruction efficiency, calculated as the ratio between the number of reconstructed and MC vertices in the mass range between 1863 and 1866 MeV is $\sim 80\%$.

This 20% inefficiency might be due to cases in which the secondary vertex is very close to the interaction point and one or both tracks are incorrectly associated with the primary vertex. It can happen that one or both tracks are broken and do not fit the requirements to be used in the vertex fit.

Further insight is provided in Figure 5.27, which shows the decay length distribution obtained as the difference between primary and secondary reconstructed (blue) and MC (red) vertices. Indeed there is a non-negligible difference between the two distributions for lengths smaller than 0.15 mm indicating that this inefficiency might be due to the fact that tracks produced by D^0 decay near the interaction vertex may be mistakenly associated with the primary vertex.

The residual distributions, obtained as the difference between the MC and reconstructed vertex coordinates) are shown in Figure 5.28. The resolutions for the secondary vertex coordinates are 25 μm along the beam axis and 5 and 4 μm along the two transverse axes.

5.5.1 A silicon spectrometer for the measurement of momentum

The reconstruction of the invariant mass of charm and beauty particles can only be performed with information about the charged particles momentum. The measurement of momentum could be performed coupling Pixel Chamber with a silicon telescope immersed in a magnetic field.

A telescope of 5 planes of ALPIDE pixel sensors immersed in a dipole magnet field starting few cm downstream of Pixel Chamber is sketched in Figure 5.29. Each plane is based on the pixel sensor modules (staves) already developed for the ALICE

ITS Inner Barrel.

First simulations of the performances of the telescope are ongoing.

Chapter 6

Continuous tracking studies with test beams data

At present the R&D on the construction of the first A9 stack is under way and is not ready for tests yet. So, in order to test the track reconstruction algorithm, single ALPIDE sensors have been used, exposing the sensor to particle beams along the surface of the sensor. In this way particles can produce very long continuous tracks inside the sensor.

In this work we profited from experimental setups which have been prepared in the context of ALICE ITS3 ([48]) which will be installed during LHC long shutdown 3. This detector will use curved wafer-scale ultra-thin silicon sensors and will replace the innermost layers of the ITS2. As a part of the R&D for the ITS3, ALPIDE sensors are used in a bent configuration for preliminary studies in the laboratory and in test beam campaigns. As explained below, part of the beam just grazes the curved surface producing long tracks inside the sensor. Additionally, in another setup a planar sensor was exposed to a beam along the surface of the sensor.

Two test beams with electrons have been carried out at the Deutsches Elektronen-Synchrotron (DESY) in Hamburg in December 2020 and April 2021. The third test beam was carried out at CERN, at the Super Proton Synchrotron (SPS) with a beam composed partly of pions and protons and partly of electrons and muons in July 2021.

6.1 Test beam apparatus

6.1.1 ALPIDE readout system

A portable readout system for the ALPIDE readout was used in the test beams. The system was developed at INFN Cagliari in 2014 in collaboration with CERN [49] for ALPIDE characterization. The system was extensively used to characterize the earlier ALPIDE prototypes and eventually the final ALPIDE sensor in the laboratory

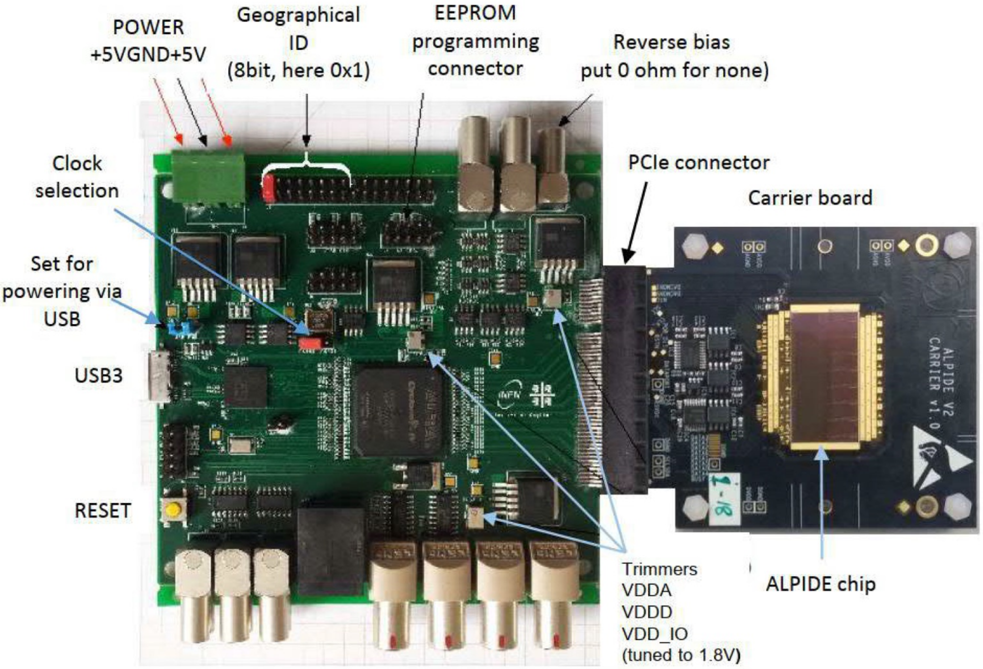

Figure 6.1: *ALPIDE readout board connected to a carrier board hosting the ALPIDE sensor.*

with radioactive sources and in test beam campaigns. It is still being used for tests related to the future developments in ALICE.

The readout system consists of an FPGA based readout board connected to the carrier board hosting ALPIDE via a Peripheral Component Interconnect Express (PCIe) connector and reads a single ALPIDE sensor (Figure 6.1). The system has a USB 3.0 interface for data transfer. The board can be powered through an external power supply or through the USB 3.0 interface.

The readout board contains an FPGA ALTERA Cyclone IV [50] which implements the readout logic. The USB 3.0 protocol is implemented using a Cypress FX3 chip [51]. The board contains DC-DC converters that generate different voltage levels. The state of the voltages and currents sent to the sensor are monitored by ADCs. In case the currents reaching the sensor exceed a certain threshold, an auto shut-off mode is activated to prevent possible damage to the sensor.

6.1.2 Silicon telescope and trigger system

A silicon telescope consisting of two arms was used, containing 2 or 3 reference planes with ALPIDE sensors. At the center, the Device Under Test (DUT) is placed. The DUT can be a planar or bent ALPIDE [52].

A trigger signal is used to readout the DUT. The trigger is formed by the coin-

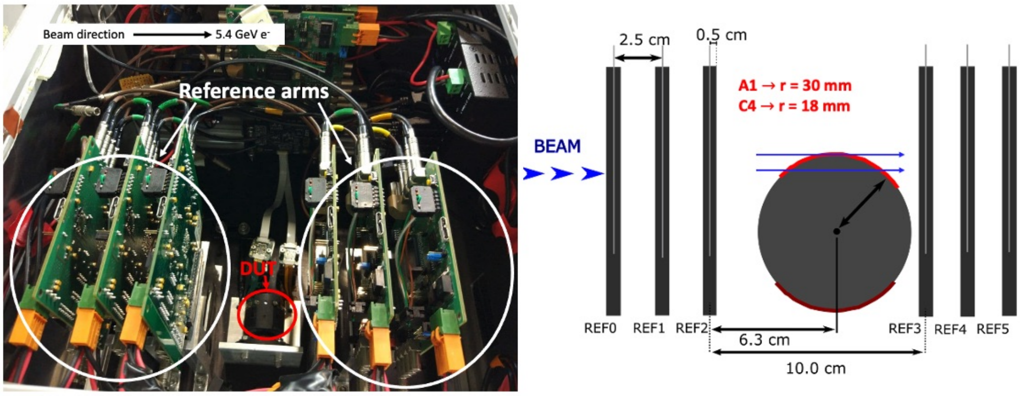

Figure 6.2: *Left: setup consisting of the telescope with 2 reference arms, each containing 3 ALPIDE with the housing for the DUT in the center.* Right: layout with a curved ALPIDE in "double crossing" configuration".

cidence of two scintillators placed on both sides of the telescope. The scintillators generate a busy signal of 20 µs which is used to prevent particles too close in time to generate a trigger signal. A trigger signal is only accepted in absence of busy signal.

In all test beams the data acquisition software was based on EUDAQ2 framework [53].

6.2 Bent ALPIDE sensor: DESY test beam in December 2020

At the December test beam at DESY, the setup consisted of a 2-arm, pixel-plane telescope (ALPIDE), each containing 3 planes (Figure 6.2). The DUT is a bent ALPIDE sensor.

The beam consists of 5.4 GeV electrons passing through the DUT in a the configuration shown in Figure 6.3. In this configuration, the beam can graze the surface producing a track in a roughly flat region of the sensor. These are the events of interest for this study.

We used two DUT chips during the data taking, one called A1 with a curvature radius of 30 mm and one called C4 with a curvature radius of 18 mm. Considering the curvature radius and the sensor thickness it is possible to define an approximately flat surface of the A1 (3.2 mm) chip is larger than that of the C4 (2.7 mm) (Figures 6.3, left and 6.4).

For both DUTs, a back bias voltage (V_{bb}) of -3 V was applied and a threshold of 50 e^- was chosen. The cluster size in this configuration is 2, which is typical for ALPIDE.

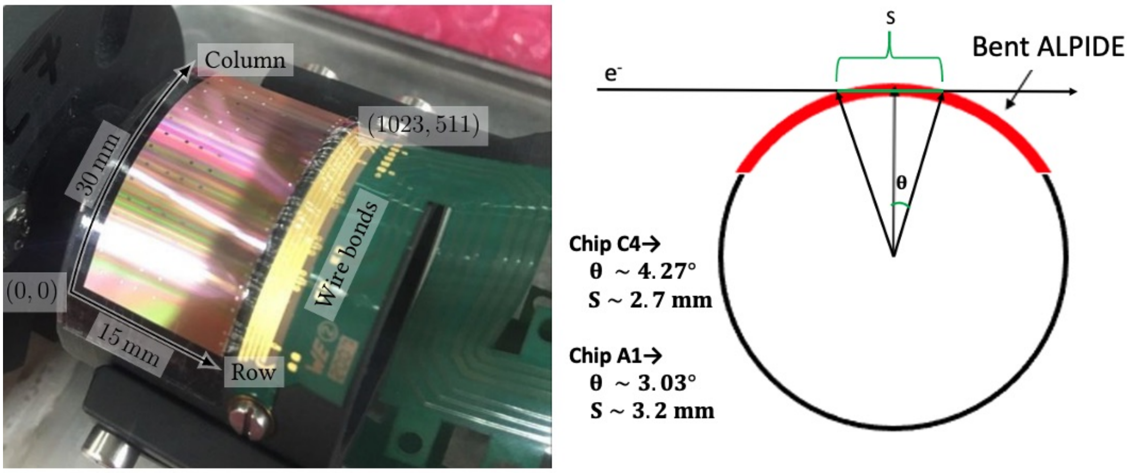

Figure 6.3: *Left: DUT at December test beam at DESY, bent ALPIDE. Right: Bent ALPIDE crossed by a particle.*

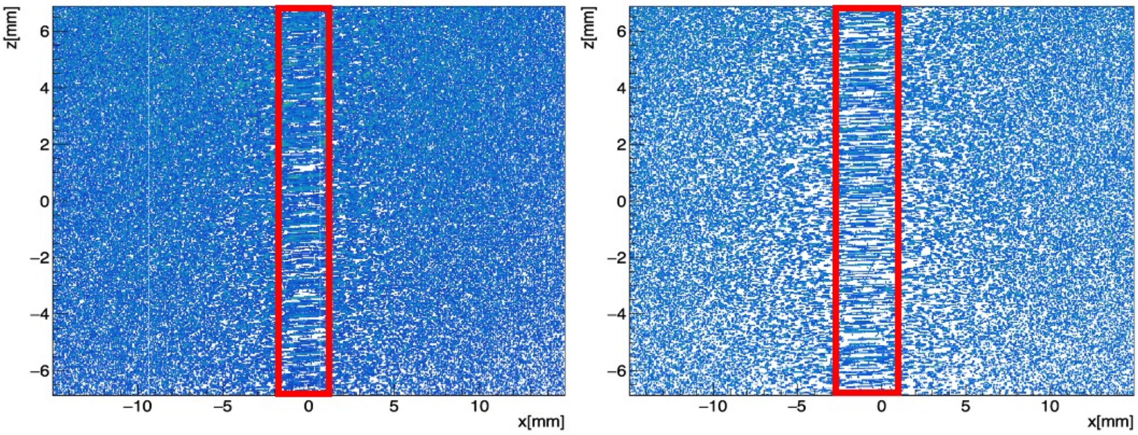

Figure 6.4: *Left: hit map of C4 DUT. Right: hit map of A1 DUT.*

Figure 6.4 shows the hit map for the two chips considered. At the center of the sensor, there is a chip portion where the tracks are long. This region is considered for data analysis.

Data analysis is divided in two main steps. First we used the Corryvreckan tool [54, 55] to get the roto-translation matrices for the alignment of the telescope planes (see section below). Second, we used the Pixel Chamber track reconstruction algorithm to reconstruct the tracks produced on the DUT surface and in the reference planes. Finally we tried to correlate the tracks reconstructed in the telescope and in the DUT.

A data selection has been performed to select the events in which the beam electrons cross the DUT surface and produce a track long enough to be accurately

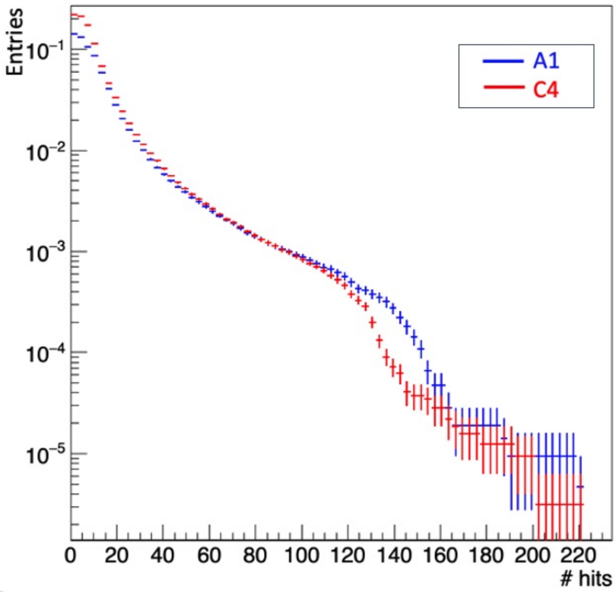

Figure 6.5: *Fraction of events with hits in the DUT.*

reconstructed. Figure 6.5 shows the distribution of the fraction of events containing hits in the DUT. As expected, the A1 chip featured more events where long, straight tracks have been produced. In the A1 chip, in the 8% of events more than 110 hits have been produced while in the C4 chip the same number of hits is produced in the 6% of events. Considering the portion of approximately flat surface that has to be crossed by a particle in order to produce a long and continuous track, the data analysis was performed only on the events in which at least seventy-five hits have been produced in the DUT.

6.2.1 Corryvreckan tool for planes alignment

Corryvreckan [54, 55] is a software specifically developed for off-line reconstruction and analysis of test beam and laboratory data. The Corryvreckan analysis and reconstruction framework are written in C++ with a modular design which allows functionalities such as coordinate transformation, analysis configuration, input and output to be personalized by the user in a simple and fast way. In the main event loop of the analysis, the data is processed sequentially in each sensor.

Corryvreckan deals with three main modules. Global modules operate on data on all available detectors, detector modules operate on a single detector of the setup and finally DUT modules. This separation allow the analysis and reconstruction to be personalized by the user in an easy way. For example, Corryvreckan has been used to perform track reconstruction using all the reference planes and excluding the DUT modules.

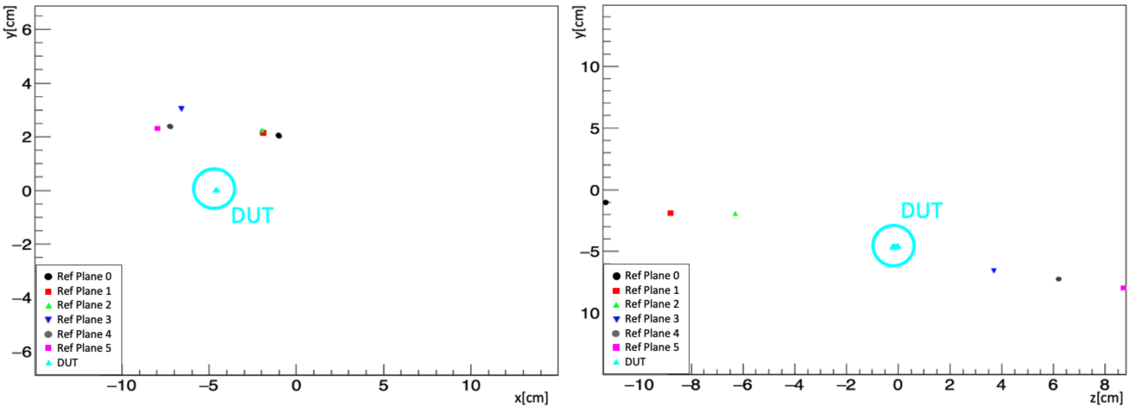

Figure 6.6: *Reference planes hits before the alignment.*

An event contains pixels information, time frame within which all data are located and all information available. The event preparation is performed processing raw data with a set of detector specific EventLoader modules. In our analysis we used EUDAQ2 [53] framework.

The detectors properties, including position, number of pixels, spatial and time resolution, are described in the geometry configuration files. Corryvreckan will only process data contained in this files. For each detector the role parameter defines if the sensor behaves as a DUT or reference plane. Reference planes are used to perform the alignment of the system.

The local coordinate system for a detector plane is defined as a right-handed Cartesian system centred in the centre of the sensor and where x and y axes describe the plane on which the sensor lies. The global coordinate system for the entire setup is defined as a right-handed Cartesian system where the z axis is along the beam axis. The orientation of a sensor in the global coordinate system is described by rotations around the geometrical centre of the sensor.

We used Corryvreckan to obtain the roto-translation matrices for the reference sensors alignment (Figure 6.6), a preliminary operation needed to perform the track reconstruction using the Pixel Chamber algorithm. The DUT is ignored during the telescope alignment.

The AlignmentTrackChi2 module has been used to perform the telescope alignment. This module requires a dedicated prealignment otherwise the alignment will fail. The z position of the telescope planes has to be measured in the experimental setup and set in the configuration files.

The prealignment module performs a preliminary translational alignment around x and y axes of the telescope planes. The distribution describing the correlation between hits in different planes has a Gaussian form. Prealignment is performed by minimizing this correlation so that the mean value of the Gaussian fit function is centred at 0.

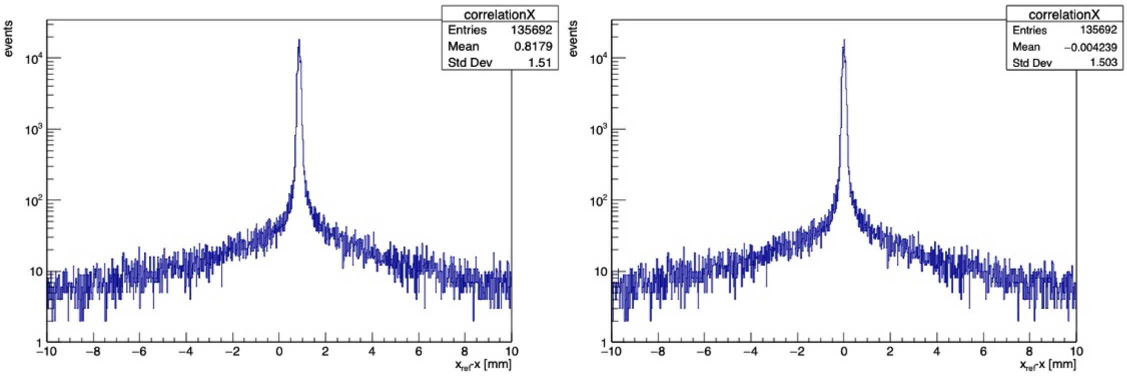

Figure 6.7: *Left: Example of correlation map before prealignment and alignment operations. Right: Example of correlation map after prealignment and alignment operations.*

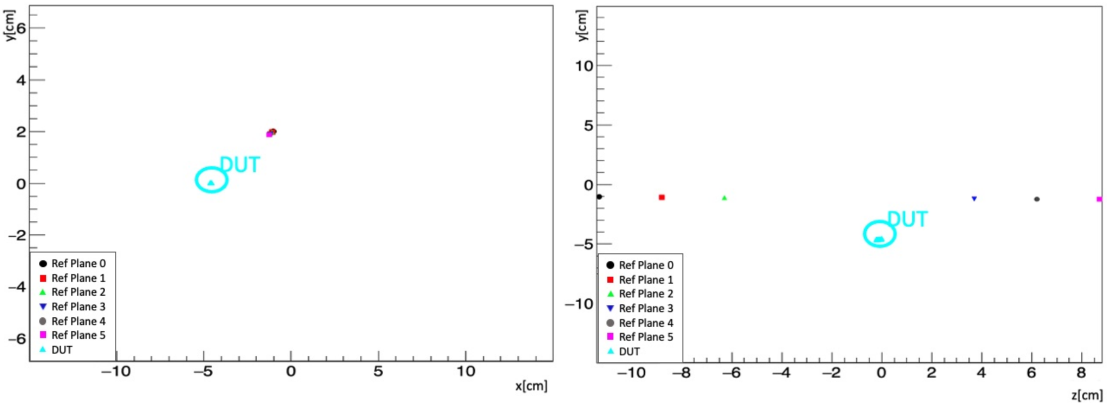

Figure 6.8: *Reference planes hits after the alignment operations.*

After the prealignment is performed, the AlignmentTrackChi2 module is used to perform the final alignment. The algorithm builds tracks that cross hits in the planes of the telescope, performs fit with straight tracks models and performs roto-translations to minimize the χ^2. These operations are repeated iteratively until the residuals are centred in 0. The root mean square of the residuals distributions correspond to the spatial resolution of each plane and should be close to pixel pitch/$\sqrt{12}$. Figure 6.7, shows an example of correlation distribution before and after the alignment operations. These alignment operations allow the roto-translation matrices for alignment to be obtained. These matrices are then applied to the hit coordinates (Figure 6.8) to obtain the data passed to the Pixel Chamber track reconstruction algorithm.

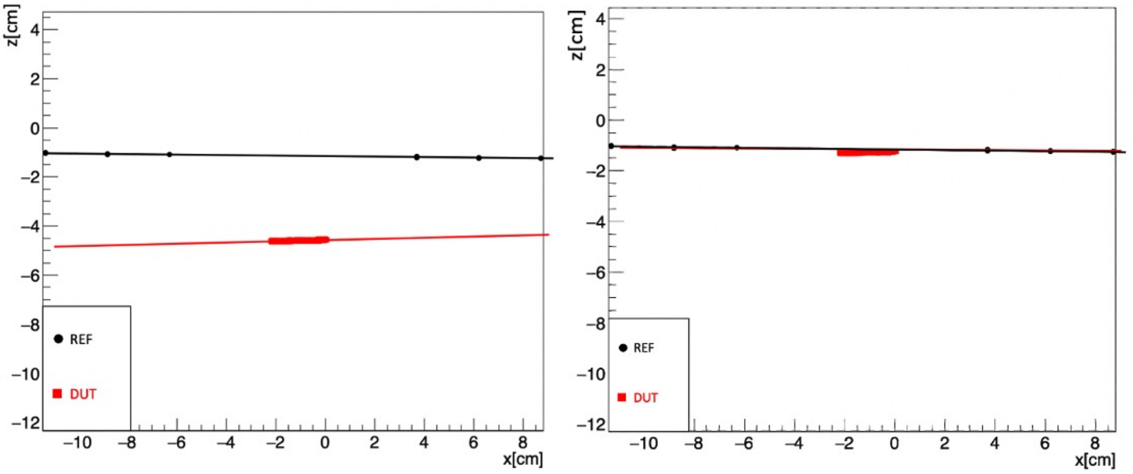

Figure 6.9: *Example of track reconstruction and fit in DUT and reference planes. Left: Before the alignment. Right: After the alignment*

6.2.2 Track reconstruction with Pixel Chamber algorithm

Track reconstruction and fit is performed as described in chapter 5, section 5.2 both in reference planes and in the DUT. 100% of tracks in DUT are well reconstructed ($\chi^2/\mathrm{ndf} < 2.5$) in the configuration containing C4 chip and in the configuration containing A1 chip. However in some events there are no hits in all the reference planes and not all tracks in reference planes are reconstructed (90% in A1 configuration and 92% in C4 configuration). The analysis and the considerations are the same for both configurations (A1 and C4).

An example of reconstruction and fit of the track produced in the DUT and reference planes is shown in Figure 6.9, left. The alignment has been performed for reference planes only and the parameters obtained from the fit have been used to determine the roto-translation matrix for the alignment of the DUT to the telescope planes.

From the track fit we obtain the direction cosines $\vec{r}$, $\vec{d}$ and a crossing point of the tracks crossing respectively reference planes and DUT. The rotation angle θ (equation 6.1) is determined as the arccosine of the scalar product of the two normalized direction cosines:

$$\theta = cos^{-1}(\vec{r}\cdot\vec{d}) \tag{6.1}$$

The angle between reference planes and DUT is 1.46 ± 0.7 degrees for A1 configuration and 2.5 ± 0.7 degrees for C4 configuration.

The translation parameters are obtained as the difference between the coordinates of two points crossed by the tracks (obtained by the fit) (equation 6.2):

$$(\Delta x, \Delta y, \Delta z) = (x_{0r}, y_{0r}, z_{0r}) - (x_{0d}, y_{0d}, z_{0d}) \tag{6.2}$$

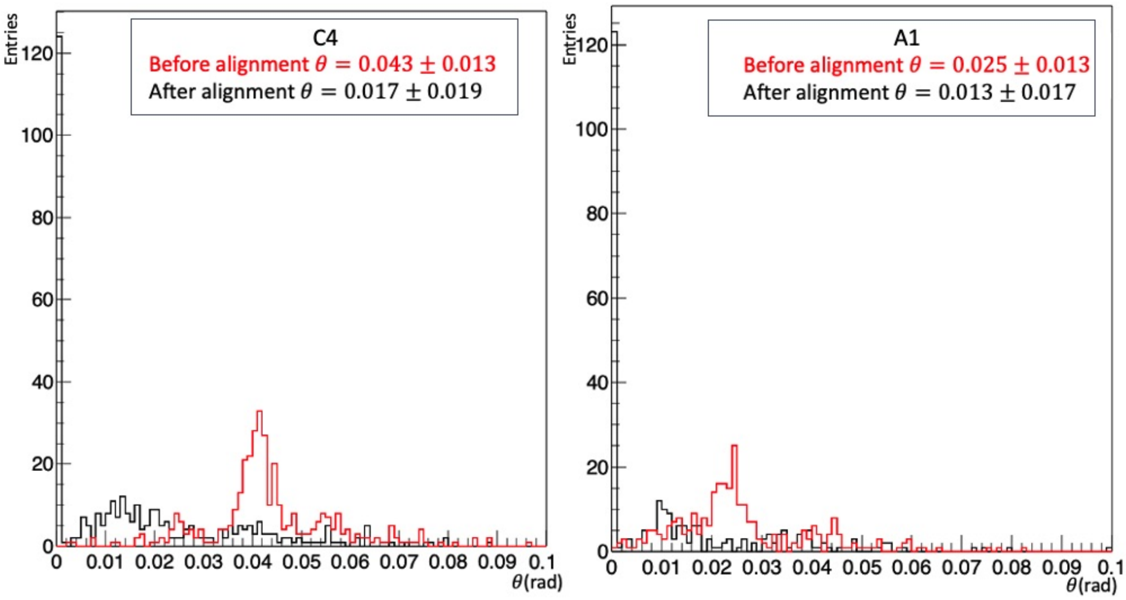

Figure 6.10: *Distributions of angles between tracks in reference planes and DUT. Left: C4 configuration, right: A1 configuration.*

An example of the result of the alignment of the DUT to the reference planes is shown in the Figure 6.9, right.

The distributions of the angles between the tracks reconstructed in the reference planes and in the DUT are shown in the Figure 6.10. Angular distributions obtained after alignment have a 0-compatible mean value in both configurations and a peak at 0 rad is present. The analysis therefore shows that it is possible to reconstruct the tracks with excellent precision with the Pixel Chamber algorithm and that it is possible to find an excellent correlation between the tracks in the reference planes and those in the DUT.

6.3 Planar ALPIDE sensor parallel to beam

I've participated in two test beams where the reconstruction of long tracks produced by high energy electrons and high energy hadrons was tested in a planar ALPIDE parallel to the beam. In this configuration a planar ALPIDE is placed so that the beam crosses its long side. An example is shown in the Figure 6.11 which shows the setup used at the SPS test beam schematized in Figure 6.12, right.

In both tests the setup was similar to the one described above: a telescope consisting of 2 arms containing 2 ALPIDE each with a planar chip in the center shown in Figure 6.12. The analysis of the data acquired during these two test beams focused on the DUT because the telescope was composed by 2 arms with 2

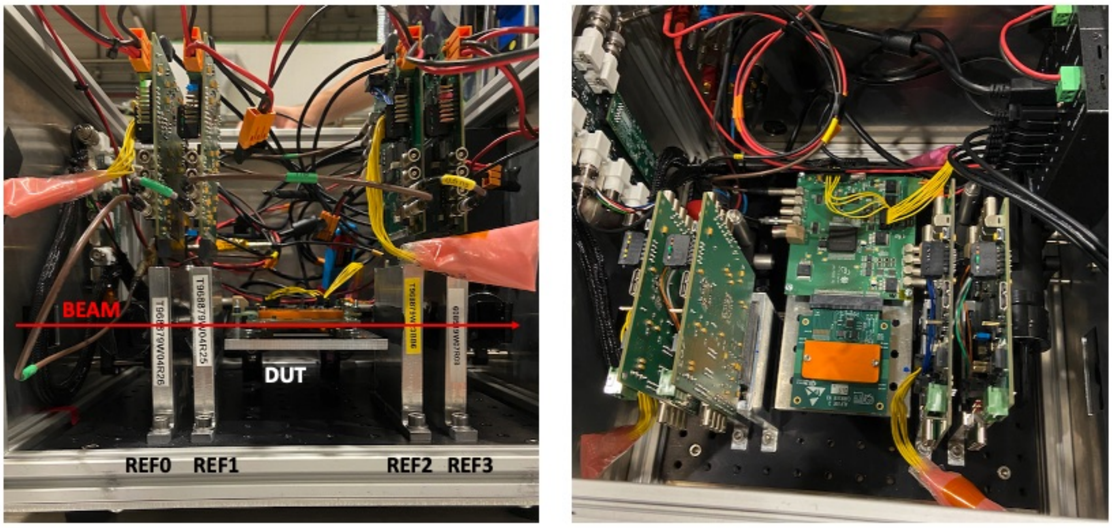

Figure 6.11: *The setup used during the SPS test beam. Left: Image from the side. Right: Image from the top.*

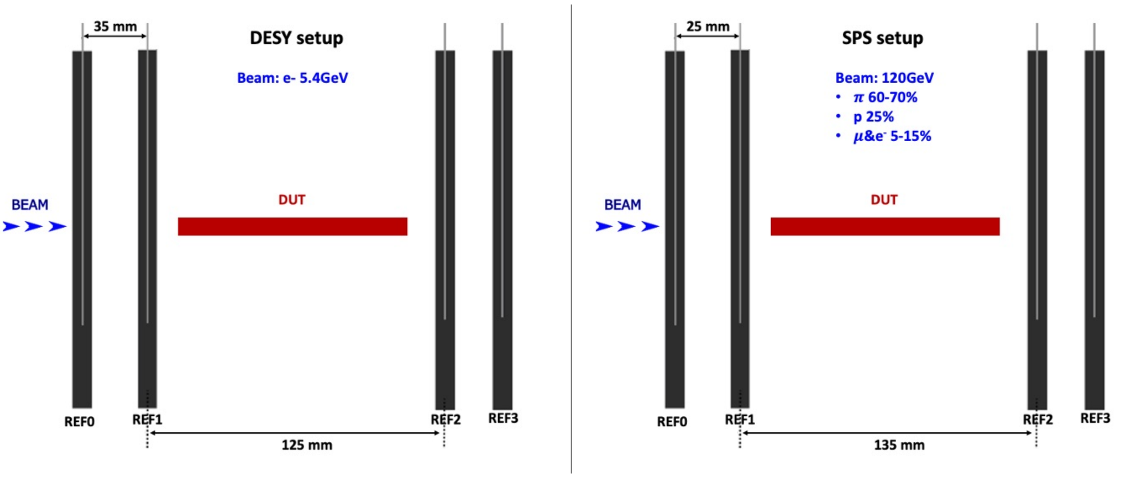

Figure 6.12: *Left: schematic description of the setup used during the April test beam at DESY. Right: schematic description of the setup used during the July test beam at SPS.*

reference planes each which does not allow an accurate track reconstruction.

For both test beams, the back bias voltage was set to -3V for both the telescope ALPIDE and DUTs and the threshold was set to 50 e^-.

With the DUT in this configuration, a long track in the ALPIDE is expected to be produced in events where the beam particle crosses the sensor. This track doesn't necessarily run through the entire chip. Since the thickness of the chip is

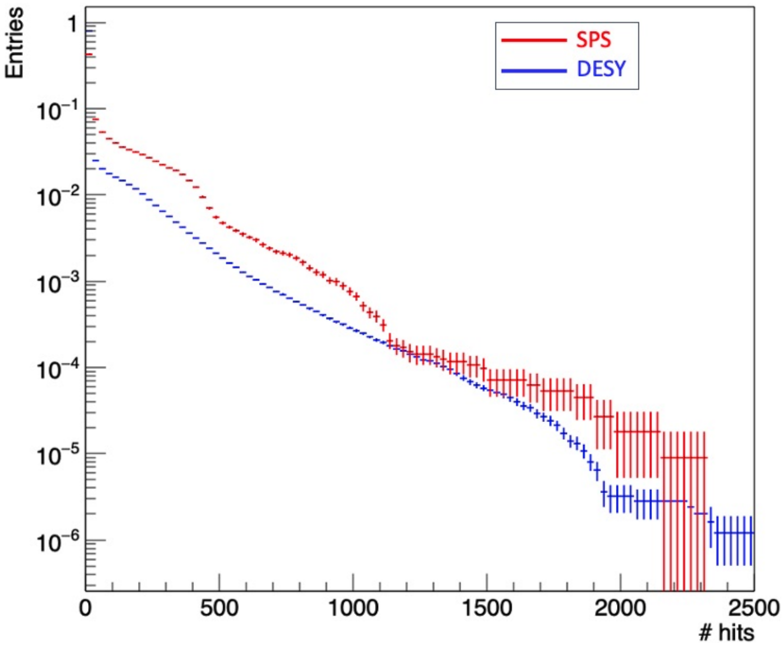

Figure 6.13: *Fraction of hits in the DUT for DESY test beam (blue) and SPS test beam (red).*

only 50 µm, a slight scattering can cause the particle to exit from the sensor plane. Another reason is that the particles momentum does not have a single component (along the axis of the beam) and a small inclination is enough for the particle to exit from the sensor before crossing it entirely.

In Figure 6.13 the distributions of the fractions of hits in the DUT for the test beam at DESY and at the SPS are shown. In some events there are no hits in the DUT because the beam particle has crossed the planes of the telescope but not the DUT (the beam is not perfectly collimated). In part of the events, hits are produced, but since the purpose of the following analysis is to test the possibility of observing long tracks in the DUT, the reconstruction of the tracks was performed only on events where the number of hits in the DUT is greater than 550, corresponding to $\sim 0.05\%$ of events at DESY, and $\sim 0.06\%$ of events at the SPS.

6.3.1 DESY test beam in April 2021

Tests have been performed with electron beams of 2.4 and 5.4 GeV. The two data sets have been merged in the following analysis. The track reconstruction is performed as described in section 5.2.

The energy loss for electrons at these energies occurs mainly by bremsstrahlung. For this reason it is expected that an electron, entering the sensor parallel to it, will mainly produce straight tracks along the entire path producing, at most, low-energy

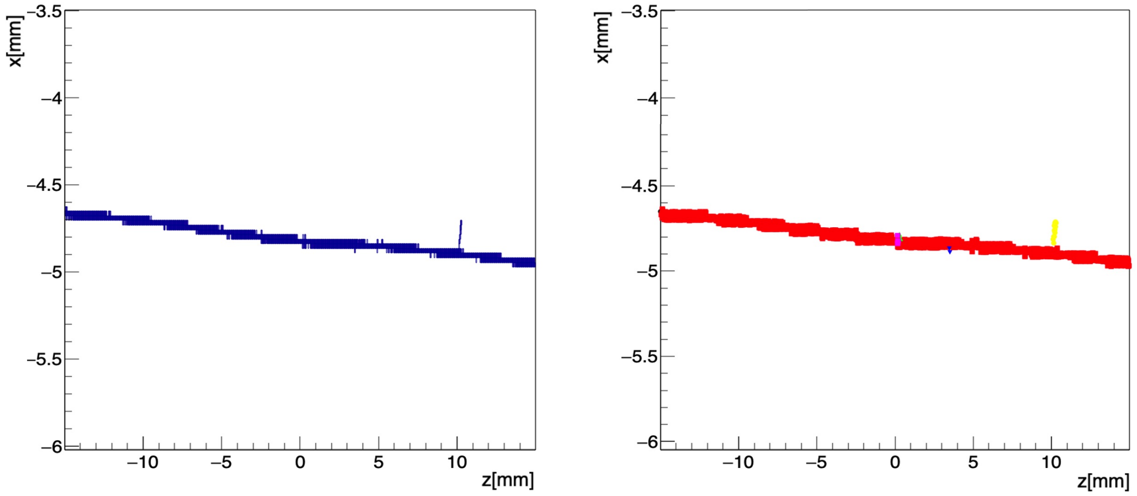

Figure 6.14: *Left: Hit map of an event in which an electron traverses the whole DUT. Right: Reconstruction of the track produced in the DUT.*

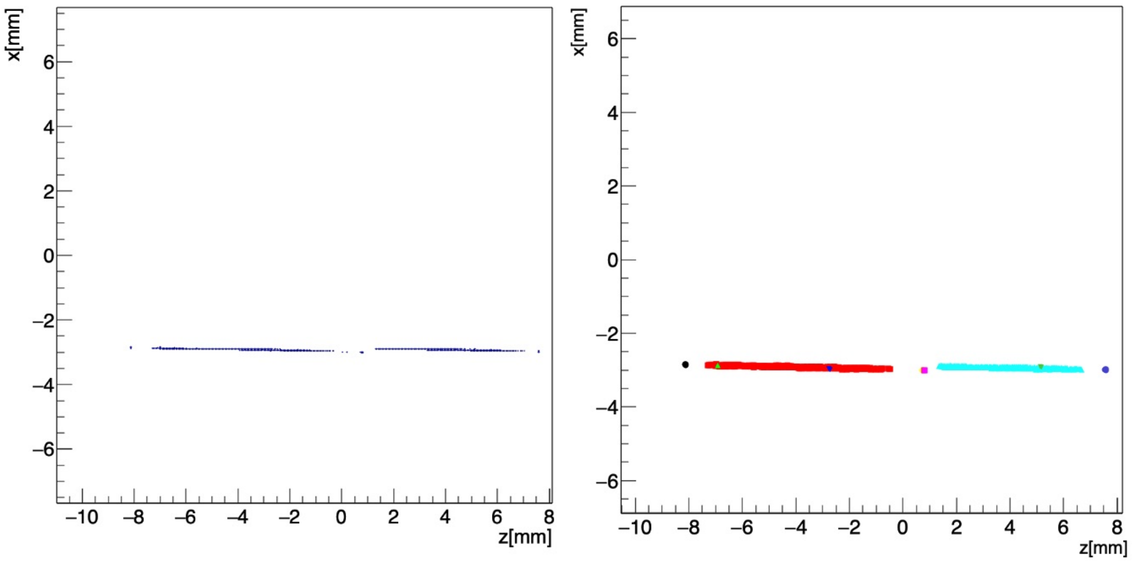

Figure 6.15: *Left: Hit map of an event in which two electrons traverse the planes of the telescope and the DUT. Right: Reconstruction of the tracks produced in the DUT.*

δ electrons that for the most part produce few hits before exiting the sensor. An example of a track produced by an electron passing through the ALPIDE for almost its entire length is shown in Figure 6.14, left. The reconstructed track is shown in Figure 6.14, right. Also a δ ray is visible and reconstructed.

However, there are events, as in Figure 6.15 in which there are more tracks. These

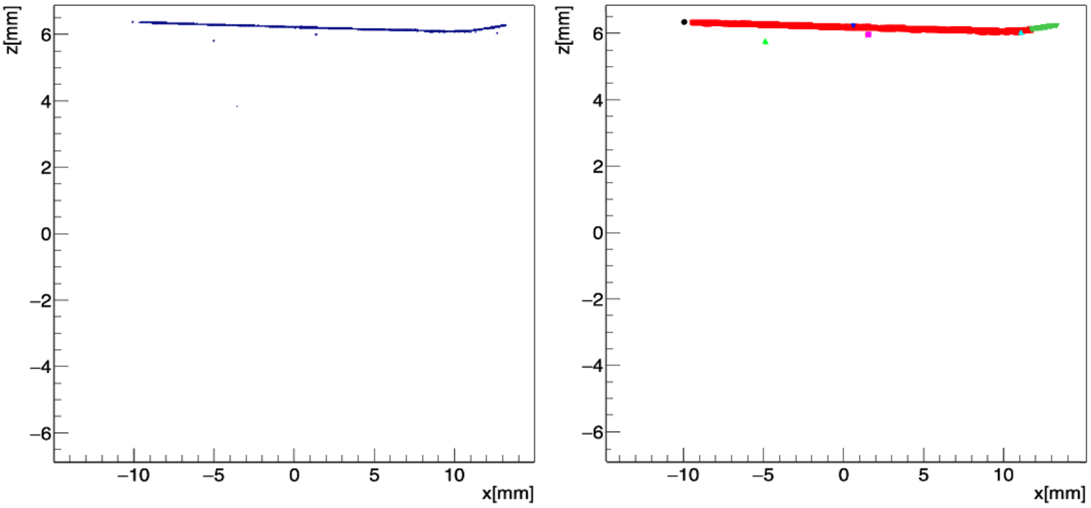

Figure 6.16: *Left: Hit map of an event in which an electron traverses the DUT and is scattered. Right: Reconstruction of the tracks produced in the DUT.*

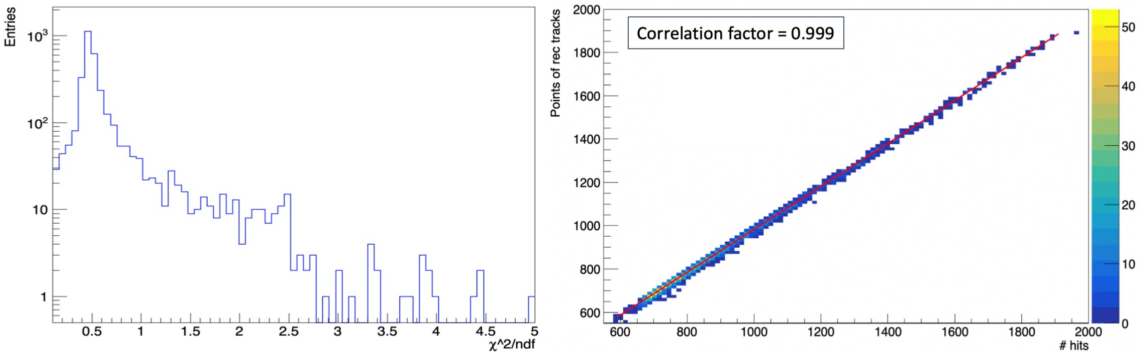

Figure 6.17: *Left:* χ^2/ndf *distribution for reconstructed tracks reconstructed. Right: correlation plot between event hit number and hits associated to recnstructed tracks.*

tracks could be due to more than one electron crossing the sensor and recorded as a single event. It could also occur that an electron scatters off a silicon nucleus as seen in Figure 6.16. In all cases the reconstruction is satisfactory.

In Figure 6.17 left, the distribution of the χ^2/ndf for reconstructed tracks with more than ten hits is shown. Also from that distribution, tracks seems to be reconstructed satisfactorily.

The correlation of the event hit number versus the number of points associated to the reconstructed tracks for the event is shown in the Figure6.17, right. Essentially all hits are associated to tracks by the reconstruction algorithm.

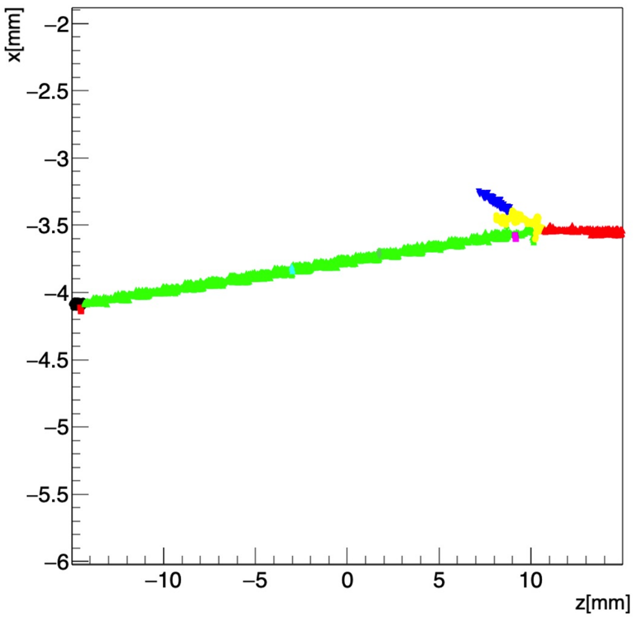

Figure 6.18: *Reconstruction of the tracks produced in the DUT in a proton-silicon interaction.*

6.3.2 SPS test beam in July 2021

During the test beam at SPS the setup shown in Figure 6.11 was used. The beam was composed of pions ($60 - 70\%$), protons (25%), muons and electrons ($5 - 15\%$) with an energy of 120 GeV.

The main purpose of this test was once again to test the possibility of reconstructing long tracks in a single ALPIDE produced, this time, mainly from hadrons for which inelastic nuclear interactions with silicon can be observed. In this case there will be tracks that originate from the interaction vertex, as shown in the Figure 6.18. In that event, a hadron crosses almost the entire sensor and finally interacts with the silicon giving rise to a primary vertex. Unfortunately, using only one ALPIDE sensor, it is not possible to obtain enough hits from the tracks produced in the vertices to obtain a complete reconstruction of the tracks from the primary vertex. However, it is interesting to note that even with a single ALPIDE it is possible to observe primary vertices.

Summary and outlook

In this thesis, Pixel Chamber, a three dimensional active target pixel matrix providing a continuous tracking for high precision track and vertex reconstruction, has been studied and demonstrated. We explored the possibility to use the high performance ALPIDE MAPS, recently developed and installed for the Inner Tracking System (ITS2) of the ALICE experiment at CERN.

The idea is to stack a few hundreds of ALPIDE sensors on top of each other to provide a continuous three dimensional tracking. Sensors are arranged in a staggered fashion with an offset of 150 μm to provide space for wire bonding of the sensor pads. Between two sensors there will be a layer of non-conductive glue with a thickness of 10 μm. The basic unit of Pixel Chamber is a stack of nine ALPIDE sensors called A9 stack. Control signals, clock and data lines will be interfaced on a carrier board which has been developed already. The ALICE data acquisition chain developed for the Run 3 of the LHC will be used. The A9 total thickness is 540 μm and Pixel Chamber is the assembly of twenty-four A9 stacks. The total active volume of Pixel Chamber is therefore $\sim$ 30x13x10 mm^3 and contains $\sim 10^8$ pixels.

Detailed cooling studies have been carried out. COMSOL Multiphysics simulations have been developed and show that without any cooling, the entire stack temperature would reach a temperature of about 570°C. Different solutions have been studied to cool down the full Pixel Chamber stack below 40°C. The best solution is to use two copper heat sinks (40 mm thickness), one on the top and one at the bottom of the sensor, and to apply an air flow at 2 m/s (at room temperature) along the long direction of the detector. Using air flow and copper sinks, the stabilized temperature is $\sim$36.7°C.

COMSOL Multiphysics has been also used to simulate an experimental setup to be used for laboratory tests. Simulations show that it is possible to reproduce the Pixel Chamber heat conditions with an aluminium block with the Pixel Chamber volume dimensions connected to two resistors at 25 W. At the moment the installation of the setup is under development and the studies on cooling in the laboratory will be carried out in the near future.

There is an ongoing R&D on the gluing of the ALPIDE sensors on top of each other using a flip-chip bonding machine in collaboration with the University of Geneva and CERN. There are a few options for gluing which are being studied. This will be followed by wire bonding studies before constructing the first A9 stack prototype. Subsequently the A9 stack will be characterized in test beams and the assembly of several A9 stacks will be performed to construct the Pixel Chamber.

Tracking and vertexing algorithms have been developed and simulations studies of proton-silicon interaction at 400 GeV performed with Geant4 have been used to study performances of those algorithms. Charm particle decays have been overlayed to p-Si interaction vertices.

The tracking algorithm is based on hit density and shows that it possible to obtain a track reconstruction efficiency of $\sim$ 90% for the reconstruction of hadronic tracks produced in proton-silicon vertices.

For the primary vertex reconstruction several options have been considered. The best one is a weighted least square fit procedure that leads to excellent results. Resolutions improve significantly with increasing multiplicity reaching the value of $\sim$5 µm along the beam axis and $\sim$0.5 µm along the transverse axes for a track multiplicity of 15. With Pixel Chamber it is possible to obtain primary vertex resolutions that are about one order of magnitude better than those obtained by the vertex detectors at LHC experiments.

For the secondary vertex reconstruction, the $D^0 \to K\pi$ decay has been considered. The vertexing algorithm is the same used for the primary vertex reconstruction with some difference to take in account the vertex multiplicity. The D^0 secondary vertices inside Pixel Chamber can be reconstructed with very good resolutions that reach $\sim$25 µm along the beam axis, $\sim$5 µm and $\sim$4 µm along the transverse axes.

As a prototype of the A9 stack is not yet available at the moment, the track reconstruction algorithm performances have been tested on a single ALPIDE sensor using data acquired in three test beams. The chip has been exposed to particle beams parallel to its surface producing long and continuous tracks.

Two test beams have been carried out at DESY with electrons. The third one has been carried out at SPS with a beam composed by hadrons (protons and pions) and leptons (muons and electrons).

During the first test beam at DESY bent ALPIDE sensors have been used. The data analysis has been performed considering long tracks produced when electrons cross the chip surface which is roughly flat. During the other two test beams a planar ALPIDE has been used. The data analysis show that the tracking algorithm is very efficient for the reconstruction of long, continuous tracks produced in a single ALPIDE sensor. essentially all long tracks are reconstructed with very good precision.

Track reconstruction could be further improved taking into account multiple scattering. This will be done adding a Kalman filter fit to the algorithm. In addition, machine learning and neural networks might also be used to improve track and vertex reconstructions and their use is being considered as a further step.

Among different possible applications of Pixel Chamber, its coupling to a silicon telescope has the potential to allow a measurement of the charm cross-section in proton-silicon interactions at CERN SPS energies. This is a fundamental measurement since the theory of strong interactions has still large uncertainties, and even for searches of new particles beyond the Standard Model. The total charm cross section would be measured as:

$$\sigma_{TOT}(c\bar{c}) = \frac{1}{2}(\sigma(D^+) + \sigma(D^-) + \sigma(D^0) + \sigma(\bar{D}^0) + \sigma(\Lambda_c^+) + \sigma(D_s) + \sigma(\bar{D}_s)) \quad \text{(C.3)}$$

with all the states contributing to it very precisely measured.

Even more interesting are possible medical applications.

The ALPIDE sensors have been also proposed for medical imaging applications like Proton Computed Tomography, that allows to reduce the uncertainty of the range in particle therapy. An example is the work done at the University of Bergen [56].

Small area monolithic pixel detector stacks have recently been proposed for applications in the medical field for the realization of small Positron Emission Tomography (PET) devices. An example is the TT-PET project at the University of Geneva [57].

The technology has reached a maturity such as to allow the creation of sensors with a very large area, substantially limited only by the size of the silicon wafer. This is possible through a technological process known as stitching which allows replicating different parts of a circuit in the wafer, overcoming the limitation imposed by the grating used for photolithography masks. This technology is already used in the industry, for example, for sensors used in dental radiography.

At present an R&D to produce large area stitched sensors is under way for the construction of a new tracking systems ITS3 for the ALICE experiment at CERN. The proposal is to produced monolithic sensors of area ∼1.5x25 cm^2.

A pioneering development would be the first three-dimensional stack with large area monolithic pixel sensors ever built. In this way we would overcome the current limitations related to the small size of the sensors by creating ground-breaking imaging devices not only for particle physics using the device as an active-target but also in the medical field as large PET devices.

Acknowledgments

First of all I want to thank my supervisor, Professor Gianluca Usai, for guiding me during these years and for showing me how to improve starting from mistakes. I also thank my co-supervisor, Dr. Sabyasachi Siddhanta for his ongoing support and for his commitment to achieving a first stack of ALPIDE before the end of my PhD.

A big thank you to Mauro Arba and Marcellino Tuveri for the technical design of Pixel Chamber and for the help in the development of the setup for the validation of cooling simulations in record time.

I also owe a big thank you to Davide Marras who helped me in the early stages of the development of the track reconstruction code and who always found the time to help me clarify many doubts.

Many thanks to Daniele Mura and Carlo Puggioni for their constant availability and technical support.

I also thank the entire ITS3 team for bringing me for the first time to a test beam, for the support and for the teachings.

A special mention goes to Purba Bhattacharya for the simulations on cooling and for the constant availability to help me, even from afar.

I also owe a special thanks to Professor Corrado Cicalò for proposing me to join the Pixel Chamber project.

I would like to thank the whole of Group 3 of the INFN in Cagliari. Prof. Alessandro De Falco, Director Alberto Masoni, Ester, Biswarup, Mauro and Stefano. Last but not least Giacomo and Valerio for their mutual support.

A great thanks to all my fellow PhD students and interns with whom I shared many breaks, in particular a big thank you to Andrea for the roasted chickens and especially to Michela for the therapeutic "banana breaks".

I thank all my friends, especially Roberto and Marianna and those of the "Friday dinners", in particular Luca and Valerio who had to suffer my outbursts in the department and outside. A special thanks to Silvia, sister not of blood, who has always listened to me, supported and advised, from the first year of university.

Finally I thank all my family. My parents who have never stopped believing in me and have always supported me. My brother, distant but always present. My husband Matteo who has always encouraged me and who, more than all, has suffered my anxieties and with his constant calm has reassured me. He deserves special mention for listening to all of my lectures and talks.

Sincere thanks to Prof. G. Iacobucci and Dr. M. Vicente of Particle Physics Department (DPNC), University of Geneva for their support and the opportunity to use the flip-chip bonding machine which is installed in their department.

This thesis work was supported by the project funded by Regione Autonoma della Sardegna, Fondo di Sviluppo e Coesione 2014 - 2020 - Interventi di sostegno alla ricerca: *Pixel Chamber: a universal silicon heavy-flavour imager with monolithic active pixel sensors for measurements of charm and beauty with unprecedented precision.*

Bibliography

[1] ALICE Collaboration. Technical Design Report for the Upgrade of the ALICE Inner Tracking System. Technical report, CERN Document Server, 11 2013. URL `https://cds.cern.ch/record/1625842`.

[2] G. Rinella Aglieri *et al.* The ALPIDE pixel sensor chip for the upgrade of the ALICE Inner Tracking System. *Nuclear Instruments and Methods in Physics Research, Section A: Accelerators, Spectrometers, Detectors and Associated Equipment*, 845:583–587, 2 2017. ISSN 01689002. doi: 10.1016/j.nima.2016.05.016.

[3] ALICE ITS ALPIDE development team. ALPIDE Operations Manual, 2016.

[4] Tower Semiconductor. URL `https://towersemi.com/`.

[5] S. Siddhanta *et al.* The upgrade of the Inner Tracking System of ALICE. *Nuclear Physics A*, 931:1147–1151, 11 2014. ISSN 03759474. doi: 10.1016/j.nuclphysa.2014.09.041.

[6] D. Colella *et al.* PoS(VERTEX2015) ALICE ITS: the Run 1 to Run 2 transition and recent operational experience, 2015. URL `https://pos.sissa.it/254/003`.

[7] F. J. Hasert *et al.* Observation of neutrino-like interactions without muon or electron in the gargamelle neutrino experiment. *Physics Letters B*, 46:138–140, 9 1973. ISSN 0370-2693. doi: 10.1016/0370-2693(73)90499-1.

[8] V. E. Barnes*et al.* Observation of a Hyperon with Strangeness Minus Three. *Physical Review Letters*, 12:204, 2 1964. ISSN 00319007. doi: 10.1103/PhysRevLett.12.204. URL `https://journals.aps.org/prl/abstract/10.1103/PhysRevLett.12.204`.

[9] G. Bellini *et al.* Live Targets as a Tool to Study Short Range Phenomena in Elementary Particle Physics. *Miniaturization of High-Energy Physics Detectors*, pages 41–55, 1983. doi: 10.1007/978-1-4684-8887-6_4. URL `https://link.springer.com/chapter/10.1007/978-1-4684-8887-6_4`.

[10] A. Mulliri *et al.* Pixel Chamber: A solid-state bubble chamber for imaging of charm and beauty. *Nuovo Cimento della Societa Italiana di Fisica C*, 44, 1 2021. ISSN 18269885. doi: 10.1393/ncc/i2021-21006-9.

[11] A. Mulliri *et al.* Pixel chamber: a solid-state active-target for 3D imaging of charm and beauty. *Journal of Instrumentation*, 16:C12029, 12 2021. ISSN 1748-0221. doi: 10.1088/1748-0221/16/12/C12029. URL `https://iopscience.iop.org/article/10.1088/1748-0221/16/12/C12029`.

[12] G. Usai *et al.* Pixel chamber: a universal silicon heavy-flavour imager with monolithic active pixel sensors for measurements of charm and beauty with unprecedented precision. Project supported by Regione Autonoma della Sardegna Fondo di Sviluppo e Coesione 2014 - 2020 - Interventi di sostegno alla ricerca, .

[13] G. Rinella Aglieri *et al.* The NA62 GigaTracKer: a low mass high intensity beam 4D tracker with 65 ps time resolution on tracks. *Journal of Instrumentation*, 14(07):P07010–P07010, jul 2019. doi: 10.1088/1748-0221/14/07/p07010. URL `https://doi.org/10.1088/1748-0221/14/07/p07010`.

[14] G. Apollinari *et al.* High-luminosity large hadron collider (HL-LHC) : technical design report V.O.1. Technical report, 2017.

[15] P. Riedler. Upgrade of the ALICE Inner Tracking System (ITS). Quark Matter conference. 2015.

[16] M. Mager *et al.* ALPIDE, the Monolithic Active Pixel Sensor for the ALICE ITS upgrade. *Nuclear Instruments and Methods in Physics Research Section A: Accelerators, Spectrometers, Detectors and Associated Equipment*, 824:434–438, 7 2016. ISSN 0168-9002. doi: 10.1016/J.NIMA.2015.09.057. URL `https://doi.org/10.1016/j.nima.2015.09.057`.

[17] C. Yang *et al.* A Prototype Readout System for the ALPIDE Pixel Sensor. *IEEE Transactions on Nuclear Science*, 66:1088–1094, 7 2019. ISSN 15581578. doi: 10.1109/TNS.2019.2913335.

[18] J. Schambach *et al.* A Radiation-Tolerant Readout System for the ALICE Inner Tracking System Upgrade. *2018 IEEE Nuclear Science Symposium and Medical Imaging Conference, NSS/MIC 2018 - Proceedings*, 11 2018. doi: 10.1109/NSSMIC.2018.8824419.

[19] Ultra-thin PET-based 5μm Double Sided Tape No.5600. URL `https://www.nitto.com/eu/it/products/double/053/`.

[20] ACCuRA100 semi-automatic flip-chip bonder. URL `https://set-sas.fr/catalog/acc%C2%B5ra100/`.

[21] G. Iacobucci *et. al.* M. Vicente. Particle Physics Department (DPNC), University of Geneva.

[22] G. De Robertis *et al.* A modular system for acquisition, interface and control (MOSAIC) of detectors and their related electronics for high energy physics experiment. *EPJ Web of Conferences*, 174, 2 2018. ISSN 2100014X. doi: 10.1051/EPJCONF/201817407002.

[23] 6-Axis NanoMax™ NanoPositioning Flexure Stages. URL `https://www.thorlabs.com/newgrouppage9.cfm?objectgroup_id=1100`.

[24] Travel Translation Stages, Crossed-Roller Bearings. URL `https://www.thorlabs.com/newgrouppage9.cfm?objectgroup_id=10211&pn=XR25C#10212`.

[25] Polarization Camera with 5.0 MP Monochrome CMOS Sensor. URL `https://www.thorlabs.com/newgrouppage9.cfm?objectgroup_id=13033`.

[26] Broadband Halogen Fiber Optic Illuminators. URL `https://www.thorlabs.com/newgrouppage9.cfm?objectgroup_id=884&pn=OSL2#5634`.

[27] A. Mulliri. Pixel chamber: a solid-state active target for 3D imaging of charm and beauty. IEEE Nuclear Science Symposium. 2021.

[28] Software di Simulazione COMSOL Multiphysics®. URL `https://www.comsol.it/`.

[29] COMSOL Multiphysics. Introduction to comsol multiphysics®. *COMSOL Multiphysics, Burlington, MA, accessed Feb*, 9:2018, 1998.

[30] K. J. Bathe. Finite Element Method. *Wiley Encyclopedia of Computer Science and Engineering*, pages 1–12, 6 2008. doi: 10.1002/9780470050118.ECSE159. URL `https://onlinelibrary.wiley.com/doi/full/10.1002/9780470050118.ecse159https://onlinelibrary.wiley.com/doi/abs/10.1002/9780470050118.ecse159https://onlinelibrary.wiley.com/doi/10.1002/9780470050118.ecse159`.

[31] Expression of Interest for an ALICE ITS Upgrade in LS3, 10 2018. URL `https://cds.cern.ch/record/2644611`.

[32] Caddock 25 ohm Power Film Resistor — RS Components. URL `https://my.rs-online.com/web/p/through-hole-resistors/3205006`.

[33] DS18B20+ Distributore elettronico — Maxim Integrated — Ariat-Tech.com. URL `https://www.ariat-tech.it/parts/maxim-integrated/DS18B20`.

[34] Raspberry Pi. URL `https://www.raspberrypi.com/`.

[35] 9WP0812H401 Splash Proof Fan-San Ace-SANYO DENKI. URL `https://products.sanyodenki.com/en/sanace/dc/splash-proof-fan/9WP0812H401/`.

[36] RS PRO DT-3893 Vane 30m/s Max Air Velocity Air Flow, Air Velocity, Temperature Anemometer. URL `https://my.rs-online.com/web/p/anemometers/1938696`.

[37] S. Agostinelli *et al.* Geant4-a simulation toolkit. *Nuclear Instruments and Methods in Physics Research Section A: Accelerators, Spectrometers, Detectors and Associated Equipment*, 506:250–303, 7 2003. ISSN 0168-9002. doi: 10.1016/S0168-9002(03)01368-8.

[38] J. Allison *et al.* Geant4 Developments and Applications. *IEEE Transactions on Nuclear Science*, 2006. doi: 10.1109/TNS.2006.869826.

[39] S. Alioli *et al.* A general framework for implementing NLO calculations in shower Monte Carlo programs: the POWHEG BOX. *Journal of Instrumentation*, 2 2010. doi: 10.1007/JHEP06(2010)043. URL `http://dx.doi.org/10.1007/JHEP06(2010)043`.

[40] Torbjörn Sjöstrand, Stephen Mrenna, and Peter Skands. Pythia 6.4 physics and manual. *Journal of High Energy Physics*, 2006(05):026–026, May 2006. ISSN 1029-8479. doi: 10.1088/1126-6708/2006/05/026. URL `http://dx.doi.org/10.1088/1126-6708/2006/05/026`.

[41] M. Ester *et al.* A Density-Based Algorithm for Discovering Clusters in Large Spatial Databases with Noise. 1996. URL `www.aaai.org`.

[42] J. Joseph. A Perspective on Quicksort. *Computing in Science and Engineering*, 2, 1 2000. doi: 10.1109/5992.814657. URL `https://dl.acm.org/doi/abs/10.1109/5992.814657`.

[43] F. James *et al.* CERN Program Library Long Writeup D506 Function Minimization and Error Analysis Reference Manual Version 94.1. Technical report, CERN Document Server, .

[44] M. Kucharczyk *et al.* Primary Vertex Reconstruction at LHCb, 2014.

[45] G. Agakichiev *et al.* A new robust fitting algorithm for vertex reconstruction in the CERES experiment. *Nuclear Instruments and Methods in Physics Research Section A: Accelerators, Spectrometers, Detectors and Associated Equipment*, 394:225–231, 7 1997. ISSN 0168-9002. doi: 10.1016/S0168-9002(97)00658-X.

[46] B. A. Rojas *et al.* On Tukey's test of additivity, . URL `https://conservancy.umn.edu/handle/11299/199160`.

[47] Particle Data Group. URL `http://pdg.lbl.gov/order.http://pdg.lbl.gov/`.

[48] ALICE Collaboration. Letter of Intent for an ALICE ITS Upgrade in LS3, LHCC-2019-018, 2019.

[49] S. Siddhanta *et al.* A Readout System for single ALPIDE sensors of the ALICE Inner Tracking System Upgrade. pages 1–3, 8 2021. doi: 10.1109/NSS/MIC42677.2020.9508095.

[50] Volume 1 Cyclone IV Device Handbook, 2016. URL `www.altera.com`.

[51] EZ-USB ® FX3: SuperSpeed USB Controller, 2018. URL `www.cypress.com`.

[52] ALICE ITS collaboration. First demonstration of in-beam performance of bent Monolithic Active Pixel Sensors. *Arxiv*, 5 2021. URL `http://arxiv.org/abs/2105.13000`.

[53] Y. Liu *et al.* EUDAQ2 – A Flexible Data Acquisition Software Framework for Common Test Beams. *Journal of Instrumentation*, 14, 7 2019. doi: 10.1088/1748-0221/14/10/p10033. URL `https://arxiv.org/abs/1907.10600v3`.

[54] D. Dannheim *et al.* Corryvreckan: A Modular 4D Track Reconstruction and Analysis Software for Test Beam Data. *Journal of Instrumentation*, 16, 11 2020. doi: 10.1088/1748-0221/16/03/p03008. URL `https://arxiv.org/abs/2011.12730v2`.

[55] M. Williams *et al.* Corryvreckan User Manual. Technical report, 2021.

[56] G. Tambave *et al.* Characterization of monolithic CMOS pixel sensor chip with ion beams for application in particle computed tomography. *Nuclear Instruments and Methods in Physics Research, Section A: Accelerators, Spectrometers, Detectors and Associated Equipment*, 958, 4 2020. ISSN 01689002. doi: 10.1016/J.NIMA.2019.162626.

[57] D. Ferrere *et al.* Module concept and thermo-mechanical studies of the silicon-based TT-PET small-animal scanner. *Arxiv*, 11 2018. URL `http://arxiv.org/abs/1812.00788`.